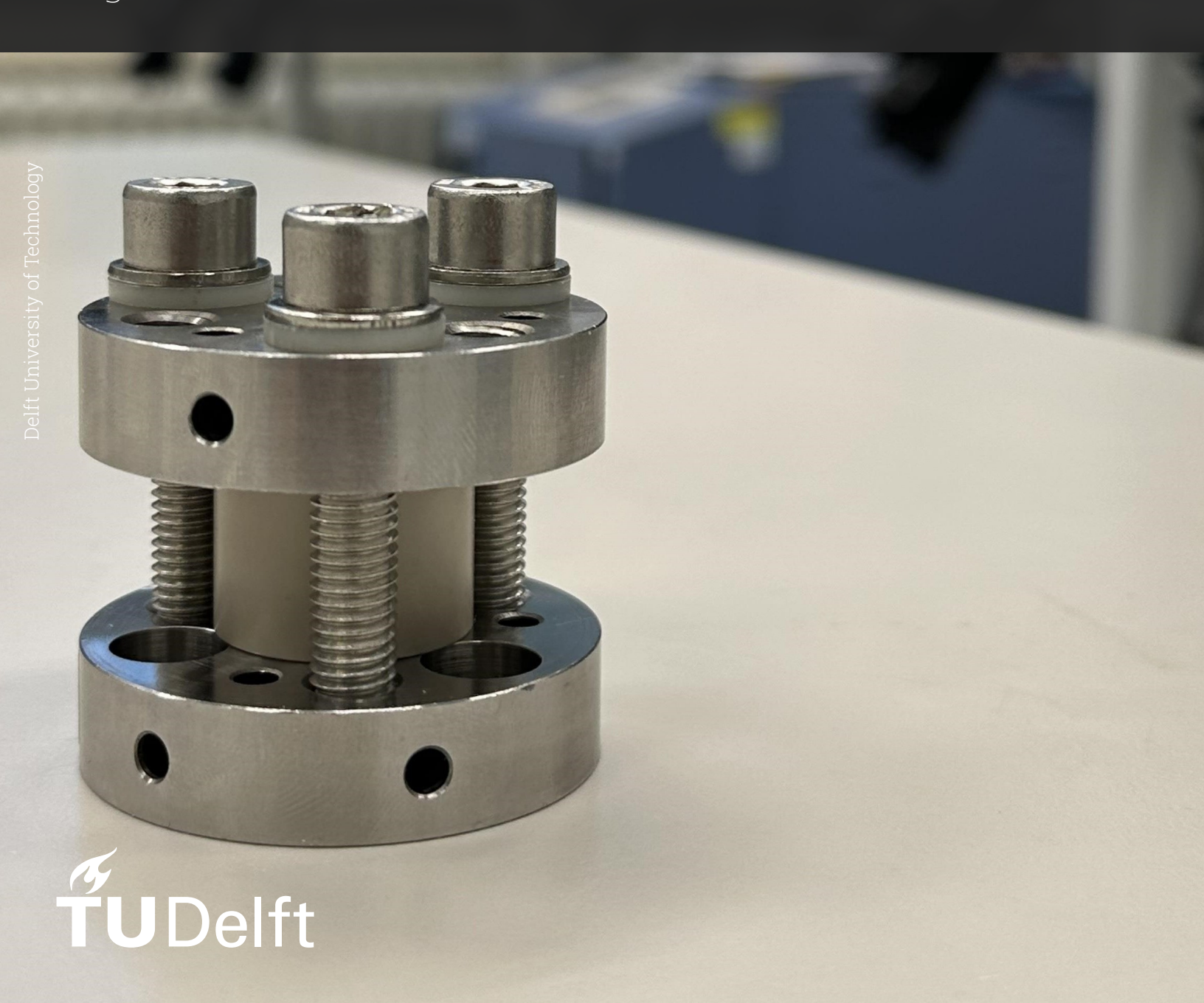
# Investigation of lithium argyrodite solid electrolyte with enriched halide substitution in the solid-state batteries

A Next Generation Battery Technology

Vignesh Kannan



## Investigation of lithium argyrodite solid electrolyte with enriched halide substitution in the solid-state batteries

A Next Generation Battery Technology

by

#### Vignesh Kannan

to obtain the degree of Master of Science in Sustainable Energy Technology at the Delft University of Technology, to be defended publicly on Monday August 26, 2024.

Student number: 5733685

Project duration: November 2023 - August 2024

Thesis committee: Prof. dr. ir. Marnix Wagemaker, TU Delft, SEE, Supervisor

Dr. Swapna Ganapathy, TU Delft, SEE, Supervisor

Dr. S.W.H. Eijt, TU Delft, FAME

Dr. Ajay Gautam, TU Delft, SEE, Daily Supervisor

Cover Photo: & Solid-State Cell image by author An electronic version of this thesis is available at https://repository.tudelft.nl/



#### Acknowledgements

This Master thesis is the result of an exciting and two-year journey in my life at TU Delft, packed with challenges and achievements that greatly influenced my academic career. I have learned a lot of things which helped me to gain knowledge and develop my skills. Firstly, I would like to show my gratitude to god, the almighty for being with me during my hard times and showered with blessing. I would like to express my deepest gratitude for my family for being my side in all my struggles & happiness and for showing unconditional support to me.

Professor dr. ir. Marnix Wagemaker, I would like to thank you for being my thesis supervisor and you are a true inspiration and your dedication towards the development of battery technology is remarkably astonishing. The interest for me to do thesis in batteries were sparked from your lectures in Energy Storage in Batteries course. I would like to thank Dr. Swapna for giving me the thesis topic and introducing Ajay as my daily supervisor and I would like to thank Dr. S.W.H. Eijt for examining the thesis and being a part of my thesis committee.

Dr. Ajay Gautam, I am truly amazed with your insights in this thesis. Your guidance and input were crucial to making this possible. I am thankful to have had you as my daily supervisor, for your encouragement, and for pushing me to learn additional knowledge that I will always remember. Your practical insights into the experiments have been a significant blessing. I really appreciate your efforts and time that you have invested in this thesis.

My sincere gratitude for Frans, Nirmal, Katarina, and Robert for helping me during the experiments and calmly explaining me about the equipments.

Finally, I would like to thank Raghav, Shriram and Kartik for being my side and helping me during my tough times and my gratitude for your invaluable support and once again, I would like to shown my deepest gratitude to my Appa, Amma and Lakshika for showing an unconditional love and support to me.

Vignesh Kannan Delft, The Netherlands August 2024

#### **Abstract**

The excessive use of the fossil fuel has attributed to the emission of carbon dioxide causing rising temperature. To counter act over this, the renewable based energy transition and lithium-ion batteries as storage facility in changing the landscape. However, these lithium-ion batteries prone to thermal runaway, lower operating conditions, dendrite formation making them vulnerable to the transition. All solid-state batteries are the next generation batteries making an revolution in the battery technology by replacing the highly volatile liquid electrolyte to the solid electrolyte for improved safety, high energy density (Li/Si possible to use the anode material), and longer cycle life

In this thesis, the halide incorporation in lithium argyrodite  $Li_{6-x}PS_{5-x}X_{1+x}$  (X= Cl, Br, I) solid electrolyte was synthesized and further characterized to understand the synthesis conditions and structural-ionic transport correlation of solid electrolyte. The halide enriched lithium argyrodite was synthesized using mechano-chemical synthesis by high energy ball milling and followed by heat treatment. All samples were investigated using following characteristics tools such as X-Ray diffraction, scanning electron microscopy, Raman spectroscopy, and Electrochemical impedance spectroscopy, to understand the structural information, morphology and the ionic conductivity of the composition. In results, the chloride/Bromide enriched in lithium argyrodite shows a higher ionic conductivity of around 14.77 mS  $cm^{-1}$  for  $Li_{5.5}PS_{4.5}Cl_{1.5}$  and 6.39 mS  $cm^{-1}$  for  $Li_{5.5}PS_{4.5}Br_{1.5}$ , and various annealing temperatures could improve the crystallinity of composition which also influences the higher ionic conductivity.

As we know from the literature, the lithium argyrodite based solid electrolyte has a narrow electrochemical stability window. It is interesting to note that altering the structure can influence this stability. We have also determined the electrochemical stability window of the chloride-enriched lithium argyrodite ( $Li_{5.5}PS_{4.5}Cl_{1.5}$ ) in both BM and HT samples and compared with the commercial lithium argyrodite ( $Li_6PS_5Cl$ ) by using linear sweep voltammetry. Additionally, we performed the electrochemical stability window of  $Li_6PS_5Br$ ,  $Li_{5.7}PS_{4.7}Br_{1.3}$  and  $Li_{5.5}PS_{4.5}Br_{1.5}$  composition. We observed the halide enriched lithium argyrodite show better electrochemical stability windows.

Overall in this thesis, the processing of halide enriched lithium argyrodite  $Li_{6-x}PS_{5-x}X_{1+x}$  (X = Cl and Br) exhibits cubic crystal structure, various occupancies of halide on 4d site with high ionic conductivity, and good electrochemical stability window to development of all solid-state batteries.

**Keywords:** Solid-State Batteries, Lithium Argyrodite, X-ray diffraction, Raman Spectroscopy, Electrochemical stability window.

#### Contents

A	knov	rledgements	ii
Αl	ostrac	t i	v
N	omen	elature xi	ii
1	Intro 1.1 1.2 1.3 1.4	Demand	1 1 2 2 3
2	2.1 2.2 2.3 2.4 2.5	Components of Solid-State Batteries  Working principle: Lithium Solid-State Batteries  2.2.1 Cell assembly  Ionic conduction  2.3.1 Activation Energy  2.3.2 Nernst equation  Solid electrolytes  1  2.4.1 Inorganic solid electrolyte  2.4.2 Overview of the Lithium argyrodite family	4 5 6 7 8 1 2 4 6 8
3	3.1 3.2	Research Question	20 20 21
4	4.1 4.2 4.3	Introduction 2 Experimental methods 2 4.2.1 Mechanochemical synthesis of lithium argyrodite 2 4.2.2 High temperature annealing 2 4.2.3 X-Ray powder Diffraction 2 4.2.4 Electrochemical Impedance spectroscopy 2 4.2.5 Raman spectroscopy 2 Results and discussion 2 4.3.1 XRD Results and lattice parameters 2 4.3.2 Site-disorder in lithium argyrodites 3 4.3.3 SEM morphology 3	22 23 24 25 27 27 27 33 44 36

Contents

	4.4 Experimental challenges	40 43 43
5	5.1 Introduction	45 45 46 46 47 50 52 54
6	6.1 Conclusion	<b>56</b> 56 58
A	A.1 Reitveld refined XRD patterns	66 66 75 76 80 80 81 82 82 83
В	B.1 Sodium solid electrolyte	87 87 87 88 88

#### List of Figures

1.1 1.2	Relative yearly electricity consumption from 2015-2025,[2]	1
1.2	diffusion from anode to cathode as the battery discharges,[11]	3
2.1	Schematic representation of the solid-state cell	4
2.2	Schematic representation of an SSB, depicting the flow of ions through solid electrolyte	5
2.3	Solid-state cell assembly	7
2.4	Diffusion pathways: (a) vacancy hopping, (b) interstitial hopping, and (c) interstitial	
	knock-off	8
2.5	Ion diffusion in the presence of electric field,[29]	9
2.6	Distribution of ions after the applied electric field,[29]	9
2.7	Potential energy barrier difference in the solid electrolyte,[28]	10
2.8	Slope of a plot of $\ln(\sigma T)$ vs $\ln(1/K)$ ,[29]	11
2.9	Comparison study of the different types of solid electrolytes,[30]	13
2.10	Classification of solid electrolytes	14
2.11	Ionic conductivity of the solid electrolyte including lithium and sodium composi-	
		14
2.12	Structural arrangement of inorganic solid electrolyte group (Green sphere represents	
	the lithium atoms),[58]	16
2.13	Cubic crystal of lithium argyrodite with halide anions X <sup>-</sup> and sulfide anions S <sup>-</sup> on the 4a and 4d site and (b) shows the presence of the lithium ions form cage like	
	structure in unit cell,[63]	17
2.14	Plot exhibiting the properties of the site disorder of the $(X^-/S^{2-})$ in the $Li_6PS_5X$ versus the ionic conductivity in mS $cm^{-1}$ and shows that $Li_6PS_5I$ exhibits the lower	
	, ,,,,,,,,,,,,,,,,,,,,,,,,,,,,,,,,,,,,,	17
2.15	(a) Cubic crystal lattice of the $Li_{6-x}PS_{5-X}X_{1+X}$ and the green spheres represents the halide (X), (b)lithium substructure cage showing the position of lithium in the	
	wyckoff sites 48h-24g-48h and the inter-cage jump between two lithium ion cages,[26]	18
2.16	Overall summary of the active challenges in the ASSB's,[66]	19
4.1		23
4.2		23
4.3		24
4.4	Plot of the AC potential $E(t)$ as input and the current density $j(t)$ as output, resulting	
		25
4.5	(a) Equivalent circuit of the solid electrolyte, (b) Schematic Nyquist plot of the	
		26
4.6	Schematic representation of the Raman scattering [74]	27

List of Figures ix

4.7	XRD patterns of $Li_6PS_5Cl$ under various conditions, including ball milling (BM) and	
	heat treatments (HT) at 200°C, 350°C, and 550°C with rhombus symbol over the	
	peaks representing the lithium argyrodite peak position	28
4.8	Refined XRD pattern and the lattice parameter of BM and annealing at 350°C and	
	550 °C $Li_6PS_5$ Cl composition	28
4.9	XRD patterns and the lattice parameter of $Li_6PS_5$ Br under various conditions,	
	including BM and HT at 350°C, and 550°C with the rhombus symbol over the peaks	
	representing the peak position of lithium argyrodite	30
4.10	XRD patterns of $Li_{5.5}PS_{4.5}Cl_{1.5}$ under various conditions, including BM and HT at	
	200°C, 350°C, and 550°C with the rhombus symbol over the peaks representing the	
	peak position of lithium argyrodite	30
4.11	1	
	Academia V4 showing the presence of $Li_{15}(PS_4)_4Cl_3$ and $LiCl$ impurity in the mixture	24
1 10	and (b) Lattice Parameters of $Li_{5.5}PS_{4.5}Cl_{1.5}$ at BM and various HT mixture	31
4.12	XRD patterns of $Li_{5.5}PS_{4.5}Br_{1.5}$ under various conditions, including BM and HT at	
	200°C, 350°C, and 450°C with the rhombus symbol over the peaks representing the	22
112	peak position of lithium argyrodite	32
4.13	Li <sub>5.5</sub> $PS_{4.5}Br_{1.5}$ , in which the refinement was done using TOPAS Academic V4 and (b)	
	Lattice Parameters of $Li_{5.5}PS_{4.5}Br_{1.5}$ at BM and various HT mixture	32
4 14	SEM images of $Li_6PS_5Cl$ (a) BM, and (b) HT $450^{\circ}c$ solid electrolyte was prepared by	32
7.17	high energy ball milling and high temperature annealing	34
4.15	SEM images of $Li_6PS_5$ Br (a) BM, and (b) HT $450^{\circ}$ c solid electrolyte was prepared by	01
1,10	high energy ball milling and high temperature annealing	35
4.16	SEM images of $Li_{5.5}PS_{4.5}Cl_{1.5}$ (a) BM, and (b) HT $450^{\circ}$ c solid electrolyte was prepared	
	by high energy ball milling and high temperature annealing	35
4.17	SEM images of $Li_{5.5}PS_{4.5}Br_{1.5}$ (a) BM, and (b) HT $450^{\circ}$ c solid electrolyte was prepared	
	by high energy ball milling and high temperature annealing	36
4.18	Raman spectra of BM and HT samples of $Li_6PS_5Cl$ and $Li_6PS_5Br$ showing the peak	
	and $PS_4^{-3}$	36
4.19	Raman spectra of BM and HT samples of $Li_{5.5}PS_{4.5}Cl_{1.5}$ and $Li_{5.5}PS_{4.5}Br_{1.5}$ showing	
	the peak and $PS_4^{3-}$	37
	Ionic conductivity and EIS fit with equivalent circuit of $Li_6PS_5Cl$ at room temperature	38
	Ionic conductivity and EIS fit with equivalent circuit of $Li_6PS_5$ Br at room temperature	38
4.22	Ionic conductivity and EIS fit with equivalent circuit of $Li_{5.5}PS_{4.5}Cl_{1.5}$ at room	20
4.00	temperature	39
4.23	Ionic conductivity and EIS fit with equivalent circuit of $Li_{5.5}PS_{4.5}Br_{1.5}$ at room	40
1 21	temperature	40
4.24	Arrhenius plot of the BM samples of Cl1, Br1, Cl1.5, and Br1.5 measured in varying temperatures from $0^{\circ}$ C to $-50^{\circ}$ C using the climate chamber	41
1 25	Arrhenius plot of the samples of Cl1, Br1, Cl1.5, and Br1.5 measured in varying	41
<b>4.2</b> 3	temperatures from $0^{\circ}$ C to $-50^{\circ}$ C	41
4 26	Activation energy of BM and HT samples of $Li_6PS_5Cl$ and $Li_6PS_5Br$	42
	Activation energy of BM and HT samples of $Li_{5.5}PS_{4.5}Cl_{1.5}$ and $Li_{5.5}PS_{4.5}Br_{1.5}$	42
4.28	Experimental challenges	43
	T	10

List of Figures x

5.1	Linear sweep voltammetry,[87]	46
5.2	Redox reaction showing lithium-ion diffusion with lithium ions (black dots) and the	
	vacant sites (empty holes)	47
5.3	Cell packing for linear sweep voltammetry to determine the electrochemical stability	
	window of the lithium argyrodite solid electrolyte	48
5.4	Postmortem of the packed cell showing the (a) Circumference and (b) thickness of	
	the cell	48
5.5	Postmortem of the cell packing retrieved after the linear sweep voltammertry showing	
	the (a) Anode side, (b) Cathode side, and (c) side view of cell	49
5.6	Electrochemical stability window of the LPSC (NEI corporation) commercial	50
5.7	Electrochemical stability window of the $Li_{5.5}PS_{4.5}Cl_{1.5}$ (BM)	51
5.8	Electrochemical stability window of the $Li_{5.5}PS_{4.5}Cl_{1.5}$ (HT 450°C)	51
5.9	Electrochemical stability window of the $Li_6PS_5Br$ (HT 550°C) Slow cooled	52
5.10	Electrochemical stability window of the $Li_{5.7}PS_{4.7}Br_{1.3}$ (HT 450°C) Slow cooled	53
5.11	Electrochemical stability window of the $Li_{5.5}PS_{4.5}Br_{1.5}$ (HT 450°C) Slow cooled versus	
	$In/Li^+$	53
5.12	Electrochemical stability window	54
6.1	Thin-film chlorine rich lithium argyrodite solid electrolyte with PTFE mixture	58
A.1	Refined XRD pattern of $Li_6PS_5Cl$ and $Li_6PS_5Br$	66
A.2	Refined XRD pattern of $Li_{5.5}PS_{4.5}Cl_{1.5}$ and $Li_{5.5}PS_{4.5}Br_{1.5}$	67
A.3	Refined XRD pattern of $Li_6PS_5Cl$ (HT 350°c) and $Li_6PS_5Br$ (HT 350°c)	67
A.4	Refined XRD pattern of $Li_6PS_5Cl$ (HT 350°c) and $Li_6PS_5Br$ (HT 350°c)	68
A.5	Refined XRD pattern of $Li_6PS_5$ Br (HT 550°c) and $Li_6PS_5$ Br (HT 350°c)	68
A.6	Refined XRD pattern of $Li_{5.5}PS_{4.5}Br_{1.5}(HT 450^{\circ}c)$	69
A.7	SEM images of (a) $Li_6PS_5Cl(BM)$ , (b) $Li_6PS_5Cl(HT~550^{\circ}C)$ , (c) $Li_6PS_5Br(BM)$ , and (d) $Li_6PS_5Br(HT~550^{\circ}C)$ solid electrolyte was prepared by high energy ball milling	
	and high temperature annealing in $50\mu$ m	75
A.8	SEM images of (a) $Li_{5.5}PS_{4.5}Cl_{1.5}$ (BM), (b) $Li_{5.5}PS_{4.5}Cl_{1.5}$ (HT 450°C), (c) $Li_{5.5}PS_{4.5}Br_{1.5}$	, .
11.0	(BM), and (d) $Li_{5.5}PS_{4.5}Br_{1.5}$ (HT 450°C) solid electrolyte was prepared by high energy	
	ball milling and high temperature annealing in $50\mu$ m	76
A.9	Ionic conductivity of the all the BM and HT 350°C samples	76
	Ionic conductivity of the all the HT samples at $450^{\circ}$ C and $550^{\circ}$ C including the $Li_6PS_5$ I	
	and $Li_{5.5}PS_{4.5}I_{1.5}$ measured at room temperature (298 K)	77
A.11	EIS fitted Nyquist plot of all the BM sample of lithium argyrodite using RelaxIS 3 .	77
	EIS fitted Nyquist plot of all the HT 350°C sample of lithium argyrodite using RelaxIS 3	78
	EIS fitted Nyquist plot of all the HT sample of lithium argyrodite using RelaxIS 3	79
	Arrhenius plot of the all the ball milled samples including the $Li_6PS_5I$ and $Li_{5.5}PS_{4.5}I_{1.5}$	
	measured from temperature ranging from $0^{\circ}$ c to $-50^{\circ}$ c	80
A.15	Pre-exponential factor of all the ball milled samples	80
	Pre-exponential factor of the heat treated samples	81
	Activation energy of BM and HT 350°C	81
	Activation energy of all the HT samples	82
	Raman spectra of BM and HT samples of $Li_6PS_5Cl$ and $Li_6PS_5Br$ showing the peaks	
	of PS <sub>4</sub> <sup>-3</sup>	82

List of Figures xi

	Raman spectra of BM and HT samples of $Li_{5.5}PS_{4.5}Cl_{1.5}$ and $Li_{5.5}PS_{4.5}Br_{1.5}$ showing	0.2
	<b>1</b> 4	83
	O)	83
	XRD pattern of both slow cooled and quenched samples showing the peaks of lithium argyrodite structure of $Li_{5.7}PS_{4.7}Br_{1.3}$ HT $450^{\circ}C$	84
	XRD pattern of both slow cooled and quenched samples showing the peaks of lithium	
		84
A.24	Electrochemical stability window representing the oxidation and the reduction of	
	- · · · · · · · · · · · · · · · · · · ·	85
A.25	Electrochemical stability window representing the oxidation and the reduction of	
	$Li_{5.7}PS_{4.7}Br_{1.3}$ HT $450^{\circ}$ c $LN_2$ Slow cooled samples	85
A.26	Electrochemical stability window representing the oxidation and the reduction of	
	$Li_{5.5}PS_{4.5}Br_{1.5}$ HT 450°c $LN_2$ Slow cooled samples	86
A.27	Electrochemical stability window of $LN_2$ cooled bromine enriched lithium argyrodite	86
B.1	X-Ray Diffraction patterns and ionic conductivity of $Na_{2+x}In_xHf_{1-x}Cl_6$ (X = 0, 0.25,	
	0.5. 0.75, 1)	88
	X-Ray Diffraction patterns and ionic conductivity of $Na_2Zr_xHf_{1-x}Cl_6$ (X = 0, 0.25,	
	0.5. 0.75, 1)	88
	X-Ray Diffraction patterns and ionic conductivity of $Na_2Zr_xHf_{1-x}Cl_6$	89

#### List of Tables

2.1	Reported ionic conductivities of inorganic solid electrolytes	15
4.1	Lattice Parameters, Volumes, and Interaxial Angles of $Li_6PS_5Cl$ at BM and various	
	HT compositions	29
4.2	Lattice Parameters, Volumes, and Interaxial Angles of $Li_6PS_5Br$ at BM and various	
	HT compositions	29
4.3	Lattice Parameters, Volumes, and Interaxial Angles of $Li_{5.5}PS_{4.5}Cl_{1.5}$ at BM and	01
4.4	various HT compositions	31
4.4	Lattice Parameters, Volumes, and Interaxial Angles of $Li_{5.5}PS_{4.5}Br_{1.5}$ at BM and various HT compositions	33
4.5	Table showing the site disorder of halide occupancies in 4d and 4a sites, and lattice	
	parameter of lithium argyrodite.	34
5.1	Electrochemical stability window of the chlorine rich lithium argyrodite solid elec-	
J.1	trolyte voltage versus $In/Li^+$	52
5.2	Actual electrochemical stability window of the Bromine rich lithium argyrodite solid	32
J.Z	electrolyte voltage versus $In/Li^+$	53
A.1	Crystallographic information of $Li_6PS_5Cl$ (BM)	69
A.2	Crystallographic information of $Li_6PS_5Br$ (BM)	70
A.3	Crystallographic information of $Li_{5.5}PS_{4.5}Cl_{1.5}$ (BM)	70
A.4	Crystallographic information of $Li_{5.5}PS_{4.5}Br_{1.5}$ (BM)	71
A.5	Crystallographic information of $Li_6PS_5Cl$ (HT 350°c)	71
A.6	Crystallographic information of $Li_6PS_5Br$ (HT 350°c)	72
A.7	Crystallographic information of $Li_{5.5}PS_{4.5}Cl_{1.5}$ (HT 350°c)	72
A.8	Crystallographic information of $Li_{5.5}PS_{4.5}Br_{1.5}$ (HT 350°c)	73
A.9	Crystallographic information of $Li_{5.5}PS_{4.5}Cl_{1.5}$ (HT 450°c)	73
	Crystallographic information of $Li_{5.5}PS_{4.5}Br_{1.5}$ (HT 450°c)	74
	Crystallographic information of $Li_6PS_5Cl$ (HT 550°c)	74
	Crystallographic information of $Li_6PS_5Br$ (HT 550°C)	75
A.13	Actual electrochemical stability window of the LPSB quenched samples	86

#### Nomenclature

#### **Abbreviations**

Abbreviation	Definition
ASSB	All solid-state batteries
BESS	Battery Energy Storage Systems
BM	Ball milled
CIF	Crystallography Information File
CNF	Carbon Nanofiber
CPE	Constant Phase Element
CV	Cyclic Voltammetry
EIS	Electrochemical impedance spectroscopy
IC	Ionic Conductivity
HT	Heat Treatment
LCO	Lithium-Cobalt-Oxide
LCOE	Levelized Cost of Electricity
LIB	Lithium-ion Battery
LISICON	Lithium Super Ionic CONductor
LMO	Lithium Manganese Oxide
LPSC/B	Lithium Phosphorous Sulfur Chlorine/Bromine
LSSB	Lithium Solid-State Batteries
LSV	Linear Sweep Voltammetry
MSD	Mean Squared Displacement
NMC	Nickel Manganese Cobalt
NMR	Nuclear Magnetic Resonance
OCV	Open Circuit Voltage
PAN	Polyacrylonitrile
PEEK	Polyether Ether Ketone
PEO	Polyethylene Oxide
PVDF	Polyvinylidene Fluoride
SE	Solid Electrolyte
SEI	Solid Electrolyte Interphase
SEM	Scanning Electron Microscope
SPE	Solid Polymer Electrolyte
SS	Stainless Steel
XRD	X-Ray Diffraction

## 1

#### Introduction

#### 1.1. Demand

After the Industrial Revolution, the world was set to compete with one another to meet the requirements of the rising population, which in return required energy as fuel for the manufacturing sectors [1]. The post-industrial revolution led to modern economies, resulting in a potential electricity consumption around the world. Global electricity demand worldwide has increased by 2% shortly after the pandemic and geopolitics, leading to high volatile prices, stagnant economic growth, and hyperinflation, [2].

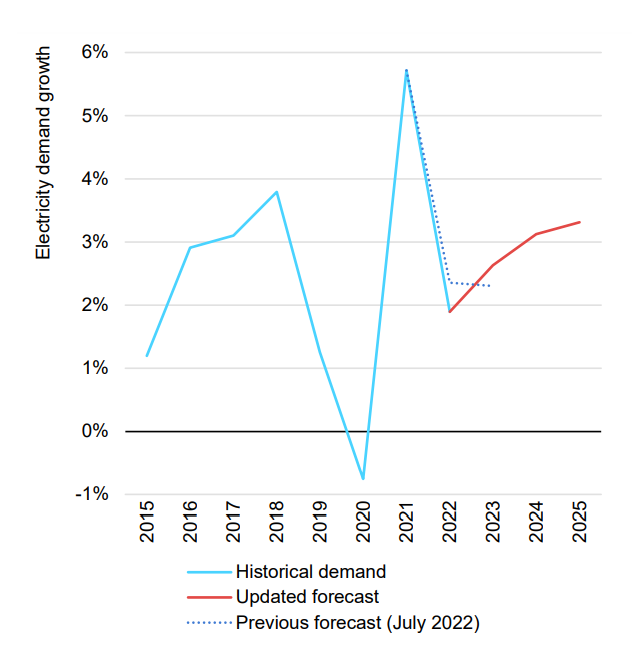


Figure 1.1: Relative yearly electricity consumption from 2015-2025,[2]

However by 2025, the annual consumption in developing countries such as China, India, and Southeast Asia are predicted to rise by 3%, while the rest of the world is expected to rise from 2.6% to 3.2% on an average[2]. As described above in the Figure 1.1 depicts the increasing growth trend of electricity consumption throughout the world from 2023.

#### 1.2. Energy Transition

According to the Paris Agreement, it states that the greenhouse gas emissions started from the pre-industrial period which is the primary cause of global warming and the subsequent rise in surface temperatures. The agreements to achieve the targeted global temperature rise within  $1.5^{\circ}$ C, [3]. Currently, electricity generation has predominantly relied on fossil fuels such as coal, oil, and natural gas to fulfill demand. However, this approach has resulted in the total  $CO_2$  emission of 37.15 Billion metric tons ( $GtCo_2$ ) in 2023[4].

This trend has compelled governments, and policymakers to transition from conventional fossil fuel-based power generation to renewable sources such as solar, wind, and biomass. These cleaner energy choices offer long-term alternatives that do not deplete finite fossil fuel reserves. Furthermore, the total installed renewable energy capacity and generation globally reached about 295 Gigawatts in 2020. Additionally, the levelized cost of electricity (LCOE) for renewable energy has decreased compared to fossil fuel power generation, making it more reliable and sustainable[5].

Now, one might wonder: how effortlessly is switching to renewable energy sources when the sun isn't shining and the wind isn't blowing?

In fact, not all seasons provide consistent solar irradiance or wind patterns, adding uncertainty to the grid system, which is not beneficial for end users. On the other hand, during the summer, the system may generate more power than required, but this surplus may be regulated via multiple Battery Energy Storage Systems (BESS) such as Lithium-ion batteries (LIB), Redox flow batteries, sodium-ion batteries, and solid-state batteries[6, 7].

#### 1.3. Batteries: a key to the sustainable energy

Batteries play a significant role in the energy transition in various aspects such as grid stability, Peak shaving, and renewable energy integration by making the renewable energy sector more stable and reliable[8]. The use of batteries provides advantages in addressing power inconsistencies from photovoltaic and wind energy by storing excess energy generated during peak production periods. This stored energy can then be discharged during off-peak hours, with the aim of reducing reliance on fossil fuel-based power generation[9].

The expansion of Battery Energy Storage Systems (BESS) in recent decades has increased drastically, driven by evolving technology and the low cost of production. It is expected to reach between 450 to 620 GWh of annual utility BESS capacity by 2030[10].

Most conventionally used battery in the various application and grid support system is the lithium ion battery (LIB). The LIB contains mainly of three major sections namely anode, cathode and the liquid electrolyte with polymer separator as shown in the below figure 1.2 as it represents the lithium ion to move from the anode to cathode during discharge and consecutively the electrons

move to meet at the outer circuit and vice versa [11].

The lithium ion battery consists of the following components as listed below,[11]:

- Electrode: Cathode (positive electrode) and Anode (negative electrode) acts as an storage facility for the lithium ions and electrons.
- Electrolyte: It acts as an transport medium for lithium ions between the electrodes and being more stable for both the electrodes.
- Current collectors: The collectors are used as a conductive material in the terminals.
- Separator: porous material is used to allow only the lithium ions to pass to other side.

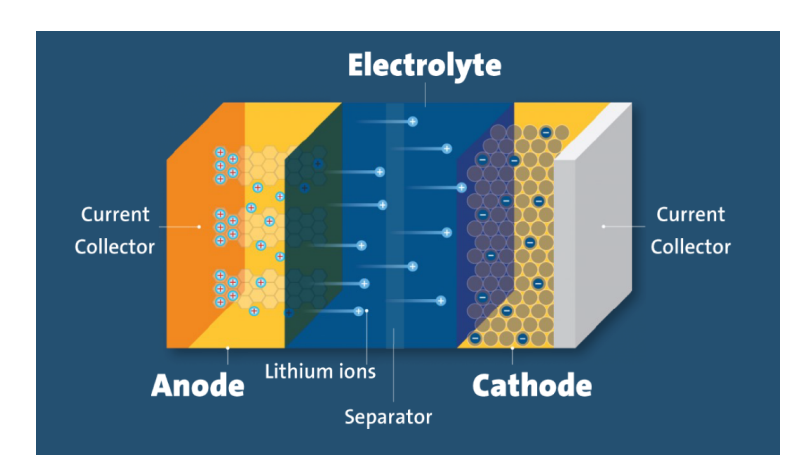


**Figure 1.2:** Schematic representation of the Lithium-ion battery showing the lithium ions diffusion from anode to cathode as the battery discharges,[11].

#### 1.4. Why Solid-State batteries?

The lithium-ion battery is the most widely used battery energy storage system (BESS) on the market. It comprises a liquid organic electrolyte known for its good ionic conductivity, and low self-discharge, [12]. However, these lithium-ion batteries are prone to high voltage charging that causes internal chemical reactions leading to short circuits, explosion, and thermal runaway[12, 13, 14].

Solid state batteries (SSBs) replace the flammable liquid electrolyte with solid which is much safer, long-cycle life, high energy density, and has similar conductivity compared to LIB [15]. This work will explore the lithium argyrodite as solid electrolyte due to its high ionic conductivity and better mechanical properties for electrolyte-electrode interface.

Chapter 2 will describe lithium solid-state batteries, including their theory, fundamentals, and working principles. In Chapter 3, an outline of the research questions will be set to help identify difficulties with the processing of the solid electrolyte. Chapters 4 and 5 will discuss experimental methods and results acquired, respectively. Finally, Chapter 6 will give overall conclusions and offer recommendations for further research.

## Lithium Solid-State Battery: Theory and Fundamentals

This chapter gives an insight into the components of solid-state batteries, cell assembly, and the working principle of solid-state batteries. Furthermore, the chapter looks into several family of solid electrolyte, describing its structure and properties, along with providing an outline of the lithium argyrodite solid electrolytes. The chapter concludes by focusing on the challenges and emerging patterns regarding resolving the challenges, providing an overview as the main focus of this thesis.

#### 2.1. Components of Solid-State Batteries

Solid-state batteries are packed with three dense layers of the cathode, solid electrolyte, and anode. The materials are placed in the solid-state battery as shown in the figure 2.1 with specific quantities inside the peek and certain pressure is applied over the cell to make the solid-solid connection between the active material and solid electrolyte, [16].

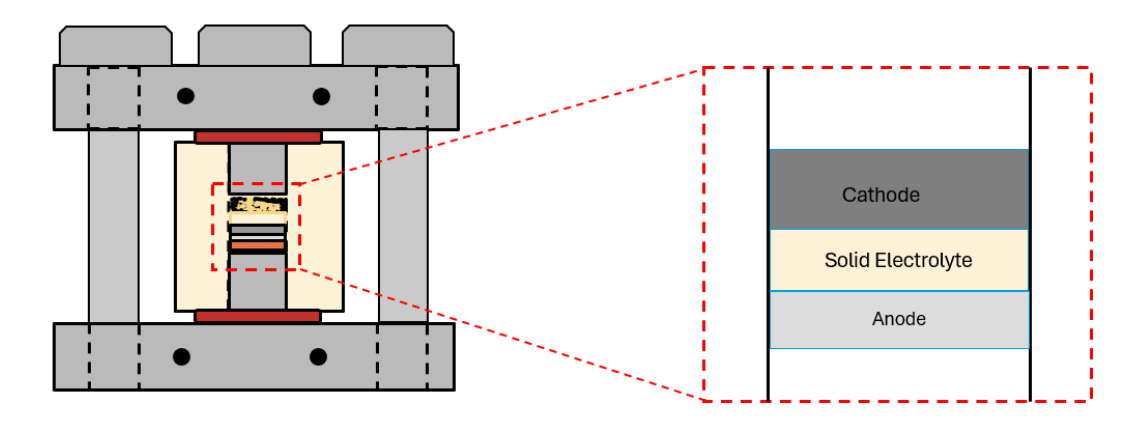


Figure 2.1: Schematic representation of the solid-state cell

Typically, the cathode composite material is prepared using NMC (LiCoO2 types intercalated type materials), solid electrolyte, and carbon fiber mixture to form the cathode composite. The presence of solid electrolytes and carbon in the cathode composition provides better ionic transport and electronic transport for improved cell performance[17].

The solid electrolyte is acts as a bridging material between both the electrodes. Solid electrolytes in solid-state batteries are categorized into three types: inorganic, organic, and hybrid electrolytes. Commonly used solid electrolytes are sulfides like Lithium argyrodite (LPSC), Lithium SuperIonic Conductors (LiSICON), and polymer-oxide based electrolytes such as LLZO-PEO, and hybrid solid electrolytes composed of both organic and inorganic materials as mentioned above, [17, 18, 19].

The anode in the solid-state batteries plays a important role in storing ions during the intercalations. Generally, graphite used as commercially available anode materials and has theoretical specific of 372 mAh/g but when replaced with the lithium metal anode with theoretical specific capacity of 3860 mAh/g could improve the higher energy density,[20]. All the components mentioned above make the solid-state batteries. However, the thesis mainly focuses on the solid electrolyte and their role in improving ionic conductivity and electrochemical stability window.

#### 2.2. Working principle: Lithium Solid-State Batteries

Previously in the above section, we discussed the components of the solid-state batteries, giving us a clear outline of the lithium solid-state batteries. This section describes the working principle behind the lithium solid-state batteries.

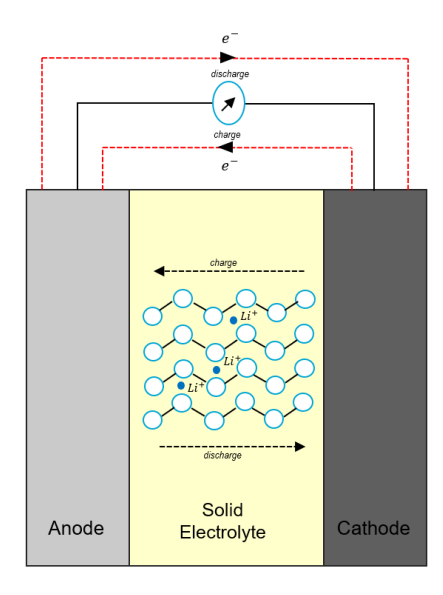


Figure 2.2: Schematic representation of an SSB, depicting the flow of ions through solid electrolyte

Generally, lithium solid-state batteries store the electrical energy by converting it to chemical energy by the redox reaction in both electrodes. The working principle in the solid state batteries are similar to the lithium ion batteries whereas the liquid electrolyte is replaced with the solid powder.

The full-cell reaction of the lithium solid-state battery is given below. The figure 2.2 below describes about the structure of solid-state batteries with lithium metal.

In the cathode, during discharging the lithium ions are lithiated towards the anode metal by reduction and by using the NMC it is shown in the half-reaction:

$$Li(Ni_xMn_yCo_z)O_2 \stackrel{\text{discharge}}{\rightleftharpoons} Li_{1-x}(Ni_xMn_yCo_z)O_2 + xLi^+ + e^-$$
(2.1)

similarly, due to oxidation in the anode metal, the lithium metal forms into lithium ions in the given reaction, [21, 22]:

$$xLi^{+} + e^{-} + In \underset{\text{charge}}{\overset{\text{discharge}}{\rightleftharpoons}} Li_{x}In$$
 (2.2)

The overall cell reaction of the lithium solid-state battery from the equation 2.1 and 2.2:

$$Li(Ni_xMn_yCo_z)O_2 + In \stackrel{\text{discharge}}{\rightleftharpoons} Li_{1-x}(Ni_xMn_yCo_z)O_2 + Li_xIn$$
 (2.3)

The equation 2.3 describes the overall cell reaction on both electrodes making the lithium ions diffuse from cathode to anode during the cell discharge,[21, 22].

The figure 2.2 illustrates the flow of ions between the cathode and anode metal with respect to charging and discharging which makes the electrons move in the external circuit due to the potential difference between the electrodes.

#### 2.2.1. Cell assembly

The figure 2.3 below illustrates about the assembly of solid-state cell for electrochemical stability window with all three components inside the polyether ether ketone (PEEK). A stainless steel frame holds the PEEK between two electrode tips which are in contact with the active materials. Both sides of the electrode tips contain an O-ring which prevents exposure to the atmosphere.

Within the PEEK casing, the active materials are stacked in order of cathode, SE, and anode, respectively [23]. The SS frame with three screws intact over the frame helps to hold the top and bottom at a certain pressure and screws are covered with the plastic washer to avoid the short-circuit between the electrodes. Basically, by applying pressure over the cell reduces the voids and increases the connection between the particles, thereby improving the lithium ion mobility for long range, [24]. Connection nodes on the electrodes facilitate the external connection for further testing of the cell.

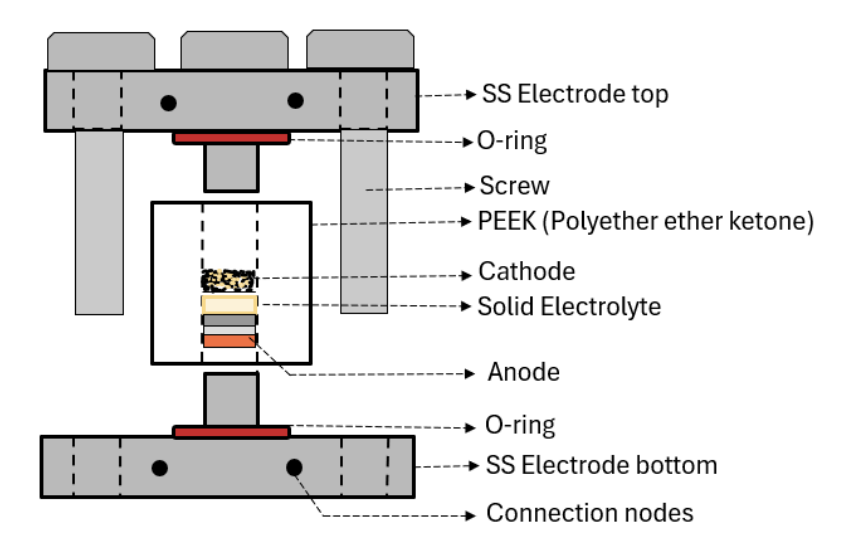


Figure 2.3: Solid-state cell assembly

Electrochemical impedance spectroscopy measurement, the customized solid-state cell is used, having electrodes with a diameter of 10 mm and a PEEK housing weight of 200 mg. An applied pressure of 392 MPa is exerted on the solid electrolyte to determine the ionic conductivity.

Electrochemical stability window setup, cell configuration was used with Li/In metal as the anode to facilitate the redox reaction of the solid electrolyte and determine its stability window till the stable decomposition of solid electrolyte, [25]. In this thesis work, cell was initially packed with 85 mg of solid electrolyte and applied the pressure of 314 MPa for 5 minutes using an automatic hydraulic press, without the O-ring. Subsequently, the top side of the cell was filled with cathode composite mixture. In this work, the cathode material was hand-grinded and used the same pressure conditions mentioned earlier. The cell was retrieved and filled with Li-In, with a copper current collector placed on the anode, and subjected to the closing pressure of 62 MPa for 3 minutes. However, this thesis mostly focuses on the structure and ionic transport correlations and stability windows, next section, we will discuss the ionic conduction mechanism.

#### 2.3. Ionic conduction

The ionic conductivity is proportional to the mobility of ions. To improve ionic conductivity, increasing ion mobility or increasing the charge carrier density, as shown in equation 2.4, is important. The ionic conductivity ( $\sigma$ ) of solid electrolyte is expressed as given below,[26]:

$$\sigma = nZe\mu \tag{2.4}$$

where,

- $\sigma$ : Ionic conductivity of the solid electrolyte.
- *n*: Active carrier density
- Ze: The charge of the ion

•  $\mu$ : Mobility of the ions.

The mobility of ions is inversely proportional to temperature, which indicates temperature change may significantly affect ion mobility as shown in the equation 2.5,[26].

$$\mu \propto \frac{nE_a}{k_B T} \tag{2.5}$$

where,

- $\mu$ : Mobility of the ions.
- $E_a$ : Activation energy for ion movement.
- *k*<sub>B</sub>: Boltzmann constant.
- *T*: Temperature.

Relatively, apart from defects in solid crystals ionic conductivity occurs due to the diffusion pathway and it can be further categorized into three types known as vacancy hopping, interstitial hopping, and interstitial knock-off as shown in figure 2.4.

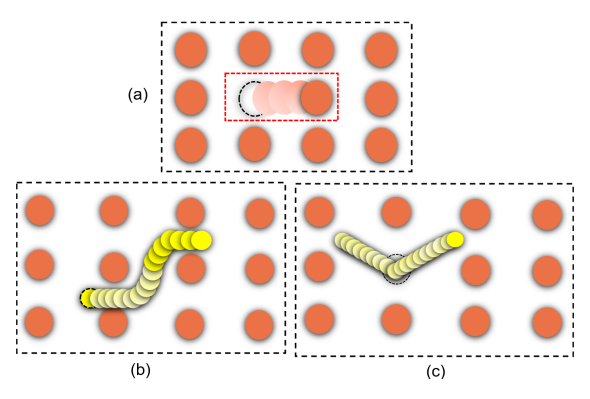


Figure 2.4: Diffusion pathways: (a) vacancy hopping, (b) interstitial hopping, and (c) interstitial knock-off

Vacancy hopping occurs within the crystal lattice structure when ions or atoms occupy empty or vacant sites due to Schottky defects, resulting in excess vacancies for direct ion transport. Similarly, in the interstitial mechanism, interstitial ions migrate to nearby Frenkel defects via interstitial vacancies. On the other hand, in the interstitial knock-off mechanism, an interstitial ion replaces an atom by eliminating it from the lattice structure. This produces multiple defects which increases the ion mobility,[27].

#### 2.3.1. Activation Energy

Activation energy is the minimum energy required for an atom or ion to hop from one site to another within the crystal lattice framework. Each solid electrolyte exhibits its own energy landscape depending on which the activation energy varies. In order to achieve higher ionic conductivity, there should be a low activation energy barrier and an increased number of ion mobilities and vacancies, [28].

The effect of ion diffusion in the presence of an electric field, when an external electric field is applied over the system makes the ions move in both directions based on the charge conditions. Figure 2.5 illustrates how the electric field decreases the ion barrier in one direction while increasing it in the other. This figure depicts the potential barrier to ion diffusion generated by the applied electric field. In this context,  $Z_e$  is the ion charge, a is the jump distance,  $E_v$  is the electric field, and  $\Delta g_m$  is the potential energy barrier height,[29].

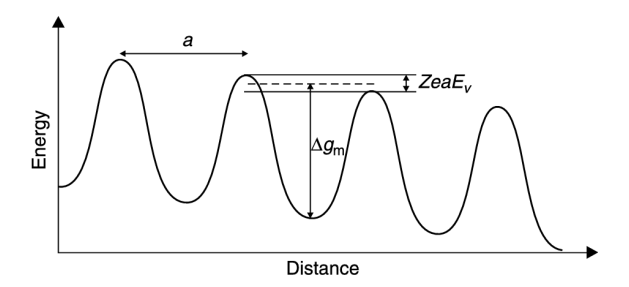


Figure 2.5: Ion diffusion in the presence of electric field,[29]

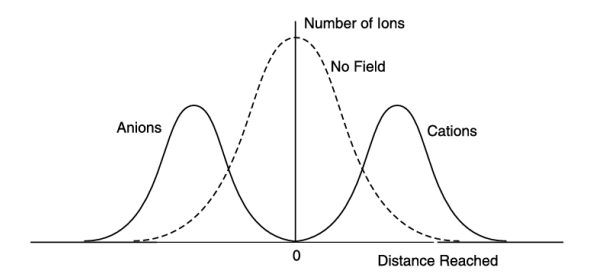


Figure 2.6: Distribution of ions after the applied electric field,[29]

The figure 2.6 describes the ion distribution after applied the electric field which shows us the diffusion of ions based on the electric field as shown in the figure, the anions and cations moves depending upon on the charge distribution and causing the diffusion of ions. The shift in the electric field causes ions to migrate within the crystal lattice. Figure 2.7 illustrates how the movement of ions varies based on the energy barrier. It describes that the higher the energy barrier, the higher the activation energy of the ion and vice versa, [28].

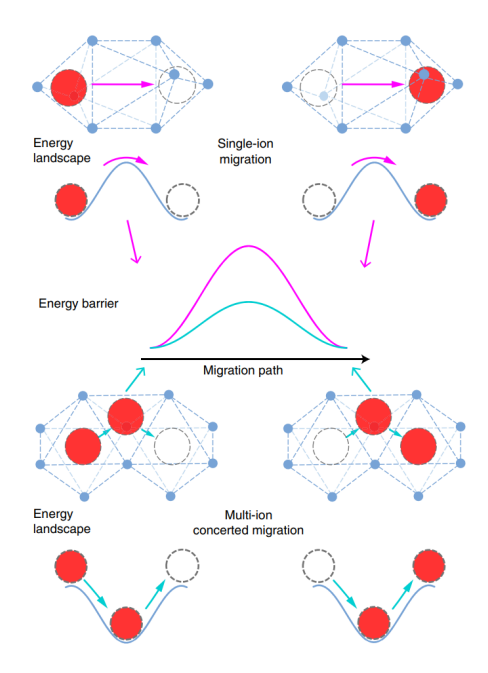


Figure 2.7: Potential energy barrier difference in the solid electrolyte,[28]

The above figure 2.7 shows us the potential energy barrier in the single and multi ion migration. Due to the change in energy landscape, the potential energy barrier can significantly change as shown in the figure migration pathway which gives us the highest energy barrier  $E_a$ ,[28]. The main difference of single ion diffusion in the framework shows the individual ion migrating from one side to other, similarly the multiple ion diffusion is denoted to be the multi ion diffusion.

Mathematically, the activation energy can be expressed using the equation 2.6 below, [29]:

$$\sigma T = \sigma_0 \exp\left(\frac{-E_a}{RT}\right) \tag{2.6}$$

where,

- $\sigma T$ : Ionic Conductivity with temperature (T)
- $\sigma_0$ : Constant
- *E<sub>a</sub>*: Activation energy
- R: Gas constant
- T: Temperature

The equation 2.6 indicates the ionic conductivity of the solid electrolyte with respect to the temperature (T) as it shows that a increase in temperature can increase the ionic conductivity of the ions. By taking the logarithm on both sides of the equation 2.6, we get [29]:

$$ln\sigma + lnT = ln\sigma_0 - \frac{E_a}{RT}$$
 (2.7)

To get the activation energy, the slope value is obtained from the plot of  $\ln(\sigma_T)$  vs  $\ln(1/K)$  as shown in the below figure 2.8 whereas it is used to measure the energy barrier. The slope value is multiplied with the Boltzmann constant of  $1.380649 \times 10^{-23}$  joule per kelvin (K) to obtain the activation energy.

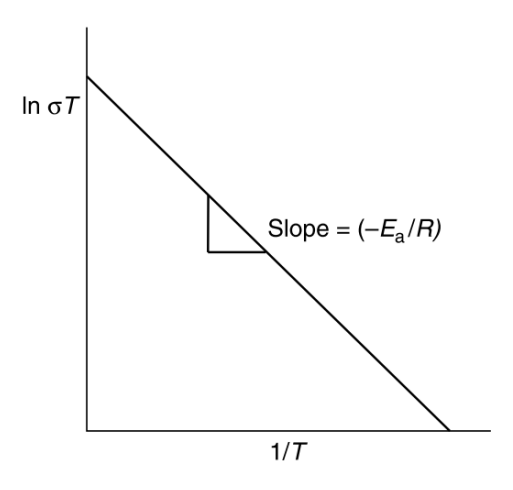


**Figure 2.8:** Slope of a plot of  $ln(\sigma T)$  vs ln(1/K),[29]

#### 2.3.2. Nernst equation

The electrochemical cell has two electrodes and they are connected with the ion conducting solid electrolyte. The potential difference across the battery is related with respect to Gibbs energy of the reaction in the cell and it is expressed as  $\Delta G_r$  in the equation 2.8:

$$\Delta G_r = -nE_{cell}F\tag{2.8}$$

where,

- $\Delta G_r$ : Gibbs energy of the cell reaction
- n : Number of moles of electrons involved in the cell reaction
- *E*<sub>cell</sub> : Cell potential (volts)
- F: Faraday constant

Here, the relation between the cell potential and concentration of components in the cell are interrelated as expressed in the below equation 2.9,[29]:

$$\Delta G_r = RT ln(\frac{Q}{K}) \tag{2.9}$$

where,

- $\Delta G_r$ : Gibbs energy of the cell reaction
- R : Gas constant  $(8.314 \frac{J}{mol.K})$

- T : Temperature (K)
- Q: Reaction quotient
- K: Equilibrium constant

By equating both the equation 2.8 and 2.9, we get:

$$\Delta G_r = -nE_{cell}F = RTln(\frac{Q}{K})$$
 (2.10)

$$-nE_{cell}F = RTln(\frac{Q}{K})$$
 (2.11)

The cell potential can be denoted as the below equation due to the cell equilibrium constant:

$$E_{cell} = -(\frac{RT}{nF})(\ln \frac{Q}{K}) \tag{2.12}$$

$$E_{cell} = -(\frac{RT}{nF})(lnQ - lnK)$$
(2.13)

$$E_{cell} = \left(\frac{RT}{nF}\right) lnK - \left(\frac{RT}{nF}\right) lnQ \tag{2.14}$$

The Q=1 (lnQ=0) when all the species are standard and the standard cell potential is denoted as  $E^0$ , [29]:

$$E_{cell} = E^0 - \left(\frac{RT}{nF}\right) lnQ \tag{2.15}$$

the above equation can be written in general terms as given below and it is known as the Nernst equation:

$$E_{cell} = E^0 - (\frac{RT}{nF})ln(\frac{Product}{Reactant})$$
 (2.16)

The below equation is written for the cell reaction as shown in the equation 2.3 for the solid state cell:

$$\Delta E = E_c^{\circ} - E_a^{\circ} + \frac{RT}{F} ln \frac{[LiIn][NMC]}{[In][LiNMC]}$$
(2.17)

#### 2.4. Solid electrolytes

This section discusses the classification of solid electrolytes used in solid-state batteries. Conventional liquid electrolytes in lithium-ion batteries pose risks over time, and flammable liquid electrolyte which raises significant reliability and safety concerns,[22].

As discussed previously in section 2.2, the development of solid-state batteries is based on one of the advancements in the ionic conductivity of solid electrolytes. This particular improvement enhances the charging rate and increases the energy density,[30]. The comparative study of various electrolytes is shown in the figure 2.9 along with their characteristics.

From figure 2.9, it illustrates the differences and the similarities between the liquid electrolyte and the solid electrolyte which shows the characteristics and properties such as ionic conductivity,

safety, electrochemical stability, processability, thermal stability, mechanical strength, and interfacial contact. Furthermore, the inorganic ceramic electrolyte exhibits better ionic conductivity and safety compared to all other electrolytes but processability of these materials are quite harder as their air sensitive material, [30].

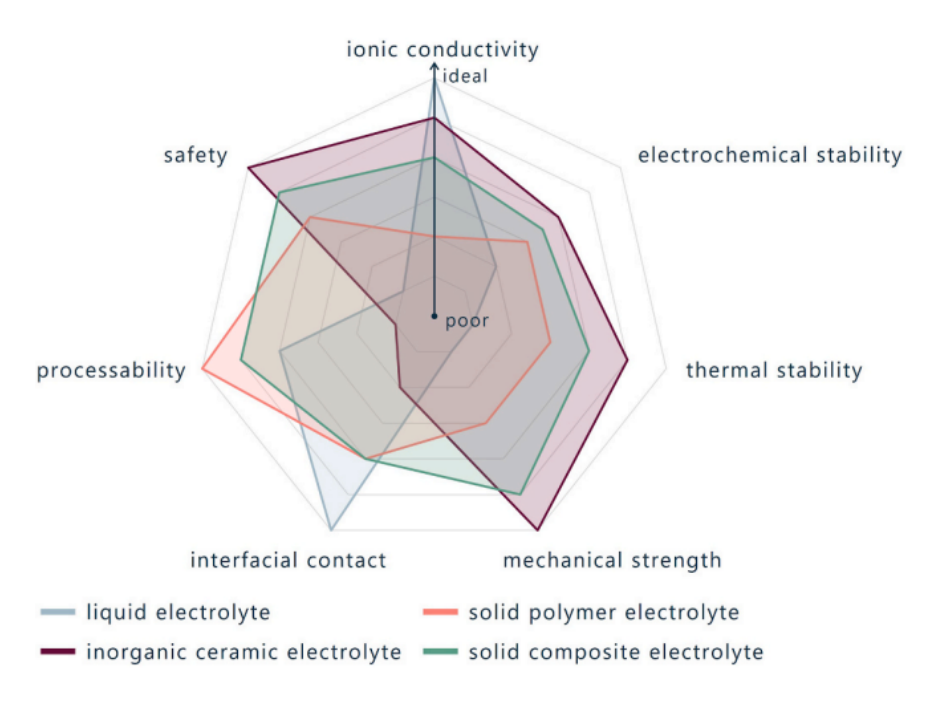


Figure 2.9: Comparison study of the different types of solid electrolytes,[30]

These solid electrolytes can be categorized into distinct sections called inorganic, solid polymer electrolyte (SPE). and solid composite as given in the figure 2.10. Commonly used inorganic solid electrolytes such as oxide, sulfides, thio-LISICON, and argyrodite. Similarly, the solid polymer electrolytes commonly used include PEO-LiBF<sub>4</sub>, PAN-based electrolytes, and polyvinylidene fluoride (PVDF),[30, 31]. However, the polymer-based electrolyte has low ionic conductivity and cycles the cell at higher temperatures hindered commercial applications.

To make a better solid electrolyte for the solid-state batteries, the solid electrolyte should have the following key criteria as follows,[32]:

- Better ionic conductivity
- Wide range of electrochemical stability window
- Better interfacial contact between the electrodes and the solid electrolyte
- Good mechanical strength to suppress the Li dendrites
- Economically feasible

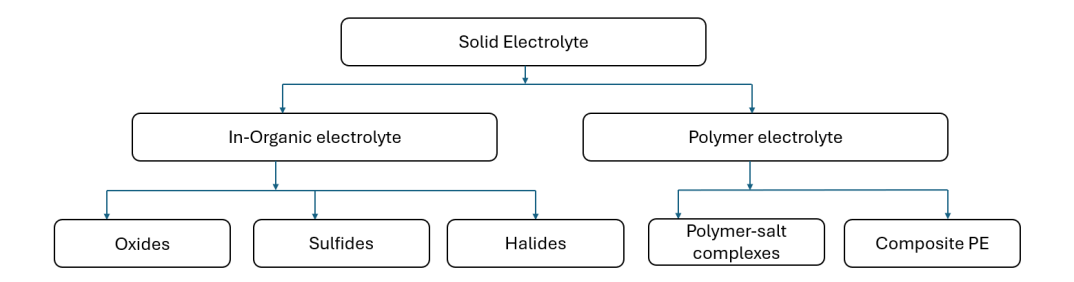


Figure 2.10: Classification of solid electrolytes.

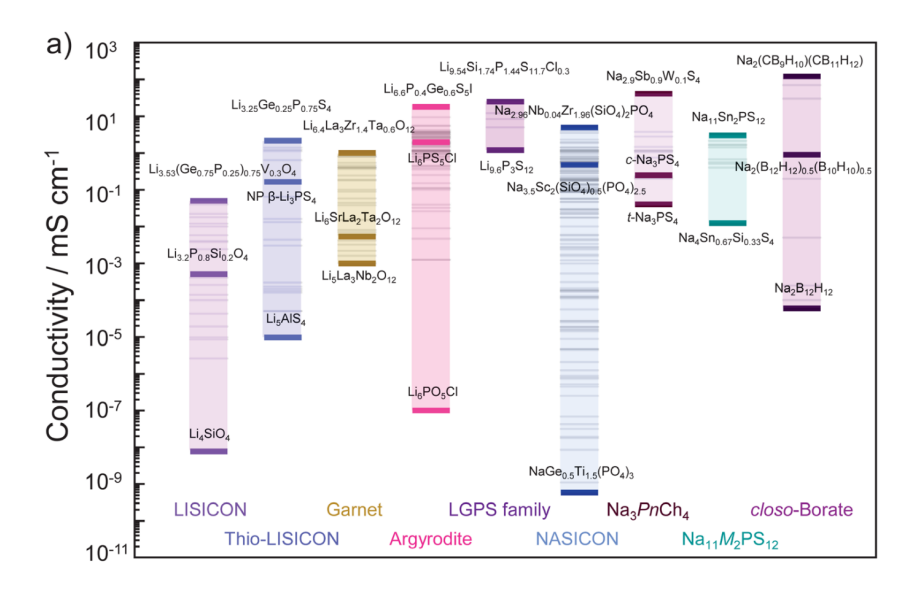


Figure 2.11: Ionic conductivity of the solid electrolyte including lithium and sodium compositions,[33]

Recent study shows the ionic conductivity and magnitude of the various other composition including lithium and sodium composition as shown in the figure 2.11 and lithium argyrodite occupies the magnitude range of  $10^1$  to  $10^{-7}$  mS  $cm^{-1}$ ,[33].

#### 2.4.1. Inorganic solid electrolyte

Inorganic solid electrolytes are a type of electrolyte as inorganic compounds that help the lithiumions to move through the crystal structure and have similar lithium mobility compared to liquid electrolytes. Recent studies have shown that inorganic solid electrolyte exhibits higher ionic conductivity, improved safety, long-cycle life, and better mechanical strength[34]., which makes the solid-state batteries safer and better compared to the conventional lithium-ion batteries by suppressing the lithium dendrite growth formation,[35].

Inorganic Solid Electrolyte	Ionic conductivity (S cm <sup>-1</sup> )	Temperature (°K)	References
Oxides			
$Li_4GeO_4$	$2.9 \times 10^{-6}$	298	[36]
$Li_{29}Zr_9Nb_3O_{40}$ (LZNO)	$5.90 \times 10^{-5}$	298	[37]
Perovskite			
$Li_{0.17}La_{0.61}TiO_3$	$3.76 \times 10^{-4}$	298	[38]
$Li_{0.38}Sr_{0.44}Ta_{0.7}Hf_{0.3}O_{2.95}F_{0.05}$	$4.89 \times 10^{-4}$	298	[39]
$LiSr_{0.95}TiTaO_{5.9}F_{0.1}$	$3.67 \times 10^{-4}$	298	[40]
Anti-Perovskite			
Li <sub>2</sub> OHCl	$2.8 \times 10^{-3}$	468.15	[41]
$Li_3OCl_{0.5}Br_{0.5}$	$1.94 \times 10^{-3}$	298	[42]
Garnet			
$Li_7La_3Zr_2O_{12}$ (LLZO)	$3.10 \times 10^{-4}$	298	[43]
$Li_{6.5}La_3Zr_{1.75}Te_{0.25}O_{12}$ (LLZTO)	$1.02 \times 10^{-3}$	303	[44]
$Li_{6.6}La_{3}Zr_{1.6}Sb_{0.4}O_{12}$	$7.70 \times 10^{-4}$	303	[45]
Sulfides			
$\text{Li}_3\text{PS}_4$	$4 \times 10^{-4}$	298	[46]
$Li_{10}Si_{0.3}Sn_{0.7}P_2S_{12}$	$8.0 \times 10^{-3}$	298	[47]
$Li_{11}AlP_2S_{12}$	$8.02 \times 10^{-4}$	298	[48]
Halides			
$Li_2ZrCl_6$	$2.1 \times 10^{-3}$	303.15	[49]
$Li_3InCl_6$	$1.03 \times 10^{-3}$	298	[50]
NASICON-based			
$Li_{1.3}Al_{0.3}Ti_{1.7}(PO_4)_3$ (LATP)	$3.0 \times 10^{-3}$	298	[51]
$Li_{1.6}Al_{0.6}Ge_{0.8}(PO_4)_3$	$0.70 \times 10^{-3}$	298	[52]
LISICON			
$Li_{9.6}P_3S_{12}$	$1.00 \times 10^{-2}$	298	[53]
$Li_{10}GeP_2S_{12}$	$1.20 \times 10^{-2}$	298	[54]
$Li_{3.4}Si_{0.4}P_{0.6}S_4$	$6.4 \times 10^{-4}$	298	[55]
Argyrodite			
$\mathrm{Li_{10}P_3S_{12}Br}$	$5.8 \times 10^{-3}$	300	[56]
$Li_{10.25}P_3S_{12.25}I_{0.75}$	$9.1 \times 10^{-3}$	300	[56]
$Li_{6.5}Sb_{0.5}Ge_{0.5}S_5I$	$16.1 \times 10^{-3}$	298	[57]

Table 2.1: Reported ionic conductivities of inorganic solid electrolytes

The table 2.1 shows several reported ionic conductivity values for the various inorganic solid electrolytes, corresponding to the structural arrangements as shown in figure 2.12. The position of the lithium ions in the structural arrangement are denoted as green spheres. These variations are most likely caused by changes in crystal lattice structure, defects, and ion pathways, all of which have an impact on ionic conductivity and transportation,[58]. Out of all the reported solid electrolyte, the lithium argyrodite exhibits the higher ionic conductivity while compared to all other solid electrolyte including the oxides, and the halides. The lithium argyrodite has intrinsic anionic site-disorder which resulting in the improved lithium ion conduction,[59] and its discussed in the coming subsection 2.3.2.

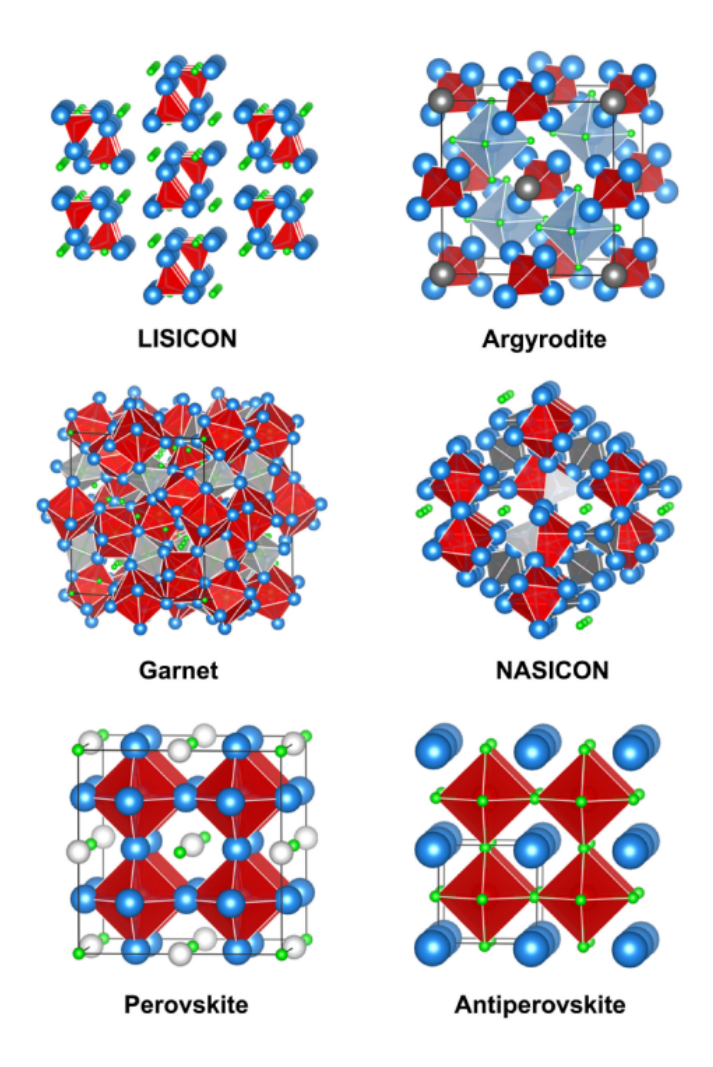


Figure 2.12: Structural arrangement of inorganic solid electrolyte group (Green sphere represents the lithium atoms),[58]

#### 2.4.2. Overview of the Lithium argyrodite family

As we discussed previously, the electrochemical properties and behaviour of all solid electrolyte exhibits broad range of ionic conductivity. Here, this section will tells us about the the overall view of the lithium argyrodite family and describes about the structural arrangement.

The lithium argyrodite has significantly higher ionic conductivity in the solid electrolyte group at room temperature making it highly reliable, and safer option to replace the liquid electrolyte. Initially, the lithium argyrodite was discovered from the family argyrodites form of mineral structure  $Ag_8GeS_6$ , also used as ion conductors by substituting in  $Ag_7PS_5X$  but later it was replaced with  $Li^+$  and halide (X) to form  $Li_6PS_5X$  (X= Cl,Br,I)[60, 61].

The halide substitution in the orthorhombic structure ( $Li_7PS_6$ ), replaces the unbound  $S^{2-}$  anions

by the halide  $X^-$  anion to form  $Li_6PS_5X$  which stabilized the cubic polymorph at room temperature and exhibits the crystal structure of F43m space group, As the figure 2.13 shows the position of the halide occupancy at the 4a site and the P and S are bounded with P as centered atom at the wyckoff 4b site and S occupancy at 16e site forming the  $PS_4^{-3}$  polyhedral structure.[61]. The free sulfur anions ( $S^{2-}$ ) occupying at Wyckoff 4d site. Lithium-ion distribution form the cage like structure around free 4d site is shown in the (b). Based on the composition, the occupancy of the halide and the free sulfur  $S^{2-}$  anions varies at the Wyckoff 4d site which is considered as the site disorder,[62].

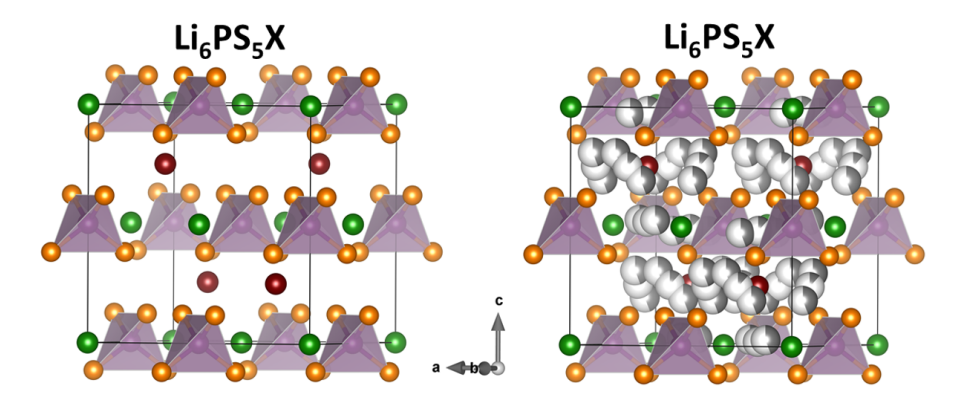


**Figure 2.13:** Cubic crystal of lithium argyrodite with halide anions X<sup>-</sup> and sulfide anions S<sup>-</sup> on the 4a and 4d site and (b) shows the presence of the lithium ions form cage like structure in unit cell, [63]

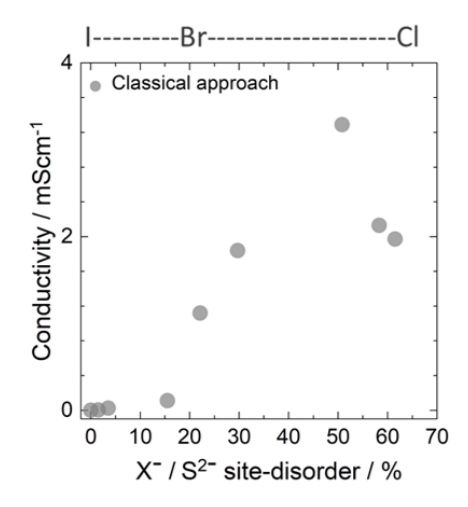


**Figure 2.14:** Plot exhibiting the properties of the site disorder of the  $(X^-/S^2^-)$  in the  $Li_6PS_5X$  versus the ionic conductivity in mS  $cm^{-1}$  and shows that  $Li_6PS_5I$  exhibits the lower ionic conductivity while compared to the Cl,Br,[59]

The percentage of site disorder varies based on the halide (X= Cl, Br, and I) in lithium argyrodite structure due to their change in ionic radii size ( $Cl^-$ = 181 pm,  $Br^-$ = 196pm, and  $I^-$ = 220pm).  $Cl^-$ 

and  $Br^-$  based lithium argyrodites exhibits the site disordered due to their similar ionic radii with the sulfur anion ( $S^{2-}$ = 184 pm) whereas in the case of iodine ( $I^-$ ) the shows no site disorder due to the large ionic radii mismatch, which limits the ionic conductivity lower than the magnitude of  $10^{-3}$  mS  $cm^{-1}$ , this shows the presence of site disorder improves the ionic conductivity as shown in the figure 2.14.

The figure 2.15 (a) shows the cubic crystal structure of  $Li_{6-x}PS_{5-X}X_{1+X}$  consists of lithium ion cage formation between the free sulfur atoms and in figure 2.15 (b) shows the two lithium ion cages occupying next to each other in the cubic structure and its occupancy also depends on the unit cell volume, and material composition. The lithium ion conduction with-in the cage are intra-cage, doublet jumps and jump between two lithium ion cages is called inter-cage jump,[26].

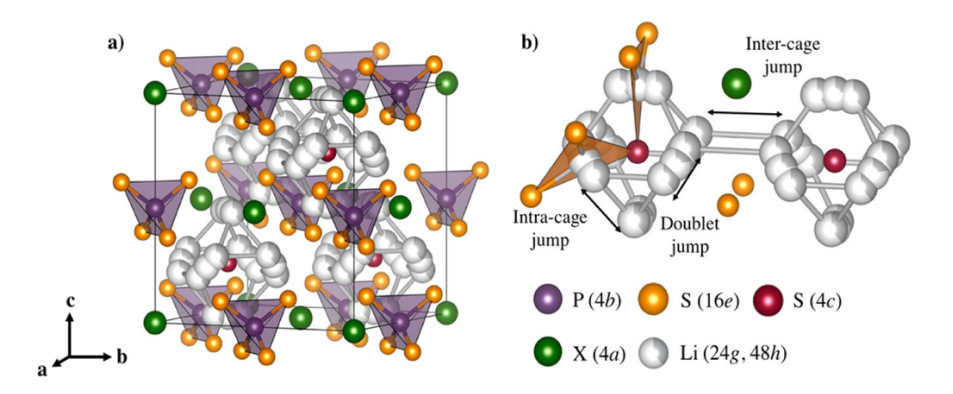


**Figure 2.15:** (a) Cubic crystal lattice of the  $Li_{6-x}PS_{5-X}X_{1+X}$  and the green spheres represents the halide (X), (b)lithium substructure cage showing the position of lithium in the wyckoff sites 48h-24g-48h and the inter-cage jump between two lithium ion cages,[26]

The lithium transport within the same cage, from 48h-48h Wyckoff site involves intra-cage jumps. Similarly when lithium move between the 48h to 24g to 48h of the same cage is referred to as a doublet, while the inter-cage jump occur when the lithium moves between two cages, from one 48h to other 48h Wyckoff site,[26]. These inter-cage jumps play a crucial role in long-range lithium ion mobility. Literature suggests that particularly in  $Li_6PS_5I$ , jumps within the cage (known as intra and doublet jumps) result in lower ionic conductivity. In contrast,  $Li_6PS_5CI$  and  $Li_6PS_5Br$ , which exhibit higher disorder, demonstrate more inter-cage jumps and, consequently, higher ionic conductivity. Furthermore, the structure of lithium argyrodite can be altered by enriching the bromide and chloride content, which influences both structure and ionic transport. In this thesis, we show how changes in synthesis parameters and the structure of bromide and chloride in lithium can improve ionic conductivity and electrochemical stability. [59].

#### 2.5. Active challenges

As above mentioned, we have covered the components and working principle behind the solid state batteries and there dominance over the liquid electrolyte in terms of a safer and more reliable alternative by replacing with the solid electrolyte, and one of the key aspect is the solid electrolyte which attributes towards the high ionic conductivity and open framework between the electrodes.

Beforehand, the conventional lithium ion battery are subjected to have various active challenges such as lithium-ion diffusion, lithium dendrite formation, contact loss between the active material in

the cathode region, safety concerns at high operating temperature conditions and degradation. The above mentioned constraints can cause short circuiting, capacity loss and thermal runaway, respectively, [64].

Currently the aim towards the solid-state batteries has increased due to its high performance with better capacity retention and the energy density. However, the ASSB's relatively exhibits the difficulties in transforming from pilot scale to intense large scale production,[65].

We choose the lithium argyrodite for the further development, its because of the high ionic conductivity and electrochemical stability while compared to other inorganic solid electrolyte exhibiting around  $10^{-2}$  to  $10^{-3}$  S  $cm^{-1}$  as shown in the table 2.1.

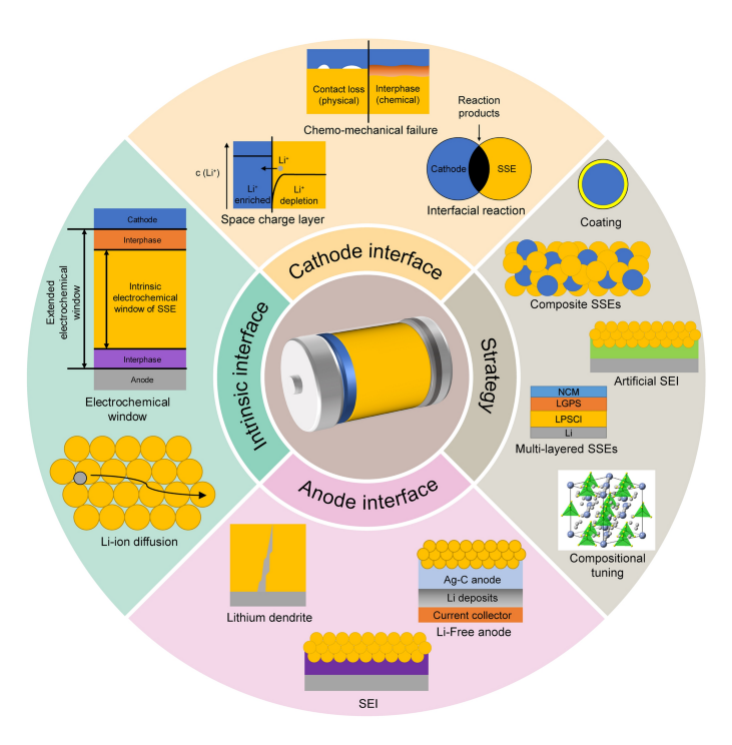


Figure 2.16: Overall summary of the active challenges in the ASSB's,[66]

This section describes the active challenges and part few of them are addressed and discussed from the further development in the solid electrolyte and their stability by specifically focusing in the intrinsic interface and the composition tuning strategy to achieve better ionic conductivity and the electrochemical stability,[66] as shown in the figure 2.16. As mentioned previously, the composition tuning helps to achieve a better ionic conductive material and by achieving more crystalline compound for better results and by improving the mechanical strength of the solid electrolyte can prevent the lithium dendrite formation which secures the battery from short-circuiting.

## Research questions and Thesis outline

This chapter provides the main research question and the sub-questions addressing the key problems in the optimization of solid electrolyte and the providing an outline of the following thesis work. The main research question is designed in such a way in order to encounter the problems and achieve a better ionic conductivity and the electrochemical stability window of the solid electrolyte.

By clearly providing an road map to solve these research questions and explaining the different methods and characteristics tools used to understand the problem and provide the strategic approach to solve them.

#### 3.1. Research Question

In this thesis, the main research question investigated are given below:

"How does structural parameter impacts the ionic conductivity, and the electrochemical stability window of halide enriched substitution in the lithium argyrodite sulfide solid electrolyte in solid-state batteries?"

For a better solution, the main research question is divided into following sub-questions and are addressed in the following chapter:

- How lithium argyrodite sulfide with halide enriched substitution are made and how does the annealing process impact in the ionic conductivity of the solid electrolyte?
- Structural parameter such as lattice parameter, site disorder influencing the ionic conductivity in lithium argyrodite?
- what is the difference in electrochemical stability window while compared with the commercial lithium argyrodite and the halide-rich composition?

3.2. Thesis outline

# 3.2. Thesis outline

In this thesis report, the first two chapters, Introduction and Chapter 2, provide the requirements of the battery in the energy transition, the basic fundamentals of solid-state batteries, the working principle of solid-state batteries, and the active challenges.

Chapter 4 in this thesis discusses the synthesis of lithium argyrodite solid electrolyte with enriched halide substitution (X = Cl, Br) using mechano-chemical synthesis and high-temperature annealing. This chapter provides insight into the differences between the ball-milled sample and the heat-treated sample. The material was characterized using various tools such as X-ray diffraction (XRD), scanning electron microscopy (SEM), Raman spectroscopy, and electrochemical impedance spectroscopy (EIS).

Additionally, Chapter 5 mainly discusses the electrochemical stability window of lithium argyrodite with chloride enriched, and also covers the slow cooling of heat-treated bromide enriched solid electrolyte for improved ionic conductivity and electrochemical stability. The results are compared between the commercial LPSC.

Chapter 6 of this thesis concludes with all the results and provides a coherent discussion of the work. Finally, in the conclusion section, all the research questions are answered as stated above.

# Processing of Halide rich Lithium argyrodite

#### 4.1. Introduction

In this chapter 4, we will discuss about the synthesis of lithium argyrodite composition of  $Li_6PS_5X$  and halide rich  $Li_{5.5}PS_{4.5}X_{1.5}$ , (X=Cl,Br) and treating the composition in various temperatures such as  $200^{\circ}$ C,  $350^{\circ}$ C,  $450^{\circ}$ C, and  $550^{\circ}$ C to understand the structural changes and ionic conduction behaviour using the characterization techniques like XRD, SEM, Raman spectroscopy, and temperature dependent EIS,.

# 4.2. Experimental methods

This section describes us about the experimental methods in synthesis and heat treatment. The section also traces the analyses of the structural information and behaviour of the lithium argyrodite as mentioned previously.

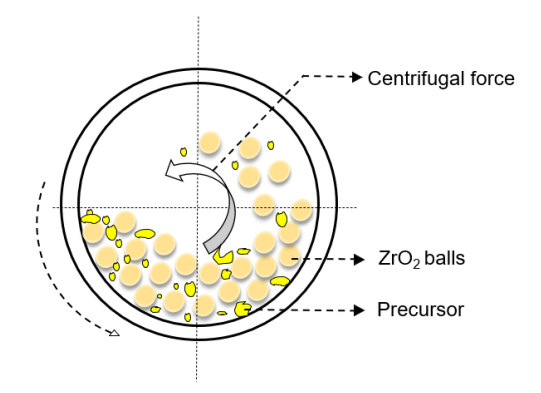
# 4.2.1. Mechanochemical synthesis of lithium argyrodite

The sample preparation was carried out in the argon filled atmosphere with <0.1ppm of moisture and oxygen content, since the lithium argyrodite are air sensitive. All the precursors were mixed based on the stoichiometric ratio of Lithium sulfide  $Li_2S$  (Sigma-Aldrich, 99.98%), phosphorus pentasulfide  $P_2S_5$  (Sigma-Aldrich, 99%), lithium chloride LiCl (Alfa Aesar, 99%),and lithium bromide LiBr (Sigma-Aldrich, 99.9%).

To prepare milling media and precursors, materials are typically measured and added to  $ZrO_2$  milling jars containing  $ZrO_2$  balls ( $\phi$  10 mm, total mass = 30 g) at 1:30 synthesis ratio. For 1 g of the needed product, we use 30 g of  $ZrO_2$  balls. The material is first uniformly homogenized with a mortar and pestle before being transferred to high-energy zirconium oxide ball mill jars (capacity = 45 mL).



(a) Ball mill jar containing the precursor before processing



(b) Schematic representation of high energy ball milling

Figure 4.1: High energy ball milling

The figure 4.1 shows a schematic perspective of high-energy ball milling, which includes the precursor and milling media. The high-speed rotation of jar increases the centrifugal force of the beads, causing them to strike the precursor with maximum energy ( $E_{max}$ ) and the impact creating desired product,[67]. The usual parameter for the ball milling apparatus (Fritsch-Pulverisette 7) is 550 rpm, 10 minutes of running period and 10 minutes of resting in order to reduce the heat generated inside the milling jars and repeated the above program for 60 cycles.

# 4.2.2. High temperature annealing

The heat treatment of a material that causes significant changes in structure. This method involves heating the material to the appropriate re-crystallization temperature (below the melting temperature), driving ions to migrate around defects, reducing dislocations, and converting amorphous ball-milled material to crystalline material,[68].



Figure 4.2: Ampule containing the SE pellets

The annealing process: The ball-milled material into pellets with a die set. The pellets are then inserted within a quartz tube (14 mm diameter) as shown in the above figure 4.2. The equipment is used to set up the vacuum (by using Pfeiffer Vacuum DCU) in the argon-filled quartz tube before sealing it. Finally, the sealed tube is heated to high temperatures such as  $200^{\circ}$ C,  $350^{\circ}$ C,  $450^{\circ}$ C, and  $550^{\circ}$ C in a muffle furnace for 2 hours. The same synthesis method has been used for all compositions.

# 4.2.3. X-Ray powder Diffraction

X-ray powder diffraction is used as a characterization tool that provides crystallographic information about a powder without causing any damage to the material, using X-rays as the source. According to Bragg's law, when X-rays with a wavelength ( $\lambda$ ) interact with a crystal, they are scattered by the atoms within the crystal planes. The inter-planar spacing (d) between these planes causes the X-rays to scatter at an angle of  $2\theta$  as shown in the below figure 4.3,[69].

The Bragg's law can be expressed as:

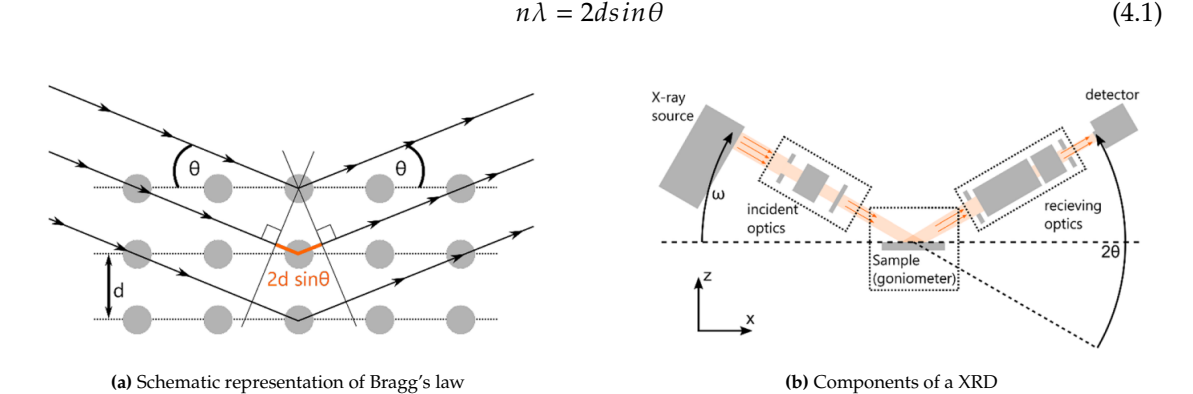


Figure 4.3: The schematic represents the X-ray diffraction principle and components,[69]

The sample was placed inside an air-tight holder with a Kapton cover on top to allow X-ray to penetrate and XRD was analysed using the X'Pert-Pro Diffractometer (PANalytical) with the source of Cu K $\alpha$  ( wavelength = 1.5406 Å) and operating at 45 kV and 40 mA. The XRD was measured from the diffraction angle (2 $\theta$ ) of 10° to 90° with the step-size of 0.0084.

#### Rietveld refinement of the X-ray diffraction pattern

The Rietveld refinement is an advanced pattern-fitting method developed by Dutch scientist Hugo Rietveld, originally formulated in 1967[70]. The diffraction data of the powder is obtained from the diffractometer and is fitted with the existing crystallographic information file by varying the height, width, and peak position to minimize the difference between the calculated and experimental data, thus determining accurate crystal lattice parameters. Rietveld refinement uses the least squares approach to resolve the differences between the calculated and measured powder diffraction patterns. It involves adjusting the lattice parameters, occupancy, and thermal parameters to achieve a match with the measured pattern. In this thesis work, TOPAS software has been used to fit the diffraction pattern and based on the weighted profile R-factor (Rwp) and the goodness of fit (GoF) between 1-1.2 is an ideal fit,[71]

# 4.2.4. Electrochemical Impedance spectroscopy

Electrochemical impedance spectroscopy (EIS) is an analytical tool used to study the electrochemical properties of the composition and the system which uses a wide range of frequencies to understand the behaviour of the material. EIS is also a non-destructive testing method that doesn't cause any damage to the material. In EIS, the small varying sinusoidal potential E(t) is applied over the system and as a function, the current density j(t) provides the varying frequency as output as shown in the below figure 4.4. The ratio of the AC potential by the current density gives the impedance Z(t) of the system as described in the equation 4.2,[72]

$$Z(t) = \frac{E(t)}{j(t)} \tag{4.2}$$

The input can be mathematically expressed as:

$$E(t) = |\Delta E| \sin(\omega t) \tag{4.3}$$

where,

- E(t) = Input voltage potential
- $|\Delta E|$  = peak voltage amplititude
- $\omega$  = angular frequency
- t = time

By Changing the frequency from higher frequency to lower frequency results in various phenomena behind the system. During the high frequency, the ions tend to migrate while in the lower frequency noticeably the diffusion mechanism occurs. since the impedance is a complex number there are known to be real and imaginary impedance, which are denoted as Re(z) and Im(Z), respectively,[72].

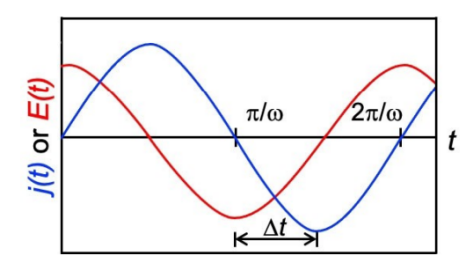


**Figure 4.4:** Plot of the AC potential E(t) as input and the current density j(t) as output, resulting in the impedance Z(t) of the system,[72]

The required data and the material information are acquired from the Nyquist and Bode plot as shown in the above figure 4.5. The Nyquist plot is plotted between the real impedance and the imaginary impedance which also expressed as the equation 4.4,[72].

$$|Z(\omega)| = \sqrt{Re(Z(\omega))^2 + Im(Z(\omega))^2}$$
(4.4)

where,  $\phi$  is the function of the  $\omega$ :

$$\phi(\omega) = tan^{-1} \frac{ReZ(\omega)}{Im(Z(\omega))}$$
(4.5)

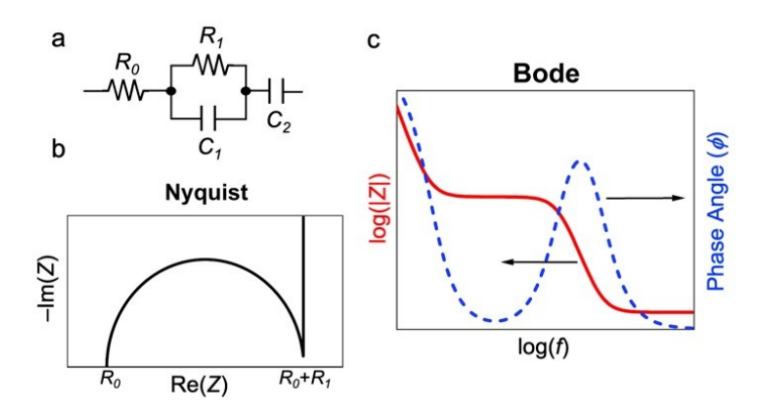


Figure 4.5: (a) Equivalent circuit of the solid electrolyte, (b) Schematic Nyquist plot of the electrolyte, and (c) Bode plot, [72].

The experimental data from the EIS is fitted with an equivalent circuit, as shown in Figure 4.5 (a), which provides the required information. The equivalent circuit fitting for the electrochemical system includes the initial resistance between the electrode and the solid electrolyte, denoted as  $R_0$ . The semicircle with respect to time represents the conduction process and the charge transfer resistance. As discussed previously, the low-frequency domain is dominated by diffusion phenomena. To determine the resistance, it is taken from the Nyquist plot at  $R_0 + R_1$ .

$$\sigma_{ion} = \frac{l}{R_{Total}A} \tag{4.6}$$

where,

- $\sigma_{ion}$  = Ionic conductivity (mS/cm)
- l = Thickness of the sample (cm)
- $R_{Total}$  = Total resistance of the sample ( $\Omega$ )
- $A = Area (cm^2)$

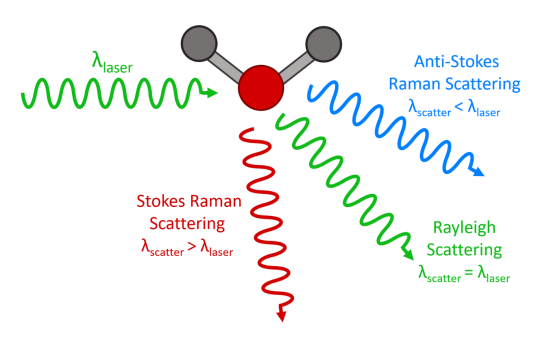
Among the Nyquist plot and Bode plot, the most generally used plot is the Nyquist plot in the field of solid-state batteries to determine the resistance ( $R_{\text{Total}}$ ) and by using the equation 4.6, we get to calculate the ionic conductivity of the solid electrolyte. The Bode plot, on the other hand, provides the frequency response of the impedance magnitude and the phase angle ( $\phi$ ) change.

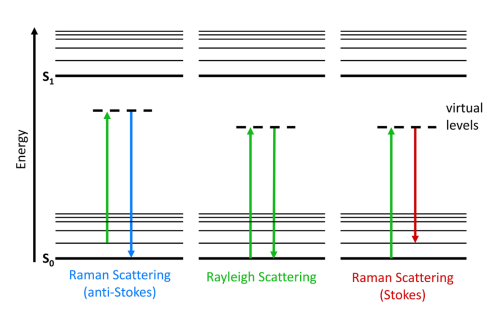
In this thesis work, all measurements were carried out using the Biologic SP-300, with a measuring frequency range from 7 MHz to 100 mHz. The SE, as shown in Figure 2.3, is filled with 200 mg of solid electrolyte and closed under a pressure of 392 MPa to improve interaction between the solid electrolyte and the electrodes, thus enhancing ion migration and reducing voids. For temperature-based impedance measurements, the SSB is placed inside a FRYKA Cold Box (B 35-85 //LOGG) climate chamber and impedance is measured at varying temperatures from  $0^{\circ}$ C to  $-50^{\circ}$ C in steps of  $10^{\circ}$ C to determine the activation energy of the composition. The experimental spectra obtained are later analyzed using RelaxIS 3 to fit the appropriate equivalent circuit.

# 4.2.5. Raman spectroscopy

Raman spectroscopy is a optical spectroscopy technique is based on the inelastic scattering of the light and it's first experimental observation by the Indian physicists C.V. Raman and K.S. Krishnan,[73] in 1928. Raman spectroscopy is used to determine the chemical and structural properties of the material through raman scattering.

In other terms raman scattering can be categorised in three types such as rayleigh, strokes, and anti-strokes scattering. when an electrons tend to excite to the virtual energy level for some period and backs to the ground state with the same wavelength is known to be Rayleigh's scattering,[74]. But when the LASER wavelength ( $\lambda_{laser}$ ) is lower than the wavelength of the scattered wavelength ( $\lambda_{scatter}$ ) is known as Strokes raman scattering and similarly when the LASER wavelength is higher is known to be anti-scattering wavelength as shown in the figure 4.6 (a) and the (b) shows the differences in the energy level and the virtual level.





- (a) Schematic representation of the difference in the strokes, anti-strokes, and Rayleigh raman scattering
- (b) Raman scattering showing the different energy levels

Figure 4.6: Schematic representation of the Raman scattering,[74]

# 4.3. Results and discussion

In this segment, we will go over the outcomes and results of the previously mentioned characterization of the samples to determine their behavior and properties for future research. This involves an examination of XRD patterns, SEM images, Raman spectra, ionic conductivity, and activation energy.

# 4.3.1. XRD Results and lattice parameters

The samples were synthesized as described in Section 4.2.1 and then heat-treated to attain an stable crystalline composition. Each figure shows the XRD patterns of both ball-milled and heat-treated samples, with considerable change in the peak intensity. The comparison of ball-milled (BM) and heat-treated at 550°C samples shows that high-energy ball milling (black) successfully converts the precursor to the base composition of lithium argyrodite with the partial crystalline glass-ceramic electrolyte,[75]. With increasing the heat treatment temperature for reaction up to 550°C (green), the peaks become sharper and less widening showing increased crystallinity as shown in the figure 4.7. However, we observed less than 2 wt% impurities on heat treatment samples at 200 °C. The remaining samples did not observe the impurities phase.

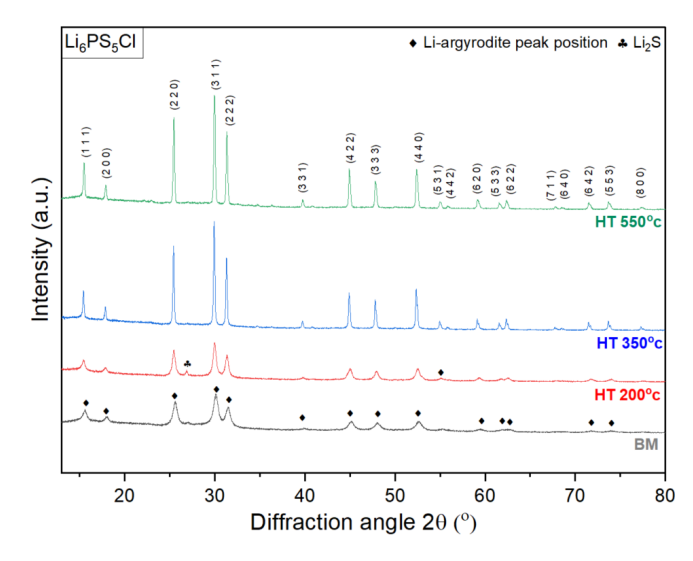


Figure 4.7: XRD patterns of  $Li_6PS_5Cl$  under various conditions, including ball milling (BM) and heat treatments (HT) at 200°C, 350°C, and 550°C with rhombus symbol over the peaks representing the lithium argyrodite peak position

Consecutively, figure 4.7 shows us the significant changes in the peak shape and peak position, later we did refinement to calculate the lattice parameter and site-disorder from ball milled sample to high-temperature annealing composition of  $Li_6PS_5Cl$ . The Rietveld refinement of the XRD pattern shows the F43m (cubic) space group,[76]. In this Thesis, we used the TOPAS Academic V4 software to refine XRD and neutron patterns for all the compositions shown in the Appendix A.1.

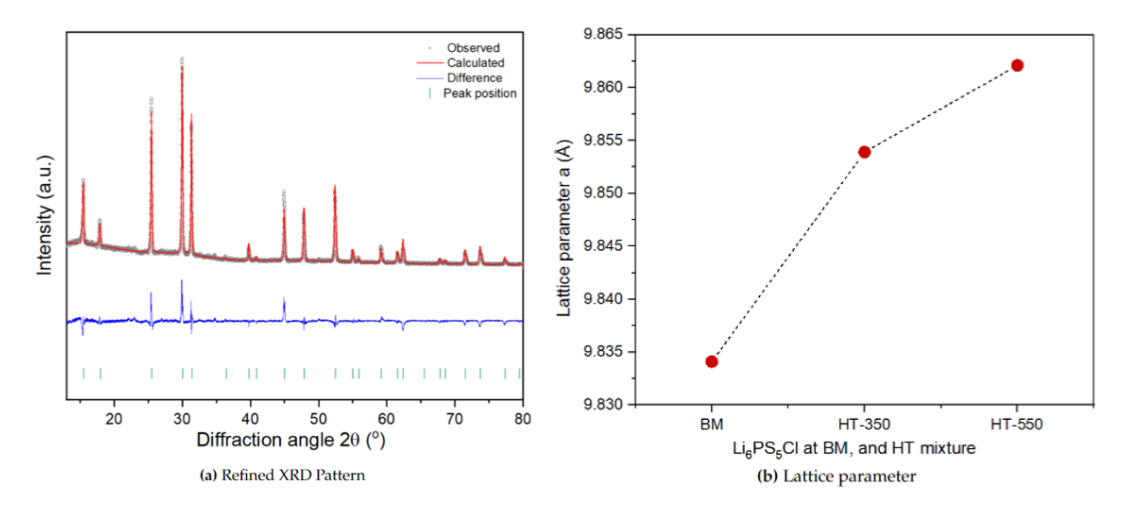


Figure 4.8: Refined XRD pattern and the lattice parameter of BM and annealing at 350°C and 550 °C Li<sub>6</sub>PS<sub>5</sub>Cl composition

The figure 4.8 (a) represents the refined XRD pattern of the  $Li_6PS_5Cl$  HT at 550°C and shows the obtained, calculated, and difference pattern with indexing the lithium argyrodite phase. The figure

4.8 (b) and table 4.1 shows the lattice parameters, volume, and interaxial angle of the crystal lattice. The table demonstrates that an increase in lattice parameters correlates with an increase in unit cell **volume from 953.45** ų **for BM to 959.21** ų **for HT** 550°C, and provides wider space for higher Li-ion mobility. As annealing temperature increases could reduce internal stresses and reduce defects like dislocations and vacancies. This defect reduction can allow the lattice to relax and expand slightly, particularly at higher annealing temperatures with maintaining the cubic structure.

	Lattice parameters (Å)			Volume (ų)	interaxial angle ( $\alpha = \beta = \gamma$ )	
	a	b	С	volume (A)	interaction arighe $(\alpha - \beta - \gamma)$	
BM	9.842	9.842	9.842	953.45	900	
HT 350	9.853	9.853	9.853	956.827	90°	
HT 450	9.862	9.862	9.862	959.218	90°	

Table 4.1: Lattice Parameters, Volumes, and Interaxial Angles of Li<sub>6</sub>PS<sub>5</sub>Cl at BM and various HT compositions

Similarly, in  $Li_6PS_5Br$ , exhibits the same characteristics of the cubic symmetry of F-43m space group. The XRD patterns indicate that high-energy ball milling contributes to the formation of the lithium argyrodite phase. The comparison between the BM and HT mixtures shows the increase in peak intensity and no attribution to the peak shift in the  $2\theta$  value, indicating that high-temperature annealing reveals the crystalline argyrodite cubic structure. The figure 4.9 (a) shows us the pure argyrodite XRD pattern with some minor impurities of LiBr in the crystal structure. All the argyrodites were heated only until their stable phase, with Cl and Br annealed at a maximum of  $550^{\circ}$ C, to avoid material decomposition and phase segregation.[77]. The figure 4.9 (b) shows the lattice parameter with annealing temperature for  $Li_6PS_5$ Br. We observed a similar behavior compared to  $Li_6PS_5$ Cl as studied. Increasing the annealing temperature can reduce internal stresses and defects, allowing the lattice to relax and expand slightly. The lattice parameter then remains constant once the relaxed structure is achieved.

The figure 4.9 (b) and table 4.2 show the changes in the lattice parameter in the same argyrodite crystal structure. High-temperature annealing causes an expansion of the unit cell compared to the BM mixture and an increase in the volume of the unit cell contributes to better ion diffusion.

	Lattice parameters (Å)			Volume (Å <sup>3</sup> )	interaxial angle ( $\alpha = \beta = \gamma$ )	
	a	b	С	voiune (A)	interaxial angle $(\alpha - \beta - \gamma)$	
BM	9.9458	9.9458	9.9458	983.855	90°	
HT 350	9.9914	9.9914	9.9914	997.425	90°	
HT 550	9.9906	9.9906	9.9906	997.187	90°	

**Table 4.2:** Lattice Parameters, Volumes, and Interaxial Angles of  $Li_6PS_5Br$  at BM and various HT compositions

In halide-enriched composition at  $550^{\circ}$ C temperature showing more impurities of LiX (X = Cl, Br) due to decomposition of the lithium argyrodite phase, in our study we have reduced the maximum temperature to  $450^{\circ}$ C for halide-enriched lithium argyrodite. The figure 4.10 shows the

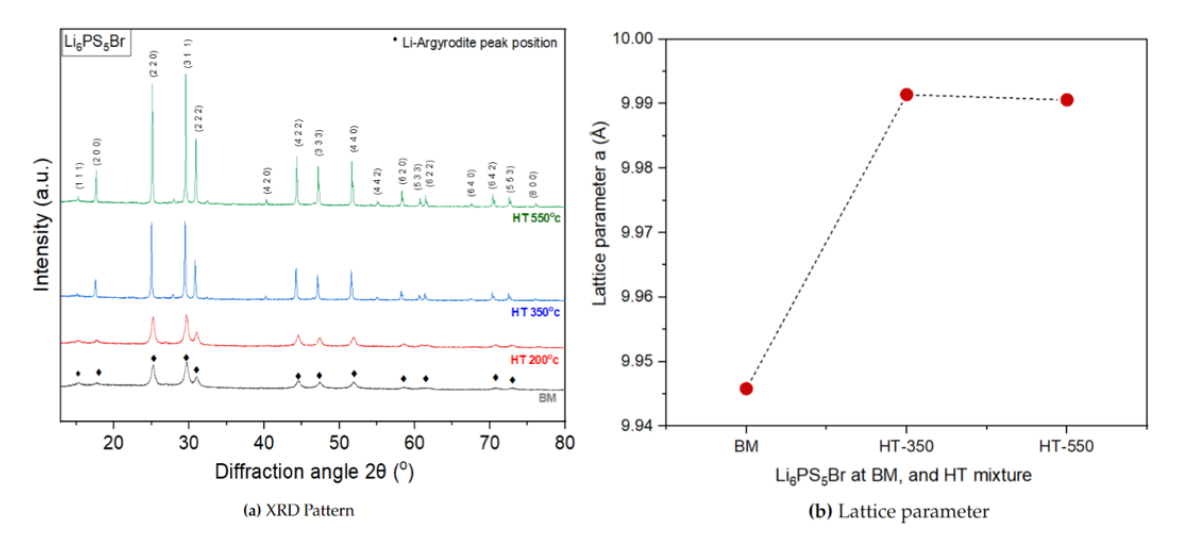


Figure 4.9: XRD patterns and the lattice parameter of  $Li_6PS_5$ Br under various conditions, including BM and HT at 350°C, and 550°C with the rhombus symbol over the peaks representing the peak position of lithium argyrodite

XRD patterns of  $Li_{5.5}PS_{4.5}Cl_{1.5}$  mixture of BM and the HT (200°C, 350°C, 450°C). The BM XRD indicates that the mixture is more amorphous or nano-crystalline, but the mixture becomes more crystalline when heated in high-temperature annealing.

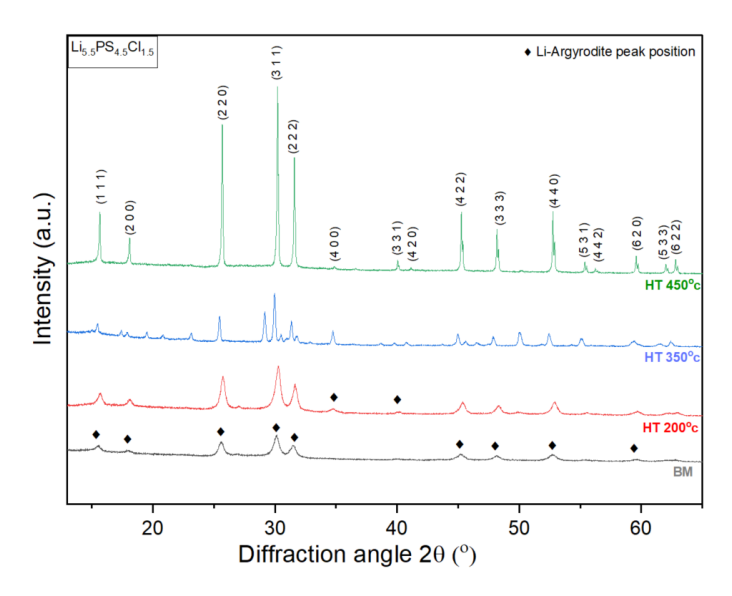
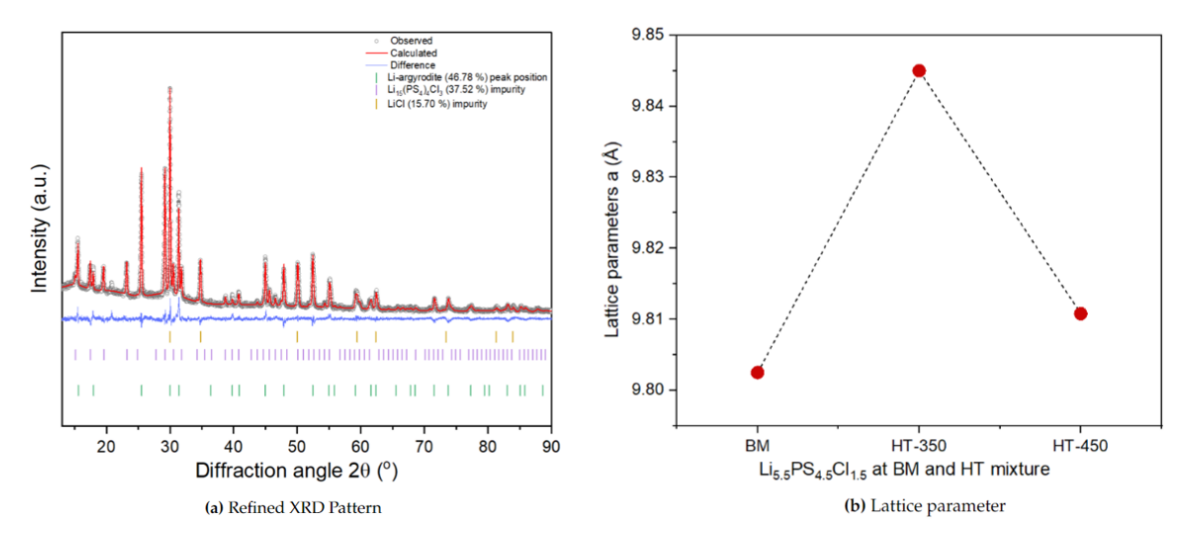


Figure 4.10: XRD patterns of  $Li_{5.5}PS_{4.5}Cl_{1.5}$  under various conditions, including BM and HT at 200°C, 350°C, and 550°C with the rhombus symbol over the peaks representing the peak position of lithium argyrodite

Notably, the HT 350°C sample had significantly more peaks compared to any other sample

tested. This suggests a structural transformation at that particular temperature, and the Reitveld refinement of  $Li_{5.5}PS_{4.5}Cl_{1.5}$  HT 350°C in figure 4.10 (a) shows the impurities of  $Li_{15}(PS_4)_4Cl_3$  and LiCl of 37.52 % and 15.70 %, respectively present in the structure which contributes to higher lattice parameter compared to other samples as shown in the figure 4.11(b), resulting in the expansion of the unit cell but due to the presence of impurities occupying in the unit cell makes the Li-ion diffusion harder and limited, [78].



**Figure 4.11:** (a) Reitveld refinement of the XRD pattern of  $Li_{5.5}PS_{4.5}Cl_{1.5}$  (HT  $350^{o}$ ) using TOPAS Academia V4 showing the presence of  $Li_{15}(PS_4)_4Cl_3$  and LiCl impurity in the mixture and (b) Lattice Parameters of  $Li_{5.5}PS_{4.5}Cl_{1.5}$  at BM and various HT mixture

This table 4.3 offers an overview of the lattice parameters, volume expansion, and interaxial angles of heat-treated materials. Furthermore, it helps us understand how impurities alter the lattice properties and expand the unit cell. However, the interaxial angle remains constant as these compositions have the same cubic structure ( $\alpha = \beta = \gamma = 90^{\circ}$ ).

	Lattice parameters (Å)			Volume (ų)	interaxial angle ( $\alpha = \beta = \gamma$ )
	a	b	c volume (A		$\frac{1}{2} \frac{1}{2} \frac{1}$
BM	9.8025	9.8025	9.8025	941.928	90°
HT 350	9.845	9.845	9.845	960.044	90°
HT 450	9.8108	9.8108	9.8108	944.319	90°

**Table 4.3:** Lattice Parameters, Volumes, and Interaxial Angles of  $Li_{5.5}PS_{4.5}Cl_{1.5}$  at BM and various HT compositions

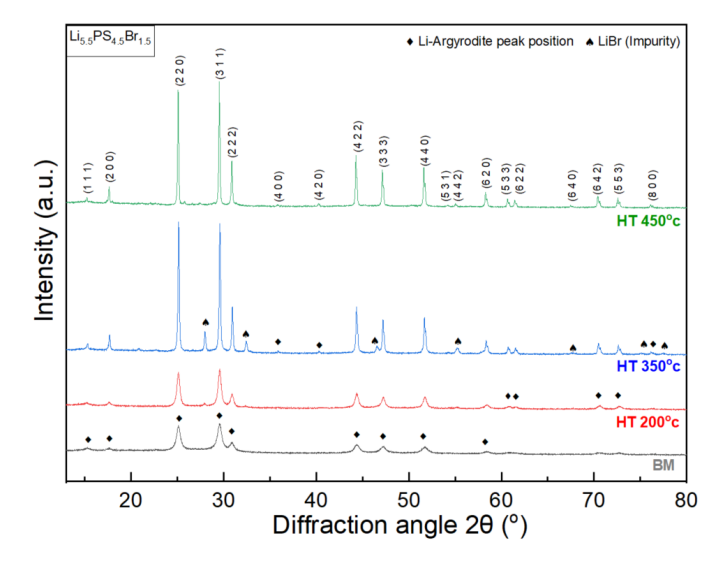
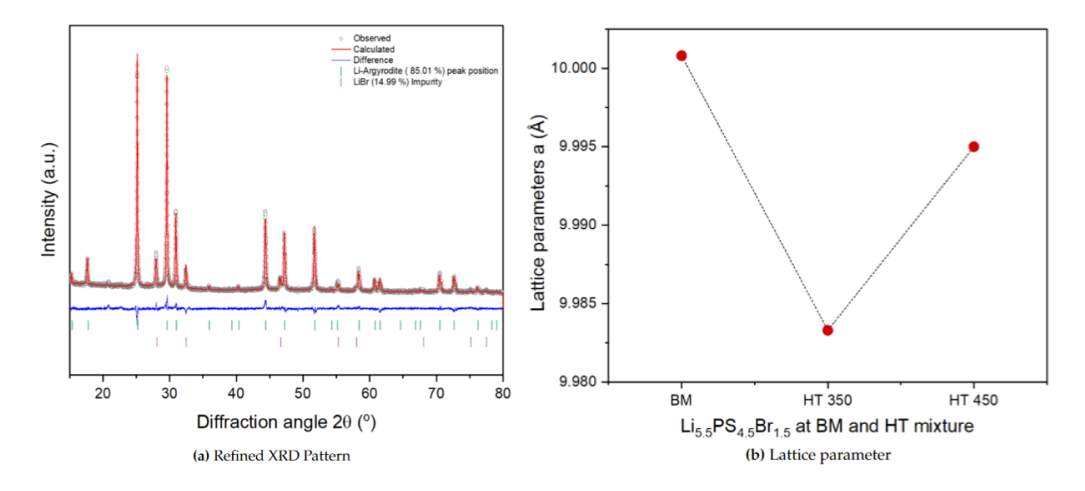


Figure 4.12: XRD patterns of  $Li_{5.5}PS_{4.5}Br_{1.5}$  under various conditions, including BM and HT at 200°C, 350°C, and 450°C with the rhombus symbol over the peaks representing the peak position of lithium argyrodite

The figure 4.12 describes the XRD patterns of  $Li_{5.5}PS_{4.5}Br_{1.5}$  under BM and various heat treated mixtures. In figure 4.12, the BM XRD (black) pattern shows the amorphous solid structure of lithium argyrodite, which improves with heat treatment at high temperatures such as 350°C and 450°C. The peaks with rhombus symbol represents the Li-argyrodite peak positions in the XRD pattern, and the miller indices represents the plane position in the crystal lattice. Heat treatment at 450°C, as compared to the BM shows the crystallization of the composition, making it more coherent and revealing the  $F\bar{4}3m$  crystal structure.



**Figure 4.13:** (a) Refined XRD pattern of HT  $350^{\circ}$ C and the lattice parameter of BM and HT of  $Li_{5.5}PS_{4.5}Br_{1.5}$ , in which the refinement was done using TOPAS Academic V4 and (b) Lattice Parameters of  $Li_{5.5}PS_{4.5}Br_{1.5}$  at BM and various HT mixture

However, similarly in figure 4.12 the XRD pattern in HT  $350^{\circ}$ C has more peaks when compared all other XRD pattern of the  $Li_{5.5}PS_{4.5}Br_{1.5}$  which shows the presence of impurities which was later confirmed with the Rietveld refinement, and found the LiBr impurities as shown in the figure 4.13 (a).

Unlike the other sample such as  $Li_6PS_5Cl$ ,  $Li_{5.5}PS_{4.5}Cl_{1.5}$ , and  $Li_6PS_5Br$  the  $Li_{5.5}PS_{4.5}Br_{1.5}$  shows a different trend as we see in the figures 4.13 (b) and table 4.4 which indicated the decrease in the lattice parameter at 350° C then increase again at 450°C annealing temperature, maybe due change the bromide occupancies on 4d and 4a site, next section (4.3.4) we will talk about the site-disorder and give proper explanation for lattice parameter correlations.

	Lattice parameters (Å)			Volume (ų)	interaxial angle ( $\alpha = \beta = \gamma$ )
a		b	С	voiune (A)	$\left  \frac{\text{Interaxial arigic } (\alpha - \beta - \gamma)}{\alpha - \beta} \right $
BM	10.0008	10.0008	10.0008	1000.260	$90^{o}$
HT 350	9.9833	9.9833	9.9833	995.025	90°
HT 450	9.995	9.995	9.995	998.507	90°

**Table 4.4:** Lattice Parameters, Volumes, and Interaxial Angles of  $Li_{5.5}PS_{4.5}Br_{1.5}$  at BM and various HT compositions

The table 4.5 represents the site disorder of halide occupancies in the 4d and 4a sites. The data was obtained from the neutron powder diffraction. Reitveld refinement was shows the occupancy of halide  $(X^-)$  in Wyckoff 4d and 4a sites in the cubic structure.

# 4.3.2. Site-disorder in lithium argyrodites

The site disorder percentage varies based on the halide (X = Cl, Br, and I) in the lithium argyrodite structure due to differences in ionic radii (Cl = 181 pm, Br = 196 pm, and I = 220 pm).  $Cl^-$  and  $Br^-$  based lithium argyrodites exhibit site disorder due to their similar ionic radii to that of the sulfur anion ( $S^{2-}$  = 184 pm). In contrast, iodine  $I^-$  based argyrodite shows no site disorder due to the significant ionic radii mismatch, resulting in ionic conductivity below 0.001 mS  $cm^{-1}$ . Therefore, we did not include iodine-based argyrodite compositions in this work. Instead, we focused on  $Cl^-$  and  $Br^-$  based argyrodites and studied how site disorder or halide occupancies on 4d site is affected by synthesis conditions, ranging from ball milling (BM) to heat treatment at 350°C, 450°C, and 550°C.

We determined the site disorder, specifically the halide occupancy on the 4d site, through Rietveld refinement analysis using neutron diffraction performed at different stages: after BM, and after heat treatment at 350°C and 550°C, followed by natural cooling and room temperature measurement. We were unable to refine the  $Li_6PS_5$ Cl BM samples due to a low data-to-background ratio. After annealing the samples in a vanadium container, we found a 66% site disorder at 350°C (from neutron diffraction measurements), and after heat treatment, it slightly decreased to around 65%, indicating improved crystallinity but minimal change in site disorder. A similar correlation was found in the  $Li_{5.5}PS_{4.5}Cl_{1.5}$  composition. With higher chloride content, more chloride occupied the 4a and 4d sites, but this was not influenced by changing the annealing temperature.

We were unable to perform measurements on the  $Li_{5.5}PS_{4.5}Br_{1.5}$  composition due to the unavailability of the PEARL instrument, but previous data at the same temperature showed a site disorder

of around 64%,[62].

Composition	Site-disorder/halide occupancy on 4d site (%)	Halide on 4a site (%)	Lattice parameter (Å)
Li <sub>6</sub> PS <sub>5</sub> Cl BM	-	-	-
Li <sub>6</sub> PS <sub>5</sub> Cl 350°C	66	34	9.9853
Li <sub>6</sub> PS <sub>5</sub> Cl 550°C	58	42	10.0545
Li <sub>6</sub> PS <sub>5</sub> Cl 550°C RT	65	35	9.8711
Li <sub>6</sub> PS <sub>5</sub> Br BM	32	68	9.9849
<i>Li</i> <sub>6</sub> <i>PS</i> <sub>5</sub> Br 350°C	28	72	10.0751
<i>Li</i> <sub>6</sub> <i>PS</i> <sub>5</sub> Br 550°C	51	49	10.1279
Li <sub>6</sub> PS <sub>5</sub> Br 550°C RT	35	65	9.9913
Li <sub>5.5</sub> PS <sub>4.5</sub> Cl <sub>1.5</sub> BM	70	80	9.8287
<i>Li</i> <sub>5.5</sub> <i>PS</i> <sub>4.5</sub> <i>Cl</i> <sub>1.5</sub> 450°C	64	86	9.9850
Li <sub>5.5</sub> PS <sub>4.5</sub> Cl <sub>1.5</sub> 450°C RT	67	83	9.8312
Li <sub>5.5</sub> PS <sub>4.5</sub> Br <sub>1.5</sub> 450°C RT,[62]	64	87	9.9742

**Table 4.5:** Table showing the site disorder of halide occupancies in 4d and 4a sites, and lattice parameter of lithium argyrodite.

# 4.3.3. SEM morphology

In this study, the SEM was conducted to study the morphology of the lithium argyrodite shows the comparison between the ball milled and heat treated sample. The SEM image shows the morphology which explains the grain size, boundaries, and the shape which helps to improve battery performance in the interaction between the electrode materials.

In figure 4.14, (a) and (b) shows us the SEM image of the  $Li_6PS_5Cl$  of BM and HT (550°C) where the BM sample was shapeless, more grainy, and unevenly distributed micro-agglomerated grains over the large particles. Each BM particles are about an average of 10-15  $\mu$ m in size even though they are not in definite shape. However, the HT (550°C) sample should the similar morphology of the BM but significant reduction of the micro-agglomerate over the surface of large particle.

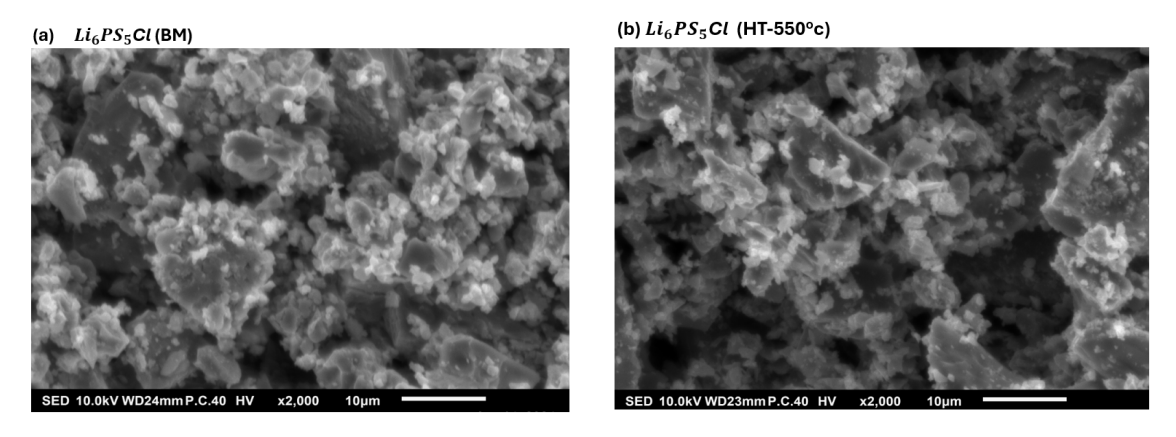


**Figure 4.14:** SEM images of  $Li_6PS_5Cl$  (a) BM, and (b) HT  $450^{o}c$  solid electrolyte was prepared by high energy ball milling and high temperature annealing

The figure 4.15 (c) and(d), describes the SEM image of the  $Li_6PS_5$ Br of BM and HT (550°C). Similar to the  $Li_6PS_5$ Cl, this is also in irregular shape and doesn't follow any pattern of size or shape to describe definitely. The micro-agglomerates over the HT (550°C) sample has reduced in lower ratio but are densely packed and an average size of  $10\mu m_s$ [79].

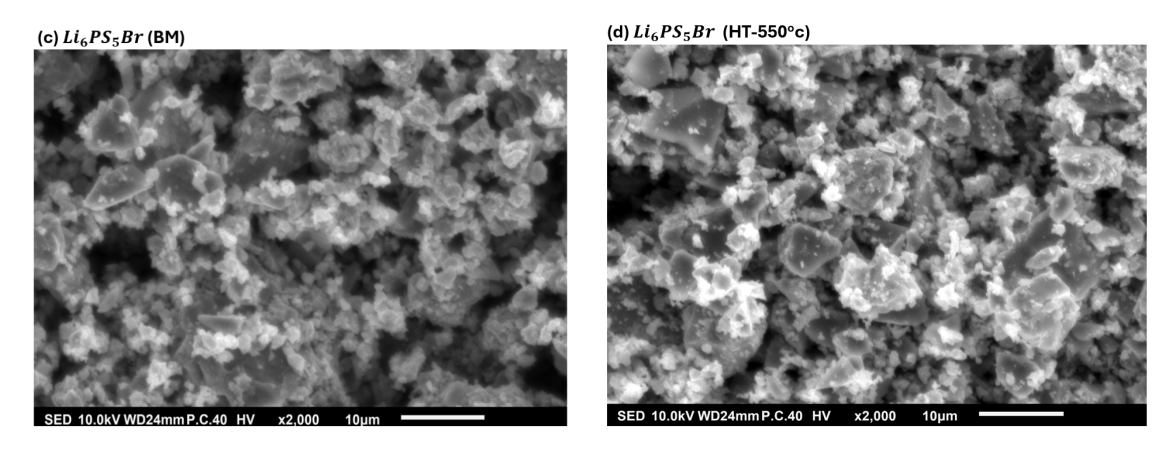


**Figure 4.15:** SEM images of  $Li_6PS_5$ Br (a) BM, and (b) HT  $450^{o}$ c solid electrolyte was prepared by high energy ball milling and high temperature annealing

Relatively, while compared to the  $Li_6PS_5Cl$  and  $Li_6PS_5Br$  the external shape and texture looks similar. Figure 4.17 and shows that the particles of the BM sample of  $Li_{5.5}PS_{4.5}Cl_{1.5}$  and  $Li_{5.5}PS_{4.5}Br_{1.5}$  are smaller particle size and include micro-agglomerates sticking to the surface of bigger particles, which are more amorphous in nature. Heat treatment of the sample at  $450^{\circ}C$  had no significant influence on the micro-grain distribution throughout the particles.

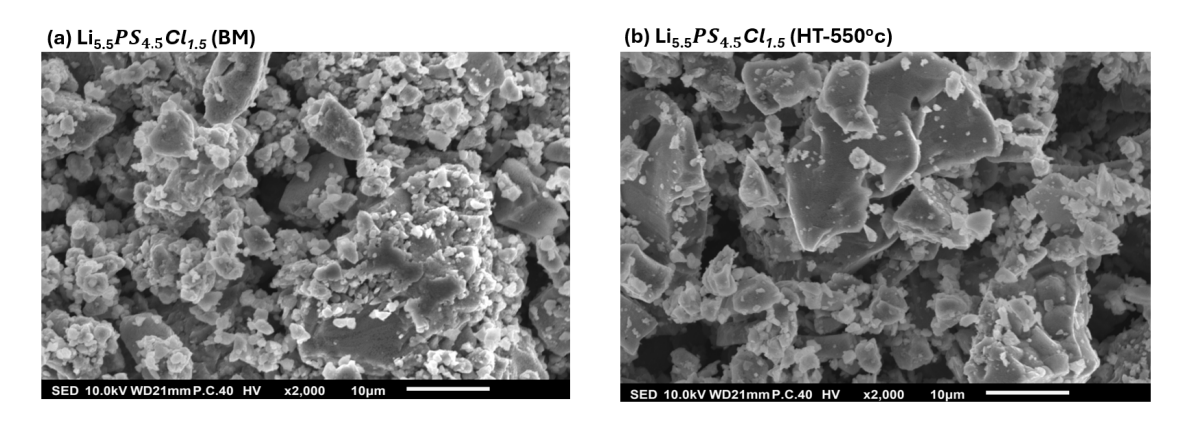


**Figure 4.16:** SEM images of  $Li_{5.5}PS_{4.5}Cl_{1.5}$  (a) BM, and (b) HT 450°c solid electrolyte was prepared by high energy ball milling and high temperature annealing

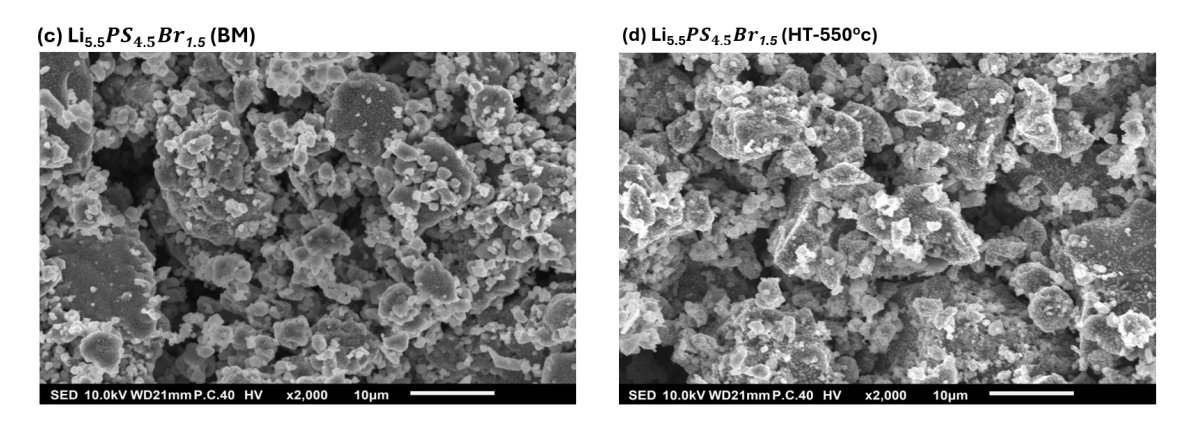


**Figure 4.17:** SEM images of  $Li_{5.5}PS_{4.5}Br_{1.5}$  (a) BM, and (b) HT  $450^{\circ}$ c solid electrolyte was prepared by high energy ball milling and high temperature annealing

# 4.3.4. Raman spectroscopy

Raman spectroscopy is taken to study the vibrational modes of the lithium argyrodite of both chloride and bromide substituted which exhibits the presence of phosphorous-sulfur bonds in the BM and HT samples. The phosphorous-sulfur bond is exhibited in the high wavelength region and it is visible around the wavelength between  $400\text{-}500~cm^{-1}$ . In this thesis work, the samples were prepared in the transparent slides by making use of the vacuum gel to seal the sample between the slide and the cover slip. Prepared slides where then characterized using the HORIBA LabRAM HR and with 10% LASER grading.

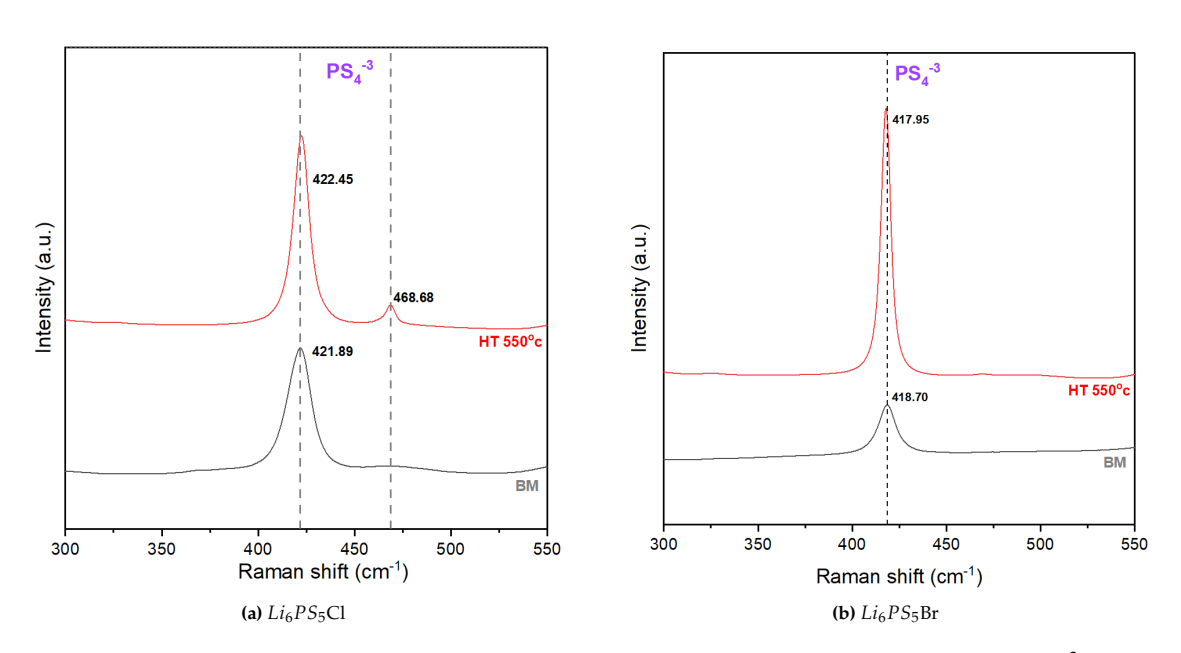


**Figure 4.18:** Raman spectra of BM and HT samples of  $Li_6PS_5$ Cl and  $Li_6PS_5$ Br showing the peak and  $PS_4^{-3}$ 

There has been slight difference in the peak position of both BM and HT of all the samples measured and the figure 4.18 (a) shows the Raman spectra of both BM and HT  $550^{\circ}$ C, indicating the presence of the PS<sub>4</sub><sup>3-</sup> in the composition. The stronger peak shift was observed from 421.89 to 422.45  $cm^{-1}$  of BM to HT  $550^{\circ}$ C, respectively, and the weaker peaks at  $468.6 cm^{-1}$ . This indicates the presence of PS<sub>4</sub><sup>3-</sup> tetrahedral volume in  $Li_6PS_5$ Cl after the high temperature annealing the intensities of the PS<sub>4</sub><sup>3-</sup> peak get sharper and it shows more crystalline materials in accordance to the previously seen XRD data above,[80]. Similarly, in  $Li_6PS_5$ Br also exhibits the stronger peaks of PS<sub>4</sub><sup>3-</sup> at 418.90  $cm^{-1}$  and 417.95  $cm^{-1}$  of the BM and HT  $550^{\circ}$ C, respectively as shown in the figure 4.18 (b).

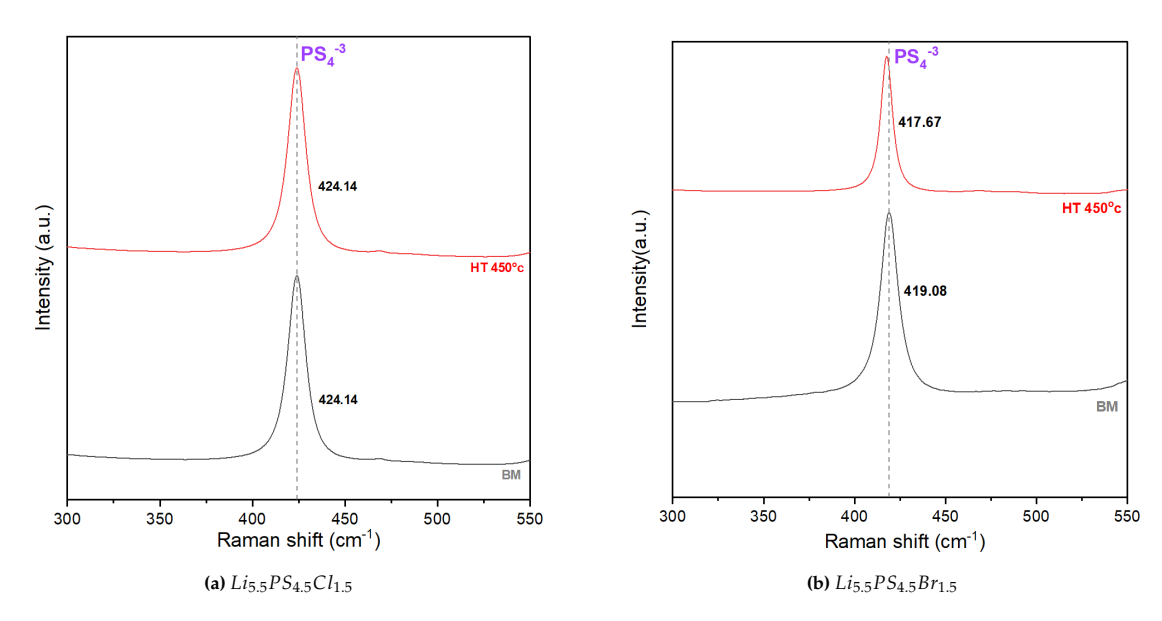


**Figure 4.19:** Raman spectra of BM and HT samples of  $Li_{5.5}PS_{4.5}Cl_{1.5}$  and  $Li_{5.5}PS_{4.5}Br_{1.5}$  showing the peak and PS<sub>3</sub><sup>3</sup>

In figure 4.19 (a) and (b), the Raman spectra of  $Li_{5.5}PS_{4.5}Cl_{1.5}$  and  $Li_{5.5}PS_{4.5}Br_{1.5}$  shows both the BM and HT 450°C samples. The  $Li_{5.5}PS_{4.5}Cl_{1.5}$  has the same peak position and intensity at 424.14  $cm^{-1}$  whereas the  $Li_{5.5}PS_{4.5}Br_{1.5}$  has the peak shift from 419.08  $cm^{-1}$  to 417.67  $cm^{-1}$  representing the existence of PS<sub>4</sub><sup>3</sup> has the high ionic conductivity phase in the composition.[81].

The BM exhibited the presence of the polyhedral  $PS_4^{3-}$  in the cubic lattice. The presence of  $PS_4^{3-}$  in both BM and HT samples shows the that lithium argyrodite phase formed after the ball milled the materials and only heat treatment at higher temperature improved the crystalline of all compositions.[81].

# 4.3.5. The Ionic conductivity of Lithium Argyrodites series

In the previous sections, we have seen the structure and morphological observation explain the peak positions of the both BM and HT samples and their differences in the morphology using the SEM. Here, in this section, we will be discussing about the the ionic conductivity (IC) of both BM and HT samples for the following compositions which are  $Li_6PS_5Cl$ ,  $Li_6PS_5Br$ ,  $Li_{5.5}PS_{4.5}Cl_{1.5}$ , and  $Li_{5.5}PS_{4.5}Br_{1.5}$ . All the results were recorded using the BioLogic SP-200 impedance analyzer with the ranging frequencies from 7 MHz to 100 mHz with 10 mV amplitude. The sample was measured

200 mg and placed in the SSB and a closing pressure of 392 MPa for better interaction of particle and an average of  $\sim$  2 mm thickness of the pellet over the area of electrode around 10 mm diameter. The observed spectra was later fitted into equivalent circuit using the RelaxIS 3 by fitting an appropriate circuit model.

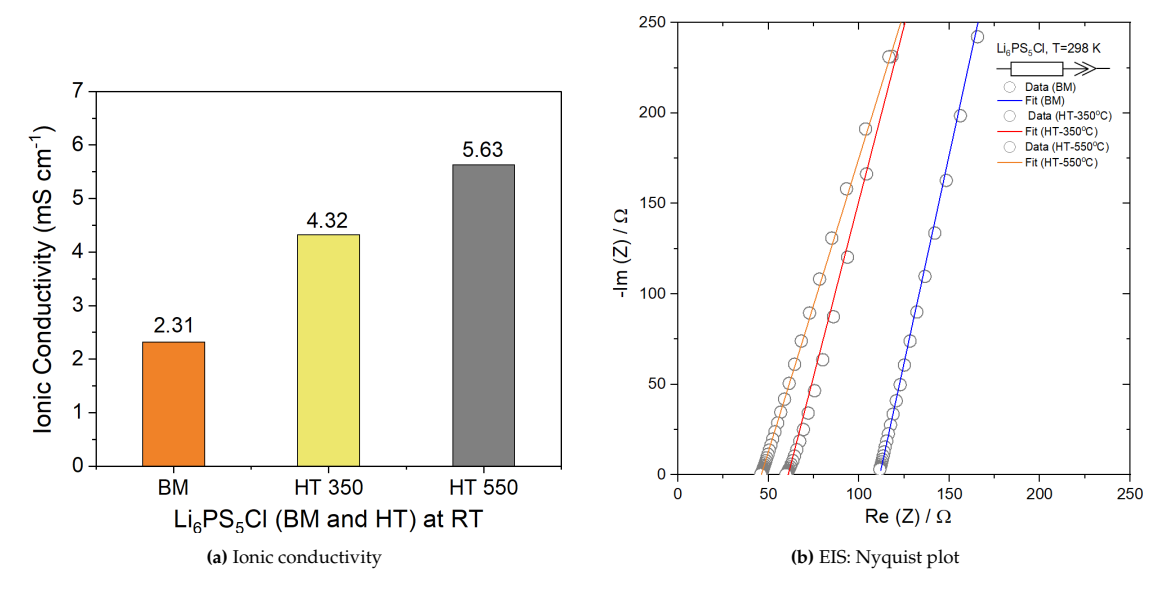


Figure 4.20: Ionic conductivity and EIS fit with equivalent circuit of  $Li_6PS_5Cl$  at room temperature

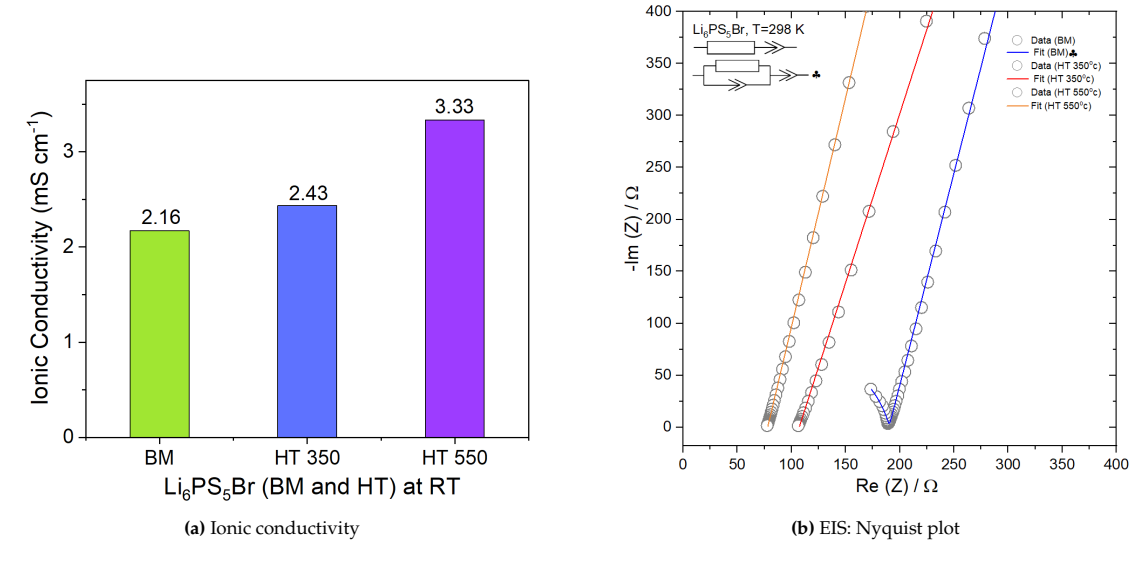


Figure 4.21: Ionic conductivity and EIS fit with equivalent circuit of  $Li_6PS_5$ Br at room temperature

In figure 4.20 and Figure 4.21 shows the ionic conductivity and Nyquist plot of both  $Li_6PS_5Cl$  and  $Li_6PS_5Br$  for BM and HT samples at room temperature (298 K). Both figures demonstrate an increase in ionic conductivity as the heat treatment temperature increases from BM to 550°C. This increase may be due to a more crystalline structure and larger lattice parameters, which could facilitate easier ion transport.

For  $Li_6PS_5Cl$ , the BM composition exhibits an ionic conductivity of 2.31 mS  $cm^{-1}$ , which increases to 5.63 mS  $cm^{-1}$  after heat treatment. Similarly, for  $Li_6PS_5Br$ , the BM composition shows an ionic conductivity of 2.16 mS  $cm^{-1}$ , increasing to 3.33 mS  $cm^{-1}$  after heat treatment. While the BM samples of  $Li_6PS_5Cl$  and  $Li_6PS_5Br$  have similar ionic conductivities, the higher-temperature synthesis of  $Li_6PS_5Cl$  results in greater ionic conductivity compared to  $Li_6PS_5Br$ . This difference is attributed to the higher disorder found in  $Li_6PS_5Cl$  (around 65%) compared to  $Li_6PS_5Br$  (around 35%). As previous studies have shown, higher disorder enhances inter-cage jumps, facilitating long-range lithium movement and thereby increasing ionic conductivity. The Nyquist plot and the equivalent circuit with a resistor ( $R_e$ ) and a constant phase element (CPE) used to fit the spectra as shown in the figure 4.20 (b),[82].

Our focus in this work is to understand the BM and heat treatment temperature which influences the lattice parameter, site-disorder, crystallinity, and higher ionic conductivity. For the chloride and bromide rich lithium argyrodite samples exhibits excellent ionic conductivity while compared to the previous samples of  $Li_6PS_5Cl$  and  $Li_6PS_5Br$ .

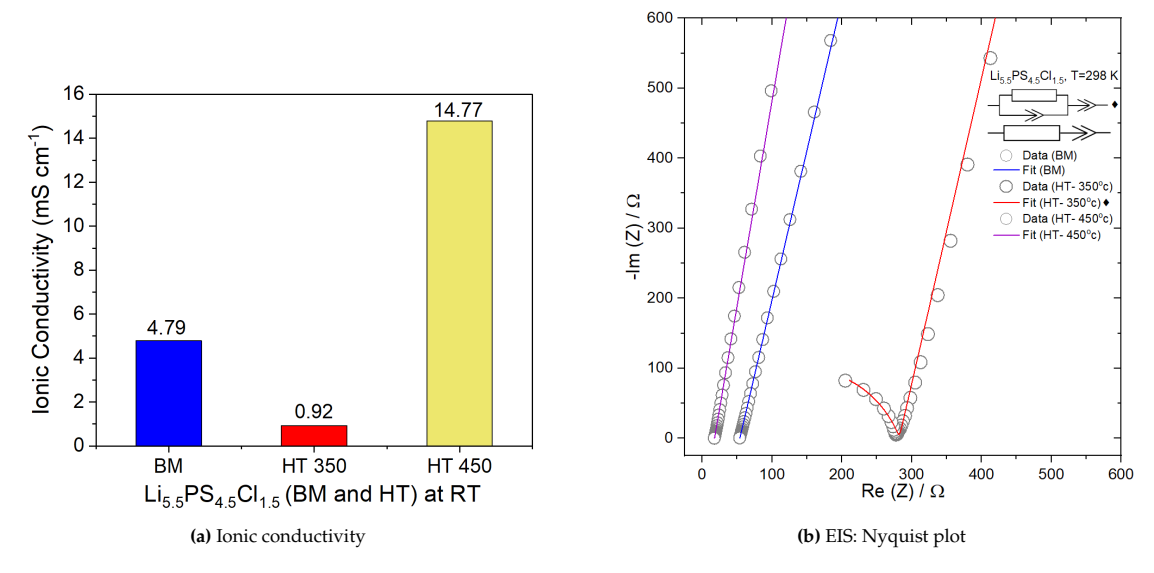
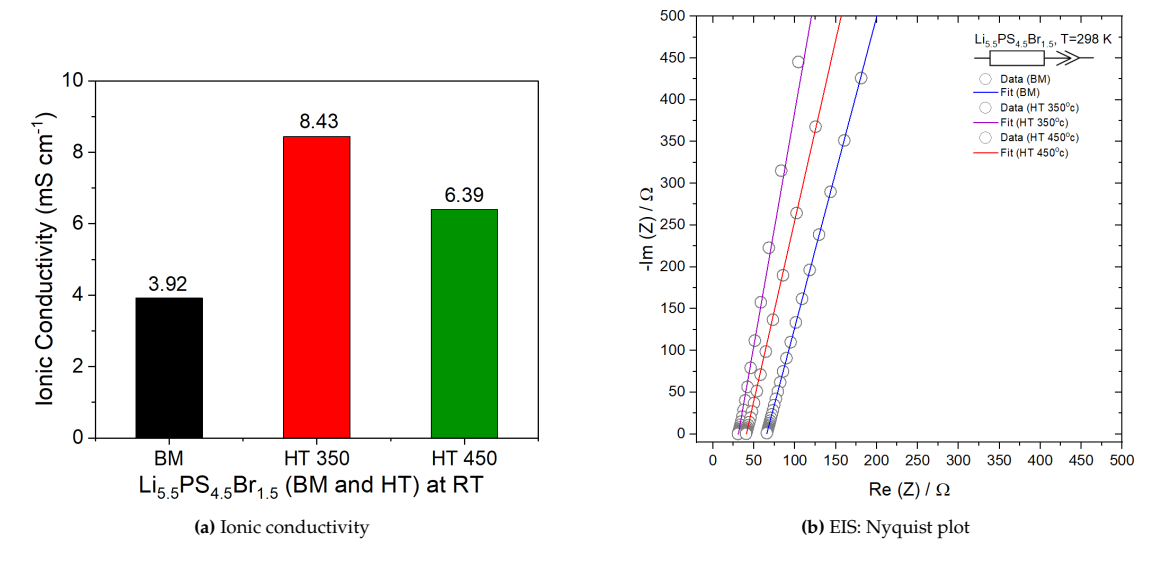


Figure 4.22: Ionic conductivity and EIS fit with equivalent circuit of  $Li_{5.5}PS_{4.5}Cl_{1.5}$  at room temperature

The figure 4.22 (a) and (b) describes the ionic conductivity and the EIS spectra fitting of the  $Li_{5.5}PS_{4.5}Cl_{1.5}$  which is BM and HT samples showing the conductivity of 4.79 and 14.77 mS  $cm^{-1}$ , respectively. we see the HT 350°C sample of  $Li_{5.5}PS_{4.5}Cl_{1.5}$  has more impurities as described in the X-ray diffraction section as shown in the figure 4.10 (b) which contributes to the higher resistance which lowers the ionic transport.

In figure 4.23 (a) and (b), Unlike the other samples which we previously covered, the  $Li_{5.5}PS_{4.5}Br_{1.5}$  exhibits an varying trend and describes the optimal annealing temperature for better ionic conductivity. In figure 4.23 (a), we observe that the HT 350°C sample has higher ionic conductivity of 8.43 mS  $cm^{-1}$  while compared to BM or HT 450°C due to the presence of LiBr impurity which was observed in the XRD pattern as shown in the figure 4.12 and the conductivity reduces when the annealing temperature increases to 450°C impacts to reduction in the LiBr impurities gives the conductivity of 6.39 mS  $cm^{-1}$ ,[83]. While the BM samples of  $Li_{5.5}PS_{4.5}Cl_{1.5}$  and  $Li_{5.5}PS_{4.5}Br_{1.5}$  have similar ionic conductivities, the higher-temperature synthesis of  $Li_{5.5}PS_{4.5}Cl_{1.5}$  results in greater ionic conductivity compared to  $Li_{5.5}PS_{4.5}Br_{1.5}$ . This difference is attributed to the higher disorder found in  $Li_{5.5}PS_{4.5}Cl_{1.5}$  (around 67%) compared to  $Li_{5.5}PS_{4.5}Br_{1.5}$  (around 64%). As a previous study suggested with increasing the halide content in lithium argyrodites, the changes in the lithium distributions, and inter-cage jump distance, influence the higher ionic conductivity.



**Figure 4.23:** Ionic conductivity and EIS fit with equivalent circuit of *Li*<sub>5.5</sub>*PS*<sub>4.5</sub>*Br*<sub>1.5</sub> at room temperature

#### 4.3.6. Temperature-dependent EIS and Activation Energy

In this section, it describes about the Arrhenius plot and the activation energy of each sample to determine the energy barrier required for lithium-ion to move. The slope value has been taken from Arrhenius plot Ln  $\sigma$ T vs 1000/K to determine the activation energy. All the samples were investigated using the climate chamber measuring from varying temperature form  $0^{\circ}$ C to  $-50^{\circ}$ C with the step-size of  $10^{\circ}$ C for an interval of 2 hour, to stabilized the particular temperature on compositions.

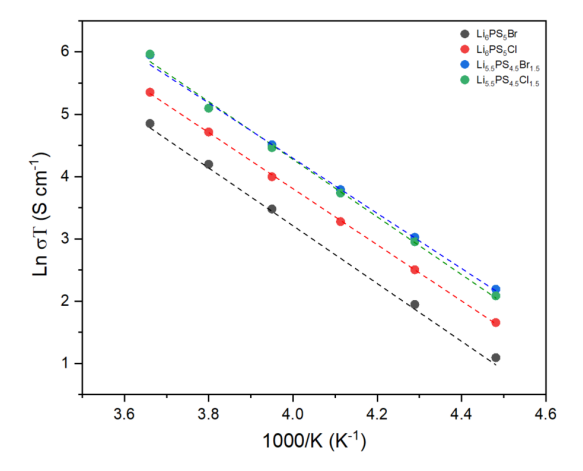


**Figure 4.24:** Arrhenius plot of the BM samples of Cl1, Br1, Cl1.5, and Br1.5 measured in varying temperatures from  $0^{\circ}$ C to  $-50^{\circ}$ C using the climate chamber

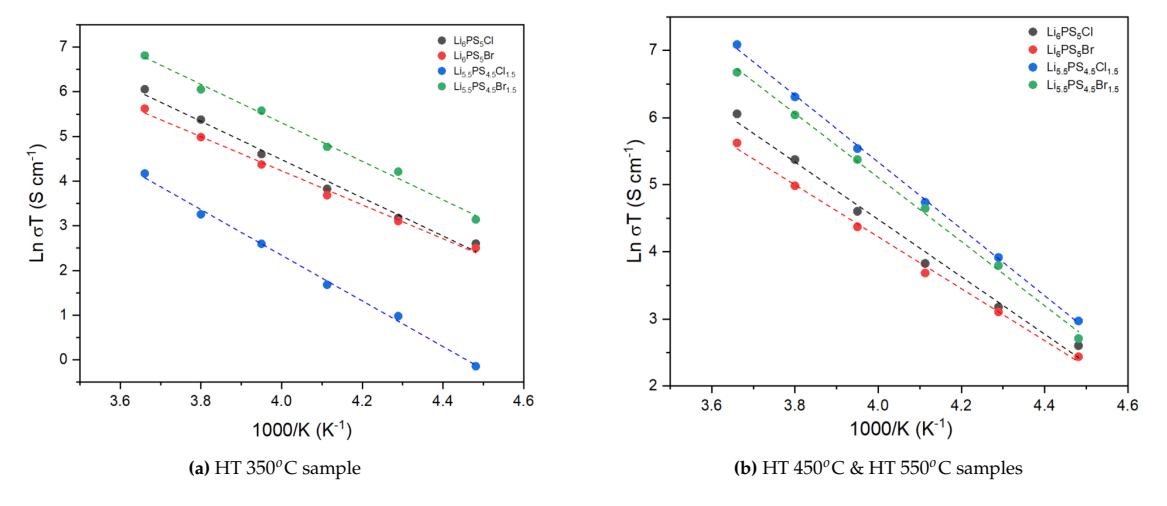


Figure 4.25: Arrhenius plot of the samples of Cl1, Br1, Cl1.5, and Br1.5 measured in varying temperatures from 0°C to -50°C

The figure 4.24 describes Arrhenius plot of the BM samples of Cl1, Br1, Cl1.5 and the Br1.5 was measured at varying temperatures from  $0^{\circ}$ C to  $-50^{\circ}$ C and plotted the natural logarithmic function of the Ionic conductivity. Similarly, in the figure 4.25 (a) and (b) were also plotted and the linear fit to determine the slope of the curve.

The halide enriched composition exhibits the better ionic conductivity while compared to the  $Li_6PS_5X$  (X= Cl, Br) which indicates the increase in anionic site-disorder in the Wyckoff 4d site as the  $X^-$  occupying the free sulfur sites  $S^{2-}$  indicating the high ionic transport,[59].

The figure 4.26 (a) shows the activation energy of  $Li_6PS_5Cl$  sample which was treated in BM and HT shows that the HT 550°C exhibits the lower activation energy of 0.34 eV while compared

to the BM sample with activation energy of 0.38 eV. since the activation energy required by the lithium ion to cross the energy barrier is lower for the  $Li_6PS_5Cl$  (HT 550°C), thus it has high ionic conductivity of 5.63 mS  $cm^{-1}$ . Identically, for the  $Li_6PS_5Br$  as shown in the figure 4.26 (b) the activation energy for the HT 550°C sample is lower than the BM with the hopping energy of 0.31 and the ionic conductivity of 3.33 mS  $cm^{-1}$ .

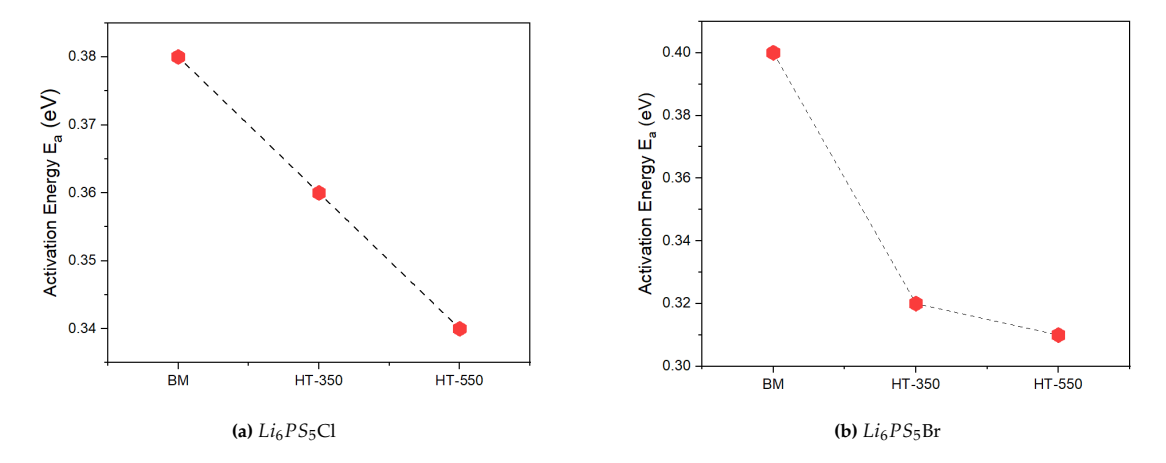
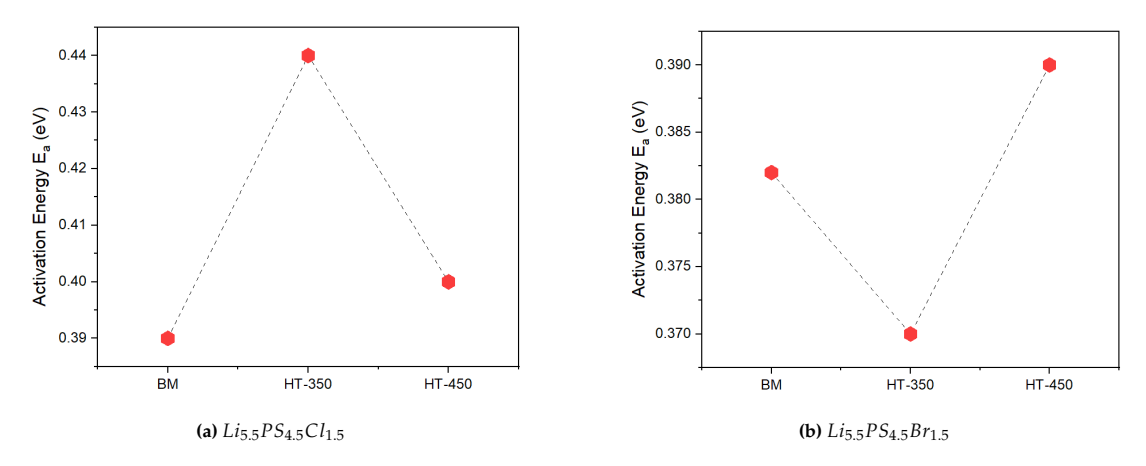


Figure 4.26: Activation energy of BM and HT samples of Li<sub>6</sub>PS<sub>5</sub>Cl and Li<sub>6</sub>PS<sub>5</sub>Br



**Figure 4.27:** Activation energy of BM and HT samples of  $Li_{5.5}PS_{4.5}Cl_{1.5}$  and  $Li_{5.5}PS_{4.5}Br_{1.5}$ 

The activation energy of  $Li_{5.5}PS_{4.5}Cl_{1.5}$  and  $Li_{5.5}PS_{4.5}Br_{1.5}$  compositions doesn't have any specific trend as followed when compared with the  $Li_6PS_5Cl$  and  $Li_6PS_5Br$ , but possibly the presence of the impurities in the HT 350°C samples can alter the way of ion diffusion in the material characteristics, as said in the XRD observations. However, these sample's behavior is observed that higher ionic conductivity is seen in the higher activation energy as compared to within the BM and HT samples, which follow the Meyer-Neldel rule, [84].

# 4.4. Experimental challenges

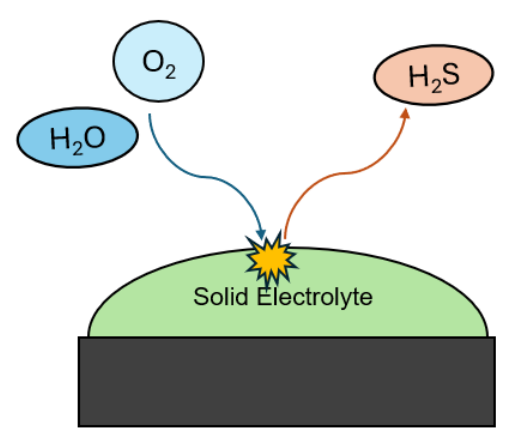
During the synthesis of lithium argyrodite with halide substitution, the process faced significant challenges in making the composition and the processability of the process is more complex and harder, it wasn't a quicker option, and the synthesis of the lithium argyrodite had few implications such as cake formation and the air sensitivity of the samples.

The cake formation occurs during the synthesis of the lithium argyrodite in the high energy ball milling, due to the high speed rotation and the subsequent abrasion causing lithium sulfide and other precursors to form agglomeration and eventually these gets accumulated over the specific region inside the ball mill jars as shown in the figure 4.28 (a).

These accumulation are removed using the spatula after every 30 cycles to synthesize the appropriate product. The cake formed over the walls of jar are extremely difficult to retrieve from the jars and the some portion of the product adhered to the  $ZrO_2$  beads and derived lower product than expected quantity.



(a) Cake formation after 30 cycles



**(b)** Schematic representation of air sensitivity of solid electrolyte in presence of the air and moisture

Figure 4.28: Experimental challenges

Regarding the air sensitivity of the material, the lithium argyrodite are highly reactive to the atmospheric oxygen and humidity causing them to react and increase in resistance which attributes to decrease in the ionic conductivity of the material as well as generation of toxic  $H_2S$  (Hydrogen Sulphide) gas,[85] as shown in the figure 4.28(b).

#### 4.5. Conclusion

In this chapter 4 specifically focused on the synthesis and characterization of the halide enriched lithium argyrodite. We have discussed the synthesis of lithium argyrodite using the high energy

4.5. Conclusion 44

ball milling and the heat treated to achieve the high ionic conductive material.

Following points will help us understand the chapter 4 findings from the experiments carried out:

- The samples were characterized using the XRD, SEM, Temperature-dependent EIS, and Raman spectroscopy to determine the structural and electrochemical properties.
- Processing of the ball milled composition and followed by high temperature annealing has significant impact in the crystallinity of the cubic structure.
- All the samples has the same structural symmetry of F43m of crystal lattices. However, impurities of  $Li_{15}(PS_4)_4Cl_3$  were found only in the heat-treated  $Li_{5.5}PS_{4.5}Cl_{1.5}$  sample at 350°C.
- The SEM image of both BM and HT shows the increase in annealing temperature had implications over the decrease in the micro-grain agglomeration over the surface of the solid electrolyte.
- The Raman spectroscopy reveals the presence of PS<sub>4</sub><sup>3-</sup> tetrahedral volume, indicating that after ball milling, lithium argyrodite can form, and heat treatment can further improve crystallinity.
- Apart from processing, the increase in halide content in the lithium argyrodite composition shows the increase in the anionic site-disorder (or halide in 4d occupancies) attributing to the more inter-cage and change in lithium distributions, improved the higher ionic conductivity.
- The BM and HT samples had significant changes in ionic conductivity were all the HT samples have better ionic conductivity than the BM among in which the  $Li_{5.5}PS_{4.5}Cl_{1.5}$  has the highest ionic conductivity of 14.77 mS  $cm^{-1}$  of HT  $450^{\circ}$ C sample.
  - All the supplementary information and individual plots are mentioned in the Appendix A.

# Electrochemical Stability of the halide substituted Lithium Argyrodite

#### 5.1. Introduction

Previously in this thesis, we have seen about the synthesis and characterization of the lithium argyrodite samples at various annealing temperatures. The results and conclusion from the previous chapter shows the halide enriched lithium argyrodite at high annealing temperature shows an significantly higher ionic conductivity which attributed to this chapter's proceedings.

Here, in this chapter 5, we will discuss about the electrochemical stability window of the halide substituted lithium argyrodite solid electrolyte where the samples of chloride and bromide enriched lithium argyrodite.

Even though the LPSC and LPSB shows an excellent ionic conductivity in an order of  $10^{-2}$  to  $10^{-3}$   $Scm^{-1}$ , these solid electrolyte has the few complications in-terms of interfacial electrochemical processes which can be limiting for the lithium diffusion to the electrode region,[86].

# 5.2. Electrochemical stability window of the lithium argyrodite

In solid-state batteries, particularly those using lithium argyrodite solid electrolytes, higher safety and performance can be achieved with a Li/Si anode. However, these solid electrolytes have a limited electrochemical stability window, which can lead to the decomposition of the solid electrolyte,[86]. It is important to increase the stability window, and this section discusses the electrochemical stability and how it can be improved with halide content.

# 5.3. Experimental methods

we might think that how is the electrochemical stability window contributes in the stability of the battery performance. The electrochemical stability is mainly disrupted when the battery is charged or discharged at high voltage causing the material to fall into the redox reaction leading to decomposition and formation of undesired interface composition which reduces the ionic conductivity of the solid electrolyte and attributing to the lower performance, [86]. The solid electrolyte's stability window is determined using various methods such as cyclic voltammetry (CV) or thermodynamic formation which reports either over-measured or under-measured, respectively [86]. The technique which have been used here in this thesis to determine the stability window of the solid electrolyte is the Linear sweep voltammetry (LSV) to measure the actual potential window.

This section describes us about the experimental methods behind the Electrochemical Stability of enriched Chloride and bromide-substituted Lithium Argyrodites by using the linear sweep voltammetry (LSV) determines the oxidation and reduction of the solid electrolyte.

# 5.3.1. Linear Sweep Voltammetry

In the solid-state cell, the Linear sweep voltammetry is measured by applying the constant increasing voltage over the period of time and obtaining the change in the current as output to determine the electrochemical properties of the solid electrolyte as shown in the below figure 5.1.

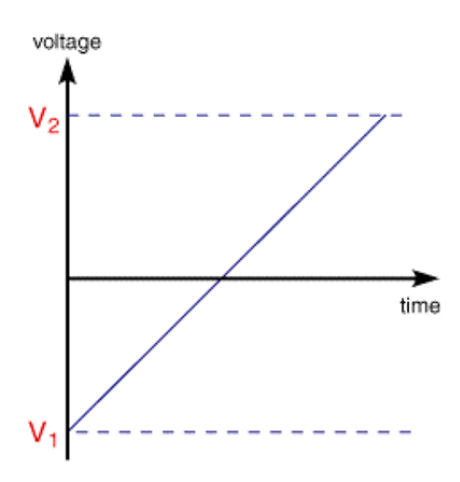


Figure 5.1: Linear sweep voltammetry,[87]

The cell is placed and its charged for oxidation (de-lithiated) and discharged for reduction (lithiated), respectively [88]. The figure clearly shows us the diffusion of lithium ions from anode as its acts to be more like a source or sink during the LSV showing the decomposition

rate with respect to change in the potential and the obtained the current.

Typically, in the reduction procedure the lithium content in the solid electrolyte is completed swept out from the open framework to the cathode region (red dashed box) causing the decomposition of solid electrolyte over the varying voltage. Similarly, for the oxidation as shown in the figure 5.2 (b) represents by charging the lithium ion causing the lithium in SE are forced to move towards anode and the lithium metal in the anode acts to be sink (red dashed box) here,[89]. During the redox reaction, the lithium argyrodite decomposes to several by-products which can cause increase in resistance making less ionic conductive in the cell.

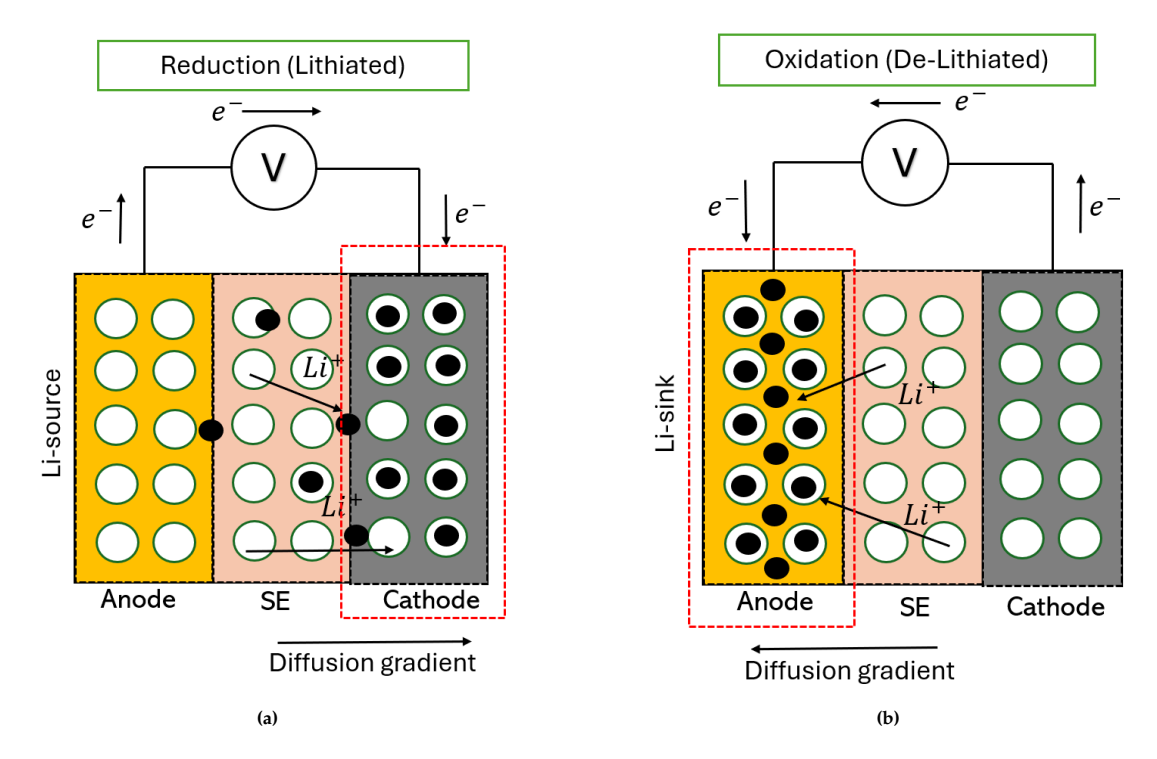


Figure 5.2: Redox reaction showing lithium-ion diffusion with lithium ions (black dots) and the vacant sites (empty holes)

# 5.3.2. Preparation of cathode material and cell assembly for LSV

This section describes us the preparation cathode material using carbon nanofiber and the solid electrolyte mixture and cell assembly to obtain the electrochemical stability window by using linear sweep voltammetry.

The preparation of the SE-CNF cathode mixture is initially started with the drying of carbon nanofiber (CNF) with >98% of carbon basis (conical platelets) in the Büchi oven at 290°c for 24 hours under vacuum condition to remove the moisture content from the CNF. Then the cathode mixture is prepared by mixing the SE and CNF in the ratio of 85% and 15%,

respectively[90]. Later, the material was hand grounded for 15 minutes using mortar and pestle to obtain uniform mixture of cathode material.

The figure 5.3 shows cell assembly for the linear sweep voltammetry (LSV) and the components are measured precisely before layering into the SSB cell. The components are weighed about 15mg of SE-CNF mixture, 85mg of SE are pre-casted in the PEEK before placing the anode components. To put this in simple terms, the SSB PEEK was filled with 85mg of SE and applied 312 MPa of moulding pressure using the automatic press for 5 minutes , similarly followed for the cathode mixture is pressed for 392 MPa for 5 minutes and then the anode lithium metal (6mm diameter) is placed between the reference electrode indium metal (8mm diameter) and the SE. Before closing the copper foil is used as current collector in the anode side with the closing pressure of 63 MPa for 3 minutes was applied to exhibit uniform pressure across the cell.

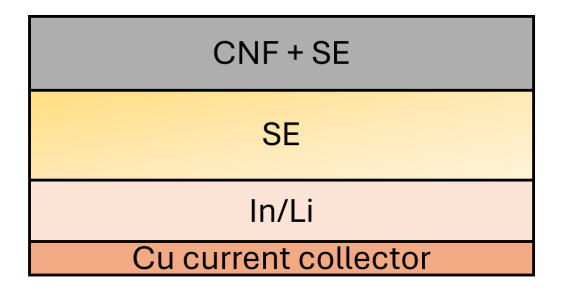


**Figure 5.3:** Cell packing for linear sweep voltammetry to determine the electrochemical stability window of the lithium argyrodite solid electrolyte

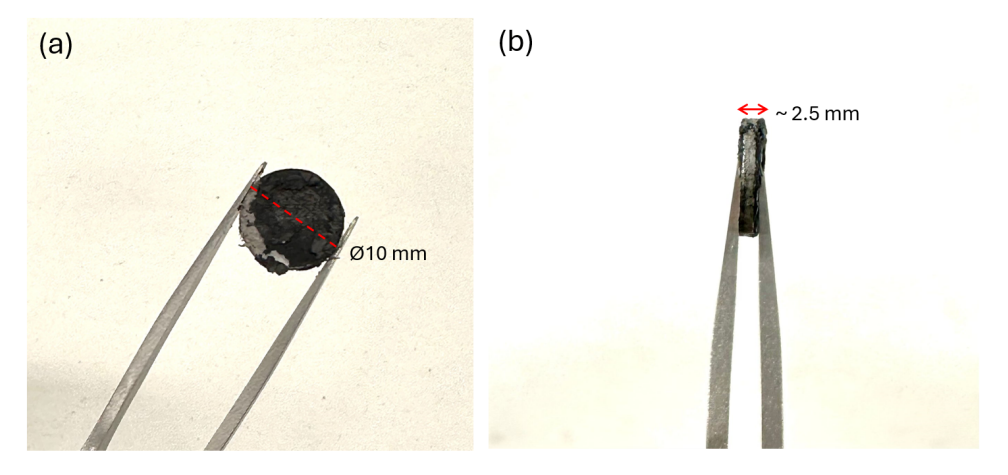
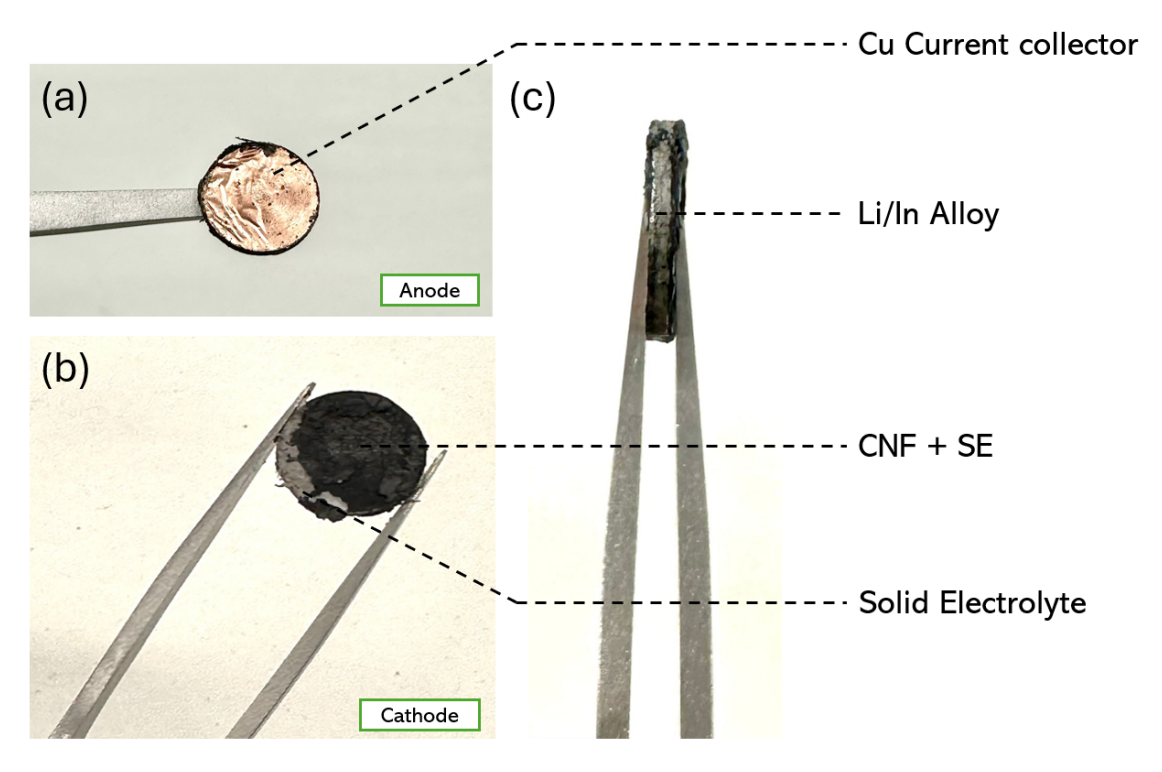


Figure 5.4: Postmortem of the packed cell showing the (a) Circumference and (b) thickness of the cell

For the LSV measurement, the cell was tested for the open circuit voltage and placed in the MACCOR (battery test system) to determine the electrochemical stability window by constantly withdrawing the current of 5  $\mu$ A from OCV to -0.6 V as the standard procedure for reduction. Similarly for oxidation, the cell was constantly charged from the OCV to 5V with 5  $\mu$ A. The data points were obtained with the scan-rate of 0.1 mV/s,[91].



**Figure 5.5:** Postmortem of the cell packing retrieved after the linear sweep voltammertry showing the (a) Anode side, (b) Cathode side, and (c) side view of cell

The figure 5.4 was the sample retrieved after the LSV showing the circumference of 10 mm and the cell thickness of  $\approx$  2.5 mm. The typical cell assembly is shown in the figure 5.5 represents the cell assembly and in figure (c) the position of Li-In alloy as an thin shiny metal indicating the presence in the cell formation.

The data points are obtained by measuring the capacity and voltage. The plots are pitched by plotting the first derivative of the capacity with respect to the voltage  $(\frac{dQ}{dV})$  versus the voltage potential vs In/ $Li^+$  (V) to determine the initial decomposition curve.

Recent studies have revealed the decomposition of the solid electrolyte as described below for  $Li_6PS_5Cl$ , during oxidation the cell is charged in increasing voltage with respect to over the period of time causing  $Li_6PS_5Cl$  decomposes to form the S,  $P_2S_5$  as the oxidative by-products

as given in the equation 5.1,[92].

$$\text{Li}_6\text{PS}_5\text{Cl} \to \text{LiCl} + \frac{1}{2}\text{P}_2\text{S}_5 + \frac{5}{2}\text{S} + 5\text{Li}^+ + 5\text{e}^-$$
 (5.1)

Similarly, for the reduction of  $Li_6PS_5Cl$  it was completely discharged and the reductive by-products causing the internal resistance are LiCl,  $Li_3$ , and  $Li_2S$  as shown in the equation 5.2,[92].

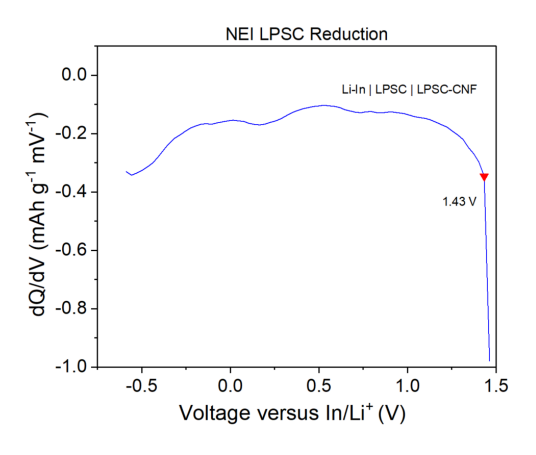
$$\text{Li}_6\text{PS}_5\text{Cl} + 8\text{Li}^+ + 8\text{e}^- \rightarrow \text{Li}\text{Cl} + \text{Li}_3\text{P} + 5\text{Li}_2\text{S}$$
 (5.2)

# 5.4. Results and discussion

This section in this chapter 5 describes the results that obtained from the linear sweep voltammetry of the halide rich lithium argyrodite to determine the electrochemical stability window.

# 5.4.1. Chloride-rich lithium argyrodite

In this subsection, we will see the results obtained from the LSV of the Chloride-rich solid electrolyte exhibiting it's electrochemical stability window and measured with the presence of In/Li alloy in the anode side which plays more like a source for reduction and the sink during the oxidation and the indium exhibiting 0.6V vs Li/ $Li^+$  [93] potential which is added with the obtained LSV to determine the actual electrochemical stability window.



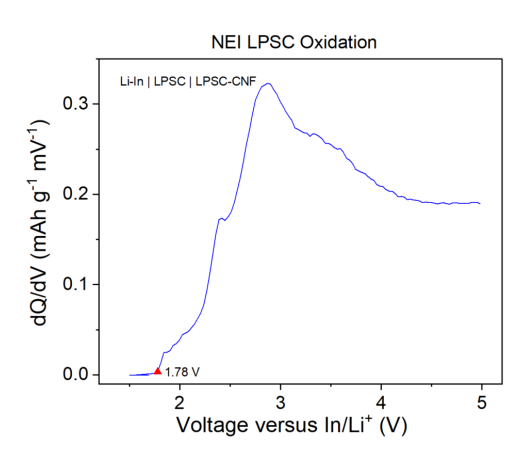


Figure 5.6: Electrochemical stability window of the LPSC (NEI corporation) commercial

The figure 5.6 shows the LSV of the LPSC (NEI corporation) commercial solid electrolyte was tested to demonstrate as an reference which is compared with the synthesized material, the redox degradation is notably occurring in the range of 1.43 to 1.78 V potential versus  $In/Li^+$  and showing the decomposition beyond the voltage window which exhibits the redox reaction in the solid electrolyte. Recent studies shows upon charging the LPSC decomposes to the following by-products as LiCl,  $P_2S_5$ , S as complete oxidative compounds. similarly, for

the reduction the LPSC decomposes to form the fully reduced by-products of  $Li_2S$ ,  $Li_3P$ , LiCl causing significant increase in the cell resistance and making less ionic conductive,[92].

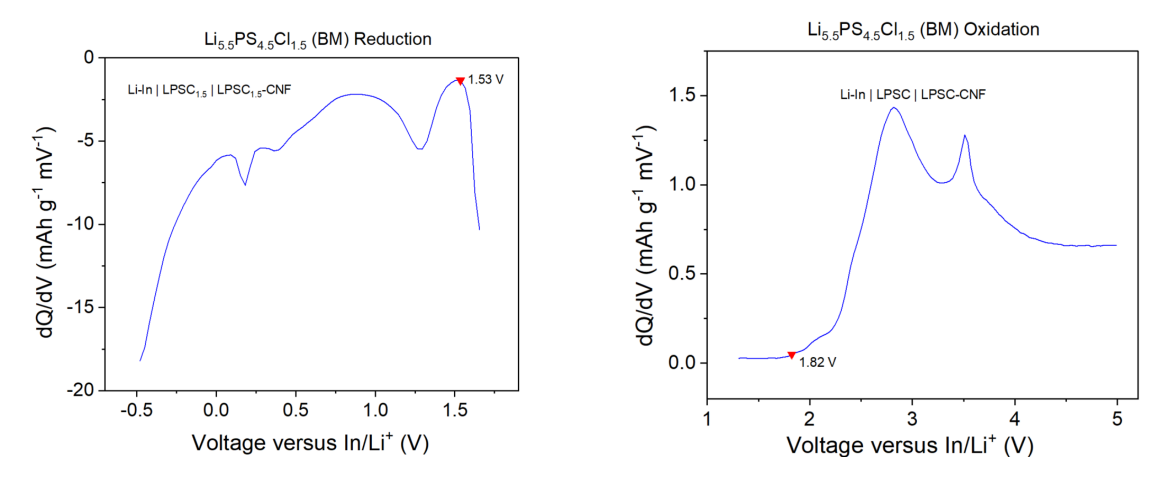
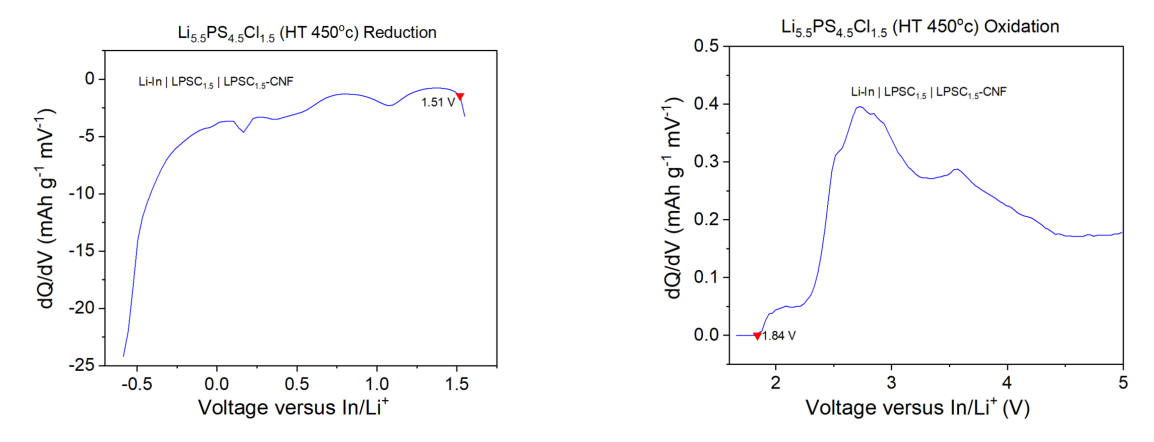


Figure 5.7: Electrochemical stability window of the Li<sub>5.5</sub>PS<sub>4.5</sub>Cl<sub>1.5</sub> (BM)

Similarly, for  $Li_{5.5}PS_{4.5}Cl_{1.5}$  ball milled sample exhibits the narrow electrochemical stability window compared to the LPSC (NEI corporation) and while recent studies shows that due to the presence of amorphous material it exhibits the narrow potential window, whereas after the heat treatment of the lithium argyrodite leads to more crystalline cubic structure as we discussed in the previous chapter 4 showing the difference in the stability window,[94]. The heat treated samples has narrow electrochemical stability window while compared to the ball milled sample and compared to the commercial LPSC (NEI corporation). As we see the table 5.1 below describes the actual electrochemical stability window of the solid electrolyte after the including the potential of 0.62V versus  $\text{Li}/Li^+$ ,[93].



**Figure 5.8:** Electrochemical stability window of the  $Li_{5.5}PS_{4.5}Cl_{1.5}$  (HT 450°C)

Composition	Reduction	Oxidation	Difference
NEI LPSC	1.43	1.78	0.35
Cl 1.5 BM	1.53	1.82	0.29
Cl 1.5 HT	1.51	1.84	0.33

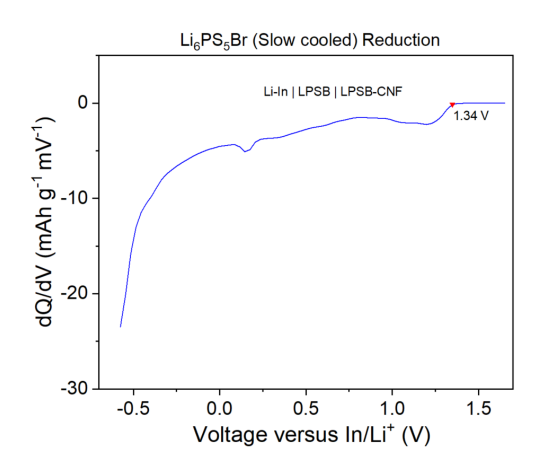
**Table 5.1:** Electrochemical stability window of the chlorine rich lithium argyrodite solid electrolyte voltage versus  $In/Li^+$ 

# 5.4.2. Bromide-rich lithium argyrodite

In this subsection, we have continued the work of Gautam, et al [59] were the lithium argyrodite with bromide enriched composition was synthesized and heat treated at designated temperatures. Slow cooling was attained to achieve crystalline structure and better ionic conductivity. Here, we have determined the electrochemical stability window of these composition to better understand the stability and potential window versus  $\ln/Li^+$ .

XRD was conducted to examine the structure and shows the purity of the synthesis and the XRD patterns are shown in the appendix A.5.3.

The figure 5.9 shows both the obtained reduction and the oxidation values of the  $Li_6PS_5Br$  standard cooled exhibits the actual stability window of 1.34 to 1.5V as shown in the below table 5.2 and taken as the base composition in this subsection. The figure 5.10 and 5.11 compositions with increasing bromine content the lithium argyrodite shows the trend of extended electrochemical stability window while compared to the base composition, [62].



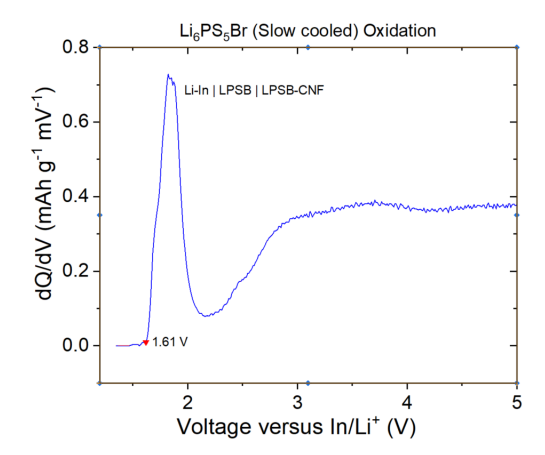
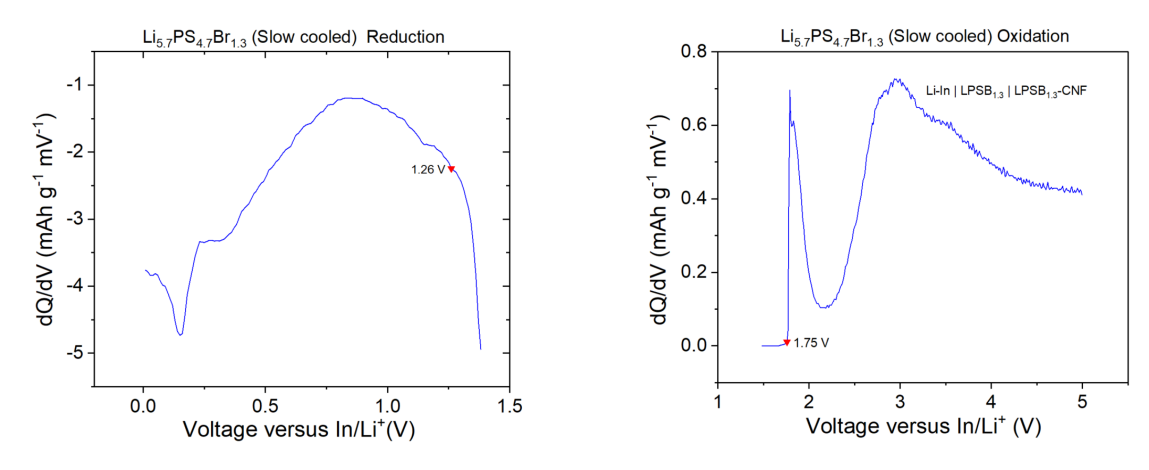


Figure 5.9: Electrochemical stability window of the Li<sub>6</sub>PS<sub>5</sub>Br (HT 550°C) Slow cooled



**Figure 5.10:** Electrochemical stability window of the  $Li_{5.7}PS_{4.7}Br_{1.3}$  (HT 450°C) Slow cooled

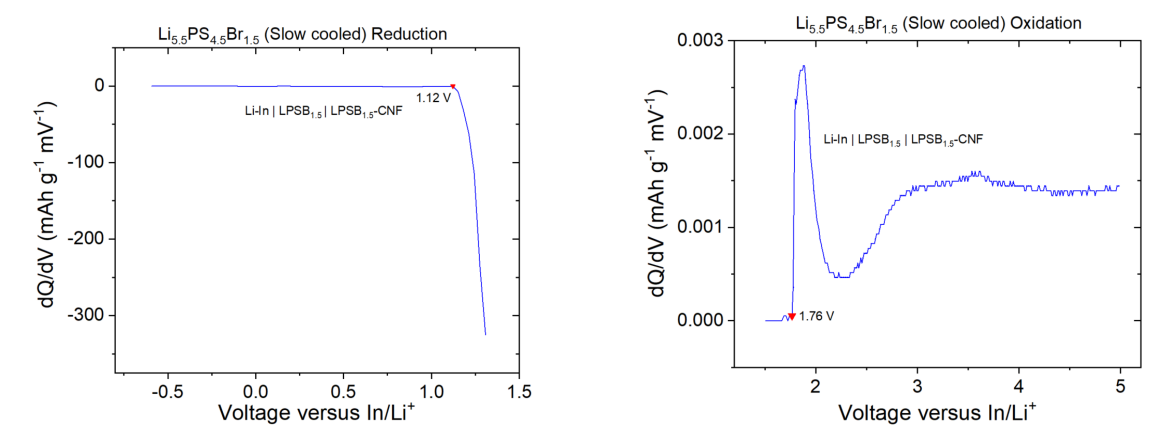


Figure 5.11: Electrochemical stability window of the  $Li_{5.5}PS_{4.5}Br_{1.5}$  (HT 450°C) Slow cooled versus In/ $Li^+$ 

The above table 5.2 shows the actual electrochemical stability window versus  $\text{Li}/\text{Li}^+$  exhibits the increasing stability window due to the increase in the halide substitution content [62].

Composition	Reduction	Oxidation	Difference
Br	1.34	1.61	0.27
Br 1.3	1.26	1.75	0.49
Br 1.5	1.12	1.76	0.64

**Table 5.2:** Actual electrochemical stability window of the Bromine rich lithium argyrodite solid electrolyte voltage versus  ${\rm In}/Li^+$ 

The study shows that higher ionic conductivity was achieved with increasing bromide content in lithium argyrodites [59]. We found that increasing the bromide content leads to an increase in electrochemical stability from 0.27 V to 0.64 V. This suggests that substituting sulfur with

5.5. Conclusion 54

bromide can improve the oxidation stability, while the reduction stability should remain unchanged since the phosphorus element is not being altered. However, due to higher site disorder, more lithium vacancies, and potentially other factors, there may be an improvement in reduction stability. Overall, we observed that the stability window for  $Li_{5.5}PS_{4.5}Br_{1.5}$  is around 0.64 V, while for  $Li_{5.5}PS_{4.5}Cl_{1.5}$ , it is around 0.33 V

# 5.5. Conclusion

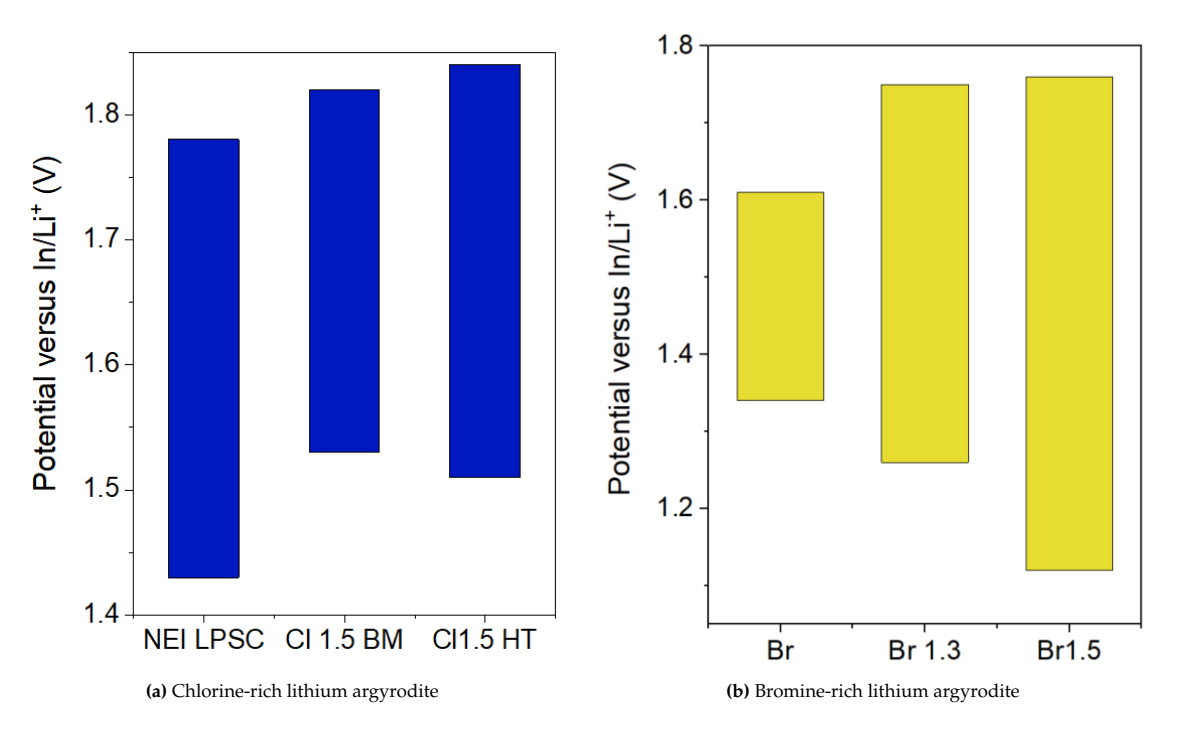


Figure 5.12: Electrochemical stability window

Similarly, the figure 5.12 (b) shows the increasing trend in the bromine rich lithium argyrodite due to an increase in the bromine content (X= 1, 1.3, 1.5) significantly broadens the electrochemical stability window.

In conclusion, the study highlights the electrochemical behavior of various lithium argyrodite solid electrolytes, emphasizing the impact of different halide substitutions on stability and ionic conductivity. The commercial LPSC (NEI Corporation) electrolyte demonstrated notable redox degradation within a potential range of 1.43 to 1.78 V versus  ${\rm In}/Li^+$ , decomposing into several by-products that increase cell resistance and reduce ionic conductivity. Comparatively, the BM synthesized  $Li_{5.5}PS_{4.5}Cl_{1.5}$  exhibited a narrower electrochemical stability window compared to heat treatment composition at  $450^{\rm o}{\rm C}$ , which is attributed to the presence of amorphous material that limits its stability. Furthermore, it was observed that increasing the bromide content in lithium argyrodites significantly enhances the electrochemical stability, with a marked increase in the stability window from 0.27 V to 0.64 V. This improvement is

5.5. Conclusion 55

linked to the substitution of sulfur with bromide, which enhances oxidation stability while maintaining reduction stability. The presence of higher site disorder, lithium vacancies, and possibly other factors, also contributed to improved reduction stability.

Overall, the study concludes that  $Li_{5.5}PS_{4.5}Br_{1.5}$  offers a broader stability window of around 0.64 V compared to the 0.33 V window observed for  $Li_{5.5}PS_{4.5}Cl_{1.5}$ , suggesting that bromide substitution may be a promising strategy for optimizing solid electrolytes in lithium-ion batteries.

# Conclusion and Outlook

# 6.1. Conclusion

This thesis mainly focused to provide an overview of synthesizing and material characterization of the lithium argyrodite solid electrolyte with halide-rich substitution and explaining their electrochemical properties. This section explains all the experimental findings for the above discussed research questions as shown in the chapter 3. Below points describe the findings and solution to the questions.

# 1. How does the halide-rich substitution improves the ionic conductivity in the lithium argyrodite sulfide solid electrolyte in solid-state batteries?

The main research question was addressed by synthesizing the halide enriched lithium argyrodite solid electrolyte was compared with X= Cl, Br were synthesized using the high energy ball milling and was tested under X-Ray diffraction, SEM, Raman spectroscopy, and EIS. Lithium argyrodite with the halide enriched substitution in  $Li_{5.5}PS_{4.5}Cl_{1.5}$  have shown higher ionic conductivity with 14.77 mS  $cm^{-1}$  at HT 450°C and the F43m as the crystal lattice structure.

Apart from this, both BM and HT have obtained morphological and structural difference in which the HT sample shows significantly crystalline structure whereas the BM samples are more amorphous and shows more micro-agglomeration in the SEM images. Additionally, after the raman spectroscopy shows the presence of the  $PS_4^{3-}$  tetrahedral shows that after ball milled argyrodite has be formed.

Synthesized the halide enriched lithium argyrodite solid electrolyte were compared with X= Cl, Br which gave us the overview and due to the presence of the lithium vacancy and change in lithium distributions and more inter-cage could improved better ionic conductivity as discussed in the chapter 4.

6.1. Conclusion 57

## 2. How lithium argyrodite sulfide with halide substitution are made and how does the annealing process impact in the ionic conductivity of the solid electrolyte?

The halide enriched lithium argyrodite was synthesized used the high energy ball milling and heat treated at suitable temperature to achieve crystallinity due to the presence uniform repetitive pattern which provides the open framework for better lithium ion diffusion. As discussed previously in the chapter 4, the SEM morphology and XRD pattern shows the purity of the synthesis and EIS proves the impact of annealing as the heat treated samples show better ionic conductivity than ball milled sample.

The temperature dependent EIS was conducted shows an overview to determine the activation energy of the halide enriched lithium argyrodite. The results shows that the  $Li_6PS_5Cl$  and  $Li_6PS_5Br$  follows the trend of decreasing activation in increase in heat treatment of the sample, whereas the halide enriched lithium argyrodite hasn't followed any pattern but activation energy of the BM is lesser while compared to HT samples.

## 3. Structural parameter such as lattice parameter, site disorder influencing the ionic conductivity in lithium argyrodite?

Structural parameters of the synthesized halide enriched lithium argyrodite solid electrolyte was obtained using the XRD and the neutron diffraction characterization which revealed the space group, lattice parameter, and site disorder which provided an better understanding of the composition. After the XRD refinement,  $Li_6PS_5Cl$  and  $Li_6PS_5Br$  shows the cubic crystal lattice with F43m space group and expansion of the unit cell and volume due to increase in lattice parameters has seen over from BM to HT samples. While the halide enriched have different pattern due the phase segregation at HT 350°C shows the presence of impurities impacting the lattice parameters. The  $Li_{5.5}PS_{4.5}Cl_{1.5}$  HT 450°C shows higher lattice parameter while compared to BM sample with high ionic conductivity, but  $Li_{5.5}PS_{4.5}Br_{1.5}$  HT 450°C shows the different trend as the lattice parameter decreased compared to BM sample.

After the neutron diffraction refinement the site disorder of the halide occupancy in the Wyckoff 4a and 4d sites of all the BM and HT compositions and the results obtained shows us the HT 350°C samples showed 66% site disorder while it slightly decreased to 65% after the heat treatment showing the crystallinity in the  $Li_6PS_5Cl$ . Similarly in the  $Li_{5.5}PS_{4.5}Cl_{1.5}$  HT 450°C shows the higher halide content in the 4d and 4a site around 67 and 83 %, respectively but it wasn't influenced by varying annealing temperature.

## 4. what is the difference in electrochemical stability window while compared with the commercial lithium argyrodite and the halide-rich composition?

The electrochemical stability window of the synthesized halide enrich lithium argyrodite solid electrolyte by using linear sweep voltammetry method in the chapter 5. To conclude the stability window of chloride enriched argyrodite and compared with the commercial LPSC (NEI Corporation) showed similar stability window for  $Li_{5.5}PS_{4.5}Cl_{1.5}$  (450°C) with the potential of 1.84 V to 1.51 V versus In/ $Li^+$  whereas, the commercial LPSC has window of 1.43

V to 1.84 V, maybe higher Chloride content and higher ionic conductivity does influence the stability window. However we found that increasing the bromide content leads to an increase in electrochemical stability from 0.27 V to 0.64 V. This suggests that substituting sulfur with bromide can improve the oxidation stability, while the reduction stability should remain unchanged since the phosphorus element is not being altered. However, due to higher site disorder, more lithium vacancies, and potentially other factors, there may be an improvement in reduction stability. Overall, we observed that the stability window for  $Li_{5.5}PS_{4.5}Br_{1.5}$  is around 0.64 V, while for  $Li_{5.5}PS_{4.5}Cl_{1.5}$ , it is around 0.33 V

#### 6.2. Future recommendation

Till now, the thesis work covered the synthesis and heat treatment of the various composition to achieve a better ionic conductive material to utilize in the formation of solid-state batteries. Inorder to determine the capacity retention by using the cyclic voltammetry to better understand the properties and behaviour of the solid electrolyte in the system.

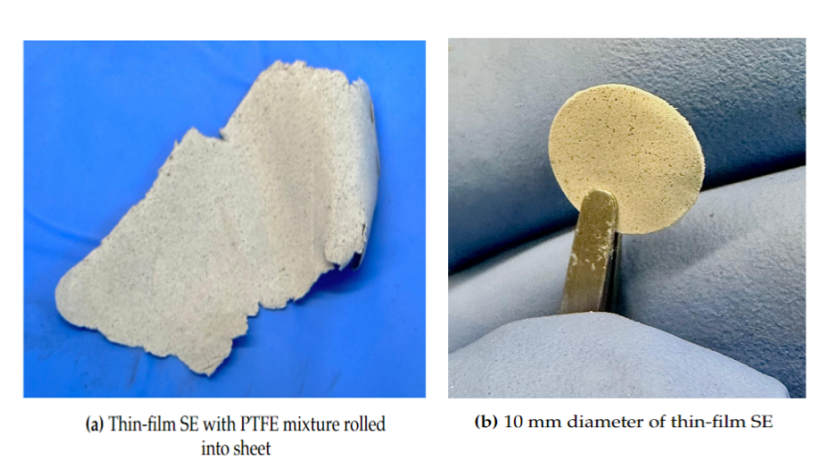


Figure 6.1: Thin-film chlorine rich lithium argyrodite solid electrolyte with PTFE mixture

During the experiment the cells where closed with the closing pressure of 392 MPa making it unreliable to scale-up the cell assembly. But, development of thin film solid electrolyte with halide-rich lithium argyrodite can possibly unlock the cell assembly of solid electrolyte in the pouch cells or coin cells.

As an additional work out of curiosity the thin film were developed using the partial mixture of polytetrafluoroethylene (PTFE) and the solid electrolyte of required ratio and rolled into thin films as shown in the figure 6.1 (a) and punched to 10mm diameter thin-films as shown in the figure 6.1 (b) are used to cell assembly with lesser closing pressure.

- [1] Hannah Ritchie, Pablo Rosado, and Max Roser. "Energy Production and Consumption". In: *Our World in Data* (2020). https://ourworldindata.org/energy-production-consumption.
- [2] IEA. "Electricity market report 2023". In: *IEA, Paris* (2023). https://www.iea.org/reports/electricity-market-report-2023, Licence: CC BY 4.0.
- [3] Valérie Masson-Delmotte et al. *Global Warming of 1.5 C: IPCC special report on impacts of global warming of 1.5 C above pre-industrial levels in context of strengthening response to climate change, sustainable development, and efforts to eradicate poverty.* Cambridge University Press, 2022.
- [4] Ian Tiseo. "Global CO2 emissions by year 1940-2023". In: *Statista* (Dec. 2024). https://www.statista.com/statistics/276629/global-co2-emissions/.
- [5] IRENA(2023). "World Energy Transitions Outlook 2023: 1.5°C Pathway". In: *International Renewable Energy Agency, Abu Dhabi* (2023).
- [6] Mark Z. Jacobson. "Renewable energy's intermittency is not a showstopper". In: *Physics* (Apr. 2022). https://physics.aps.org/articles/v15/54.
- [7] BalancePower. "What are the best types of Battery Energy Storage Systems". In: Balance Power (Sept. 2023). URL: https://balancepower.co.uk/news-insights/what-are-the-best-types-of-battery-energy-storage-systems.
- [8] IEA (2024). "Batteries and Secure Energy Transitions, IEA, Paris-Licence: CC BY 4.0". In: (2024). URL: https://www.iea.org/reports/batteries-and-secure-energy-transitions.
- [9] Kyle Slinger. "Electrical batteries for renewable energy". In: Electrical and Computer Engineering Design Handbook (2015). URL: https://sites.tufts.edu/eeseniordesign handbook/2015/electrical-batteries-for-renewable-energy/.
- [10] Gabriella Jarbratt et al. "Enabling renewable energy with battery energy storage systems". In: McKinsey Company (Aug. 2023). URL: https://www.mckinsey.com/industries/automotive-and-assembly/our-insights/enabling-renewable-energy-with-battery-energy-storage-systems#/.
- [11] UL Research Institutes. What Are Lithium-Ion Batteries? Accessed: 2024-08-03. 2021. URL: https://ul.org/research/electrochemical-safety/getting-started-electrochemical-safety/what-are-lithium-ion.
- [12] Yoshio Nishi. "Lithium ion secondary batteries; past 10 years and the future". In: *Journal of Power Sources* 100.1 (2001). Journal of Power Sources Volume 100, pp. 101–106. DOI: https://doi.org/10.1016/S0378-7753(01)00887-4. URL: https://www.sciencedirect.com/science/article/pii/S0378775301008874.

[13] Nicola Boaretto et al. "Lithium solid-state batteries: State-of-the-art and challenges for materials, interfaces and processing". In: *Journal of Power Sources* 502 (2021), p. 229919. ISSN: 0378-7753. DOI: https://doi.org/10.1016/j.jpowsour.2021.229919. URL: https://www.sciencedirect.com/science/article/pii/S0378775321004511.

- [14] Jens Conzen et al. "Lithium Ion Battery Energy Storage Systems (BESS) hazards". In: *Journal of Loss Prevention in the Process Industries* 81 (Feb. 2023), p. 104932. DOI: 10.1016/j.jlp.2022.104932.
- [15] Hanyu Huo and Jürgen Janek. "Solid-state batteries: From 'all-solid' to 'almost-solid'". In: *National Science Review* 10.6 (Apr. 2023). DOI: 10.1093/nsr/nwad098.
- [16] Kaustubh G. Naik, Bairav S. Vishnugopi, and Partha P. Mukherjee. "Kinetics or Transport: Whither Goes the Solid-State Battery Cathode?" In: *ACS Applied Materials & Interfaces* 14.26 (2022). PMID: 35732069, pp. 29754–29765. DOI: 10.1021/acsami.2c04962. URL: https://doi.org/10.1021/acsami.2c04962.
- [17] Nataly Carolina Rosero-Navarro, Akira Miura, and Kiyoharu Tadanaga. "Preparation of lithium ion conductive Li6PS5Cl solid electrolyte from solution for the fabrication of composite cathode of all-solid-State Lithium Battery". In: *Journal of Sol-Gel Science and Technology* 89.1 (Aug. 2018), pp. 303–309. DOI: 10.1007/s10971-018-4775-y.
- [18] Can Cao et al. "Recent Advances in Inorganic Solid Electrolytes for Lithium Batteries". In: Frontiers in Energy Research 2 (2014). ISSN: 2296-598X. DOI: 10.3389/fenrg.2014.00025. URL: https://www.frontiersin.org/articles/10.3389/fenrg.2014.00025.
- [19] Duygu Karabelli, Kai Peter Birke, and Max Weeber. "A performance and cost overview of selected solid-state electrolytes: Race between polymer electrolytes and inorganic sulfide electrolytes". In: *Batteries* 7.1 (Mar. 2021), p. 18. DOI: 10.3390/batteries7010018.
- [20] Renheng Wang et al. "Lithium metal anodes: Present and future". In: *Journal of Energy Chemistry* 48 (2020), pp. 145–159.
- [21] Dhrubajyoti Das, Sanchita Manna, and Sreeraj Puravankara. "Electrolytes, Additives and Binders for NMC Cathodes in Li-Ion Batteries—A Review". In: *Batteries* 9.4 (2023). ISSN: 2313-0105. DOI: 10.3390/batteries9040193.
- [22] Lee Yong-Gun et al. "High-energy long-cycling all-solid-state lithium metal batteries enabled by silver–carbon composite anodes". In: *Nature Energy* 5.4 (2020), pp. 299–308.
- [23] Cui, Chenqi, Liu, Yanting, and Zhu, Haochen. "Research Progress of All-Solid-State Lithium-Ion Batteries". In: MATEC Web Conf. 386 (2023), p. 03001. DOI: 10.1051/matecc onf/202338603001. URL: https://doi.org/10.1051/matecconf/202338603001.
- [24] William Fitzhugh, Luhan Ye, and Xin Li. "The effects of mechanical constriction on the operation of sulfide based solid-state batteries". In: *Journal of Materials Chemistry A* 7.41 (2019), pp. 23604–23627. DOI: 10.1039/c9ta05248h.
- [25] Tammo K. Schwietert, Alexandros Vasileiadis, and Marnix Wagemaker. "First-principles prediction of the electrochemical stability and reaction mechanisms of solid-state electrolytes". In: *JACS Au* 1.9 (Aug. 2021), pp. 1488–1496. DOI: 10.1021/jacsau.1c00228.
- [26] Marvin A Kraft et al. "Influence of lattice polarizability on the ionic conductivity in the lithium superionic argyrodites Li6PS5X (X= Cl, Br, I)". In: *Journal of the American Chemical Society* 139.31 (2017), pp. 10909–10918.

[27] Longwei Liang et al. "Sur-/interfacial regulation in all-solid-state rechargeable Li-ion batteries based on inorganic solid-state electrolytes: advances and perspectives". In: *Materials Horizons* 6.5 (2019), pp. 871–910.

- [28] Xingfeng He, Yizhou Zhu, and Yifei Mo. "Origin of fast ion diffusion in super-ionic conductors". In: *Nature communications* 8.1 (2017), p. 15893.
- [29] Richard JD Tilley. Defects in solids. John Wiley & Sons, 2008.
- [30] K. Daems et al. "Advances in inorganic, polymer and composite electrolytes: Mechanisms of Lithium-ion transport and pathways to enhanced performance". In: *Renewable and Sustainable Energy Reviews* 191 (2024), p. 114136. ISSN: 1364-0321. DOI: https://doi.org/10.1016/j.rser.2023.114136. URL: https://www.sciencedirect.com/science/article/pii/S1364032123009942.
- [31] Guan Xi et al. "Polymer-based solid electrolytes: material selection, design, and application". In: *Advanced Functional Materials* 31.9 (2021), p. 2007598.
- [32] Duygu Karabelli Kaus, Kai Birke, and Max Weeber. "A Performance and Cost Overview of Selected Solid-State Electrolytes: Race between Polymer Electrolytes and Inorganic Sulfide Electrolytes". In: *Batteries* 7 (Mar. 2021), p. 18. DOI: 10.3390/batteries7010018.
- [33] Saneyuki Ohno et al. "Materials design of ionic conductors for solid state batteries". In: *Progress in Energy* 2.2 (2020), p. 022001.
- [34] Yuqing Chen et al. "A review of lithium-ion battery safety concerns: The issues, strategies, and testing standards". In: *Journal of Energy Chemistry* 59 (2021), pp. 83–99. ISSN: 2095-4956. DOI: https://doi.org/10.1016/j.jechem.2020.10.017. URL: https://www.sciencedirect.com/science/article/pii/S2095495620307075.
- [35] Yi-An Wang et al. "Advances in Inorganic Solid Electrolytes: A Mini Review". In: *JOM* 76.3 (2024), pp. 1131–1142.
- [36] Yohei Yoneda et al. "Preparation and characterization of hexagonal Li4GeO4-based glass-ceramic electrolytes". In: *Solid State Ionics* 363 (2021), p. 115605.
- [37] Junming Shao et al. "Li29Zr9Nb3O40 based Li-ionic conductors as a new system of solid-state electrolytes". In: *Journal of Alloys and Compounds* 816 (2020), p. 152517.
- [38] Sangryun Kim et al. "Low temperature synthesis and ionic conductivity of the epitaxial Li 0.17 La 0.61 TiO 3 film electrolyte". In: *CrystEngComm* 16.6 (2014), pp. 1044–1049.
- [39] Yutao Li et al. "A perovskite electrolyte that is stable in moist air for lithium-ion batteries". In: *Angewandte Chemie International Edition* 57.28 (2018), pp. 8587–8591.
- [40] Liang-Liang Sun et al. "Perovskite-type compounds in anion-substituted LiSr1- 0.5 xTiTaO6- xFx electrolyte for improving lithium-ion conduction". In: *Ceramics International* 45.2 (2019), pp. 2381–2384.
- [41] Zachary D Hood et al. "Li2OHCl crystalline electrolyte for stable metallic lithium anodes". In: *Journal of the American Chemical Society* 138.6 (2016), pp. 1768–1771.
- [42] Yusheng Zhao and Luke L Daemen. "Superionic conductivity in lithium-rich antiperovskites". In: *Journal of the American Chemical Society* 134.36 (2012), pp. 15042–15047.
- [43] Yutao Li et al. "Ionic distribution and conductivity in lithium garnet Li7La3Zr2O12". In: *Journal of Power Sources* 209 (2012), pp. 278–281.

[44] C Deviannapoorani et al. "Lithium ion transport properties of high conductive tellurium substituted Li7La3Zr2O12 cubic lithium garnets". In: *Journal of Power Sources* 240 (2013), pp. 18–25.

- [45] S Ramakumar et al. "Structure and Li+ dynamics of Sb-doped Li 7 La 3 Zr 2 O 12 fast lithium ion conductors". In: *Physical Chemistry Chemical Physics* 15.27 (2013), pp. 11327–11338.
- [46] Ömer Ulaş Kudu et al. "Structural details in Li3PS4: Variety in thiophosphate building blocks and correlation to ion transport". In: *Energy Storage Materials* 44 (2022), pp. 168–179.
- [47] Philipp Bron, Stefanie Dehnen, and Bernhard Roling. "Li10Si0. 3Sn0. 7P2S12–A low-cost and low-grain-boundary-resistance lithium superionic conductor". In: *Journal of Power Sources* 329 (2016), pp. 530–535.
- [48] Pengfei Zhou et al. "A solid lithium superionic conductor Li 11 AlP 2 S 12 with a thio-LISICON analogous structure". In: *Chemical Communications* 52.36 (2016), pp. 6091–6094.
- [49] Hiram Kwak et al. "Li+ conduction in aliovalent-substituted monoclinic Li2ZrCl6 for all-solid-state batteries: Li2+ xZr1-xMxCl6 (M= In, Sc)". In: *Chemical Engineering Journal* 437 (2022), p. 135413.
- [50] Palanivel Molaiyan et al. "Investigation of the structure and ionic conductivity of a Li3InCl6 modified by dry room annealing for solid-state Li-ion battery applications". In: *Materials & Design* 227 (2023), p. 111690.
- [51] Mykhailo Monchak et al. "Lithium diffusion pathway in Li1. 3Al0. 3Ti1. 7 (PO4) 3 (LATP) superionic conductor". In: *Inorganic chemistry* 55.6 (2016), pp. 2941–2945.
- [52] Pilar Maldonado-Manso et al. "High Lithium Ionic Conductivity in the Li1+ x Al x Ge y Ti2-x-y (PO4) 3 NASICON Series". In: *Chemistry of materials* 15.9 (2003), pp. 1879–1885.
- [53] Kenji Homma et al. "Crystal structure and phase transitions of the lithium ionic conductor Li3PS4". In: *Solid State Ionics* 182.1 (2011), pp. 53–58.
- [54] Noriaki Kamaya et al. "A lithium superionic conductor". In: *Nature materials* 10.9 (2011), pp. 682–686.
- [55] Masahiro Murayama et al. "Synthesis of new lithium ionic conductor thio-LISICON—lithium silicon sulfides system". In: *Journal of Solid State Chemistry* 168.1 (2002), pp. 140–148.
- [56] Subin Song et al. "Material Search for a Li10GeP2S12-Type Solid Electrolyte in the Li-P-S-X (X= Br, I) System via Clarification of the Composition–Structure–Property Relationships". In: *Chemistry of Materials* 34.18 (2022), pp. 8237–8247.
- [57] Yongheum Lee et al. "Lithium argyrodite sulfide electrolytes with high ionic conductivity and air stability for all-solid-state Li-ion batteries". In: ACS Energy Letters 7.1 (2021), pp. 171–179.
- [58] Wei Xia et al. "Antiperovskite electrolytes for solid-state batteries". In: *Chemical reviews* 122.3 (2022), pp. 3763–3819.
- [59] Ajay Gautam et al. "Rapid crystallization and kinetic freezing of site-disorder in the lithium superionic argyrodite Li6PS5Br". In: *Chemistry of Materials* 31.24 (2019), pp. 10178–10185.

[60] R Prasada Rao and S Adams. "Studies of lithium argyrodite solid electrolytes for all-solid-state batteries". In: *physica status solidi (a)* 208.8 (2011), pp. 1804–1807.

- [61] Hans-Jörg Deiseroth et al. "Li6PS5X: a class of crystalline Li-rich solids with an unusually high Li+ mobility". In: *Angewandte Chemie* 120.4 (2008), pp. 767–770.
- [62] Ajay Gautam et al. "Exploring the Relationship Between Halide Substitution, Structural Disorder, and Lithium Distribution in Lithium Argyrodites (Li6–x PS5–x Br1+ x)". In: *Chemistry of Materials* 35.19 (2023), pp. 8081–8091.
- [63] Ajay Gautam. "Structure-ionic Transport Relationship of Lithium Superionic Argyrodites". PhD thesis. Westfälische Wilhelms-Universität Münster, 2022.
- [64] Da Deng. "Li-ion batteries: basics, progress, and challenges". In: *Energy Science & Engineering* 3.5 (2015), pp. 385–418.
- [65] Abniel Machín, Carmen Morant, and Francisco Márquez. "Advancements and challenges in solid-state battery technology: An in-depth review of solid electrolytes and anode innovations". In: *Batteries* 10.1 (2024), p. 29.
- [66] Zhan Wu et al. "Interfaces in sulfide solid electrolyte-based all-solid-state lithium batteries: characterization, mechanism and strategy". In: *Electrochemical Energy Reviews* 6.1 (2023), p. 10.
- [67] Sylvain Boulineau et al. "Mechanochemical synthesis of Li-argyrodite Li6PS5X (X= Cl, Br, I) as sulfur-based solid electrolytes for all solid state batteries application". In: *Solid State Ionics* 221 (2012), pp. 1–5.
- [68] Junjun Wei et al. "Influence of annealing on ionic transfer and storage stability of Li2S–P2S5 solid electrolyte". In: *Journal of Power Sources* 294 (2015), pp. 494–500.
- [69] George F Harrington and José Santiso. "Back-to-Basics tutorial: X-ray diffraction of thin films". In: *Journal of Electroceramics* 47.4 (2021), pp. 141–163.
- [70] Hugo M Rietveld. "A profile refinement method for nuclear and magnetic structures". In: *Journal of applied Crystallography* 2.2 (1969), pp. 65–71.
- [71] Robert E Dinnebier, Andreas Leineweber, and John SO Evans. *Rietveld refinement: practical powder diffraction pattern analysis using TOPAS*. Walter de Gruyter GmbH & Co KG, 2018.
- [72] Pooja Vadhva et al. "Electrochemical impedance spectroscopy for all-solid-state batteries: theory, methods and future outlook". In: *ChemElectroChem* 8.11 (2021), pp. 1930–1947.
- [73] Marek Prochazka and Marek Prochazka. "Basics of Raman scattering (RS) spectroscopy". In: Surface-Enhanced Raman Spectroscopy: Bioanalytical, Biomolecular and Medical Applications (2016), pp. 7–19.
- [74] S. Granite. "What is Raman spectroscopy?: Raman Spectroscopy Principle, Edinburgh Instruments". In: (2023). URL: https://www.edinst.com/blog/what-is-raman-spectroscopy/.
- [75] Yu Liu et al. "Revealing the impact of Cl substitution on the crystallization behavior and interfacial stability of superionic lithium argyrodites". In: *Advanced Functional Materials* 32.47 (2022), p. 2207978.
- [76] Zhixia Zhang et al. "One-step solution process toward formation of Li6PS5Cl argyrodite solid electrolyte for all-solid-state lithium-ion batteries". In: *Journal of Alloys and Compounds* 812 (2020), p. 152103.

[77] Chuang Yu et al. "Revealing the relation between the structure, Li-ion conductivity and solid-state battery performance of the argyrodite Li 6 PS 5 Br solid electrolyte". In: *Journal of Materials Chemistry A* 5.40 (2017), pp. 21178–21188.

- [78] Rayavarapu Prasada Rao, Haomin Chen, and Stefan Adams. "Stable Lithium Ion Conducting Thiophosphate Solid Electrolytes Li x (PS4) y X z (X= Cl, Br, I)". In: *Chemistry of Materials* 31.21 (2019), pp. 8649–8662.
- [79] Dominika A Buchberger et al. "Lithium Transport Studies on Chloride-Doped Argyrodites as Electrolytes for Solid-State Batteries". In: *ACS Applied Materials & Interfaces* 15.46 (2023), pp. 53417–53428.
- [80] Shuo Wang et al. "High-conductivity argyrodite Li6PS5Cl solid electrolytes prepared via optimized sintering processes for all-solid-state lithium–sulfur batteries". In: ACS applied materials & interfaces 10.49 (2018), pp. 42279–42285.
- [81] Shuo Wang et al. "Effect of processing on structure and ionic conductivity of chlorine-rich lithium argyrodites". In: *Advanced Energy and Sustainability Research* (2023), p. 2200197.
- [82] Marvin A Kraft et al. "Inducing high ionic conductivity in the lithium superionic argyrodites Li6+ x P1–x Ge x S5I for all-solid-state batteries". In: *Journal of the American Chemical Society* 140.47 (2018), pp. 16330–16339.
- [83] Shuo Wang et al. "Facile synthesis of lithium argyrodite Li5. 5PS4. 5Br1. 5 with high ionic conductivity for all-solid-state batteries". In: *Frontiers in Chemical Engineering* 4 (2022), p. 883502.
- [84] Anshuman Dalvi, N. Parvathala Reddy, and S.C. Agarwal. "The Meyer-Neldel rule and hopping conduction". In: *Solid State Communications* 152.7 (2012), pp. 612–615. ISSN: 0038-1098. DOI: https://doi.org/10.1016/j.ssc.2012.01.018. URL: https://www.sciencedirect.com/science/article/pii/S003810981200035X.
- [85] "Structural change of Li2S-P2S5 sulfide solid electrolytes in the atmosphere". In: Solid State Ionics 182.1 (2011), pp. 116-119. ISSN: 0167-2738. DOI: https://doi.org/10.1016/j.ssi.2010.10.013. URL: https://www.sciencedirect.com/science/article/pii/S0167273810005989.
- [86] Tammo K Schwietert, Alexandros Vasileiadis, and Marnix Wagemaker. "First-principles prediction of the electrochemical stability and reaction mechanisms of solid-state electrolytes". In: *Jacs Au* 1.9 (2021), pp. 1488–1496.
- [87] Department of Chemical Engineering and Biotechnology. "Linear sweep and cyclic voltametry: The principles". In: *Department of Chemical Engineering and Biotechnology* (2013). URL: https://www.ceb.cam.ac.uk/research/groups/rg-eme/Edu/linear-sweep-and-cyclic-voltametry-the-principles.
- [88] Marnix Wagemaker et al. "Beneficial redox activity of halide solid electrolytes empowering high-performance anodes in all-solid-state batteries". In: (2024).
- [89] Tammo K Schwietert et al. "Clarifying the relationship between redox activity and electrochemical stability in solid electrolytes". In: *Nature materials* 19.4 (2020), pp. 428–435.
- [90] Ananya Banik et al. "Can substitutions affect the oxidative stability of lithium argyrodite solid electrolytes?" In: ACS applied energy materials 5.2 (2022), pp. 2045–2053.

[91] Eveline Van Der Maas et al. "Investigation of Structure, Ionic Conductivity, and Electrochemical Stability of Halogen Substitution in Solid-State Ion Conductor Li3YBr x Cl6–x". In: *The Journal of Physical Chemistry C* 127.1 (2022), pp. 125–132.

- [92] Darren HS Tan et al. "Elucidating reversible electrochemical redox of Li6PS5Cl solid electrolyte". In: *ACS Energy Letters* 4.10 (2019), pp. 2418–2427.
- [93] AL Santhosha et al. "The indium-lithium electrode in solid-state lithium-ion batteries: phase formation, redox potentials, and interface stability". In: *Batteries & Supercaps* 2.6 (2019), pp. 524–529.
- [94] Xavier Randrema et al. "A detailed characterisation study of Li6PS5Cl ionic conductors from several synthetic routes". In: *Solid state sciences* 118 (2021), p. 106681.



## Supplementary information -Halide rich lithium argyrodite synthesis and performance

## A.1. Reitveld refined XRD patterns

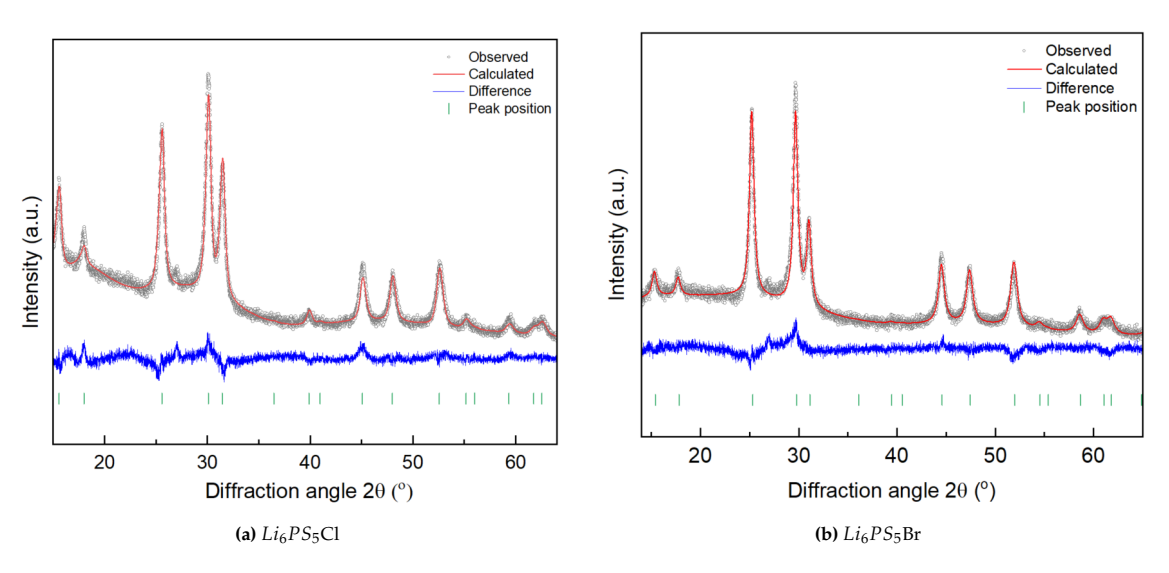


**Figure A.1:** Refined XRD pattern of  $Li_6PS_5Cl$  and  $Li_6PS_5Br$ 

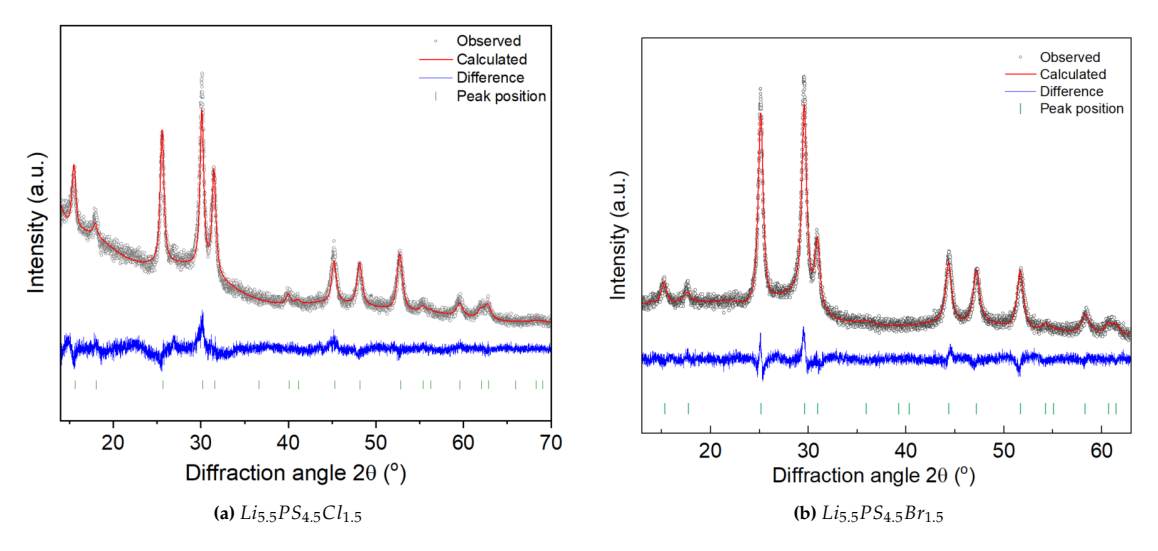


**Figure A.2:** Refined XRD pattern of  $Li_{5.5}PS_{4.5}Cl_{1.5}$  and  $Li_{5.5}PS_{4.5}Br_{1.5}$ 

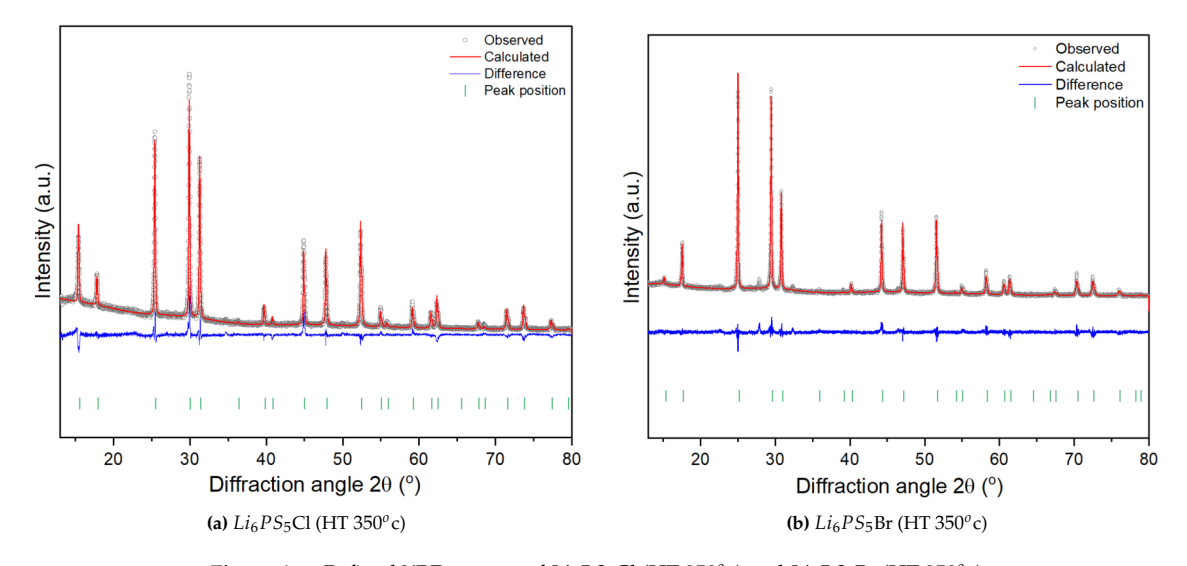


**Figure A.3:** Refined XRD pattern of  $Li_6PS_5Cl$  (HT 350°c) and  $Li_6PS_5Br$  (HT 350°c)

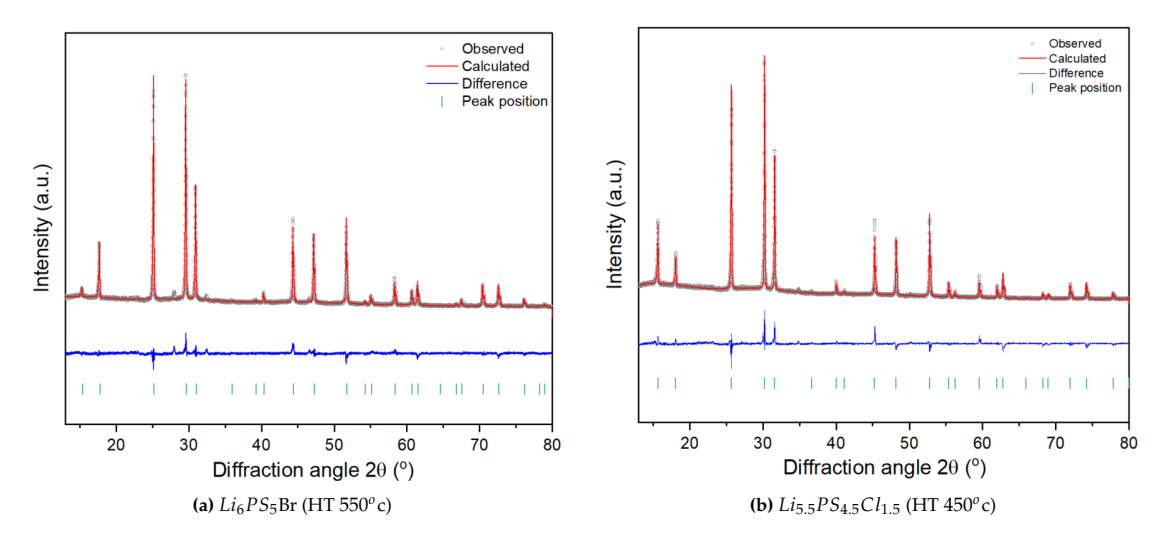


**Figure A.4:** Refined XRD pattern of  $Li_6PS_5C1$  (HT 350°c) and  $Li_6PS_5Br$  (HT 350°c)

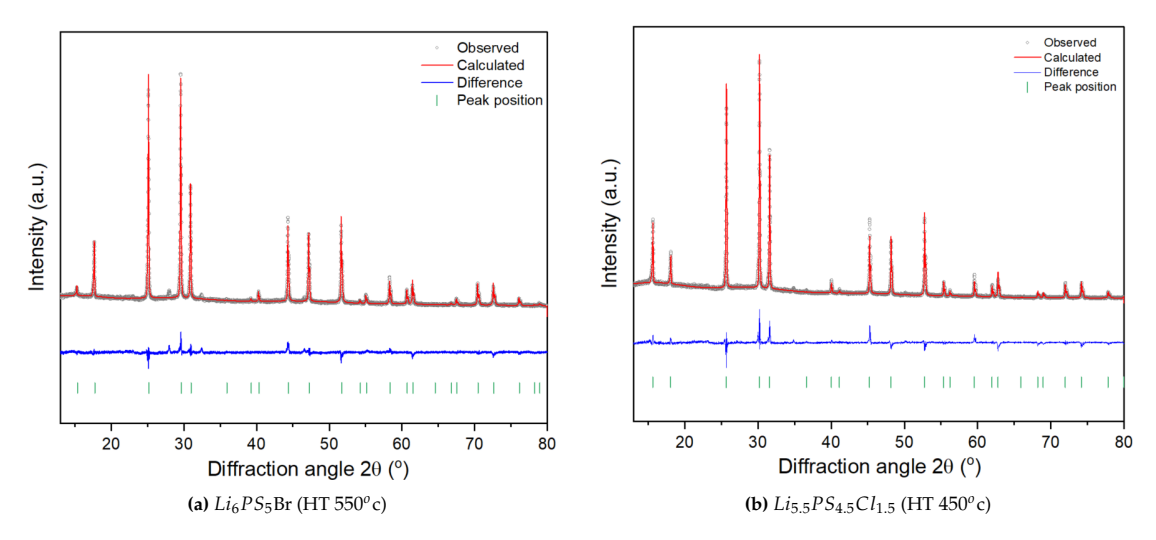


**Figure A.5:** Refined XRD pattern of  $Li_6PS_5$ Br (HT 550°c) and  $Li_6PS_5$ Br (HT 350°c)

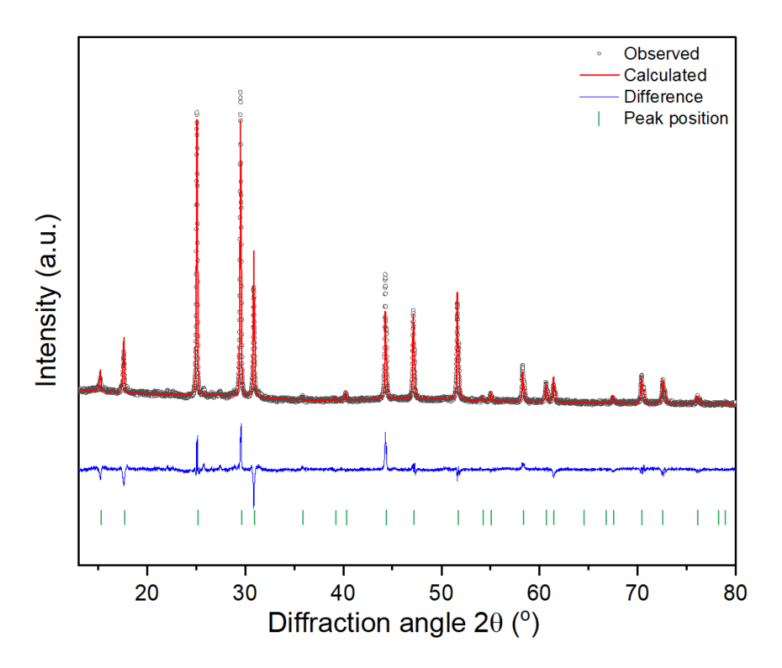


**Figure A.6:** Refined XRD pattern of  $Li_{5.5}PS_{4.5}Br_{1.5}$ (HT  $450^{\circ}$ c)

$Li_6PS_5$	<i>Li</i> <sub>6</sub> <i>PS</i> <sub>5</sub> <i>Cl</i> (BM) structure from X-ray diffraction data (space group F-43m)							
$\lambda_1 = 1.5$	406 Å							
a = 9.84	$423; \alpha = \beta = \gamma =$	$= (90^{\circ}); V_{\bullet}$	olume = 9	53.43				
Fit resi	duals ( $R_{wp}$ , $R_{ex}$	p): 5.742,	3.929					
Atom								
Li1	48h	0.3044	0.0253	0.6956	0.437	5		
Li2	24g	0.25 0.009 0.75 0.158 5						
Cl1	4a	1	1	1	0.3559	5.4203		
Cl2	4d	0.75	0.75	0.75	0.6440	5		
P1	4b	1	0.5	1	1	5		
S1	4d 0.1222 -0.1222 0.6222 1 5							
S2	16e 1 1 1 0.6440 5.4203							
S3	4a	0.75	0.75	0.75	0.3559	5		

**Table A.1:** Crystallographic information of  $Li_6PS_5Cl$  (BM)

 $Li_6PS_5Br$  (BM) structure from X-ray diffraction data (space group F-43m)  $\lambda_1$ = 1.5406 Å

a = 9.9458;  $\alpha = \beta = \gamma = (90^{\circ})$ ; Volume = 983.85

Fit residuals ( $R_{wp}$ ,  $R_{exp}$ ): 5.742, 3.929

Atom	Wyckoff Site	x/a	y/b	z/c	Occ.	beq
Li1	48h	0.3044	0.0253	0.6956	0.437	5
Li2	24g	0.25	0.009	0.75	0.158	5
Br1	4a	1	1	1	0.5479	3.3329
Br2	4d	0.75	0.75	0.75	0.4520	0.1637
P1	4b	1	0.5	1	1	0.0208
S1	4d	0.1195	0.1195	0.6195	1	0.03192
S2	16e	1	1	1	0.4520	3.3329
S3	4a	0.75	0.75	0.75	0.5479	0.1637

**Table A.2:** Crystallographic information of *Li*<sub>6</sub>*PS*<sub>5</sub>*Br* (BM)

 $Li_{5.5}PS_{4.5}Cl_{1.5}$  (BM) structure from X-ray diffraction data (space group F-43m)  $\lambda_1$ = 1.5406 Å

a=9.8025;  $\alpha = \beta = \gamma = (90^{\circ})$ ; Volume = 941.92

Fit residuals ( $R_{wp}$ ,  $R_{exp}$ ): 6.161, 4.701

	( 10 p ) est	<i>'</i>				
Atom	Wyckoff Site	x/a	y/b	z/c	Occ.	beq
Li1	48h	0.3044	0.0253	0.6956	0.437	5
Li2	24g	0.25	0.009	0.75	0.158	5
Cl1	4a	1	1	1	0.700	0.2867
Cl2	4d	0.75	0.75	0.75	0.800	1
P1	4b	1	0.5	1	1	2.0361
S1	4d	0.1242	0.1242	0.6242	0.298	2.1043
S2	16e	1	1	1	0.300	0.2867
S3	4a	0.75	0.75	0.75	1	1

**Table A.3:** Crystallographic information of  $Li_{5,5}PS_{4,5}Cl_{1,5}$  (BM)

<u>S1</u>

S2

S3

4d

16e

4a

 $Li_{5.5}PS_{4.5}Br_{1.5}$  (BM) structure from X-ray diffraction data (space group F-43m)  $\lambda_1 = 1.5046 \text{ Å}$ a = 10.0008;  $\alpha = \beta = \gamma = (90^{\circ})$ ; Volume = 1000.260 Fit residuals ( $R_{wp}$ ,  $R_{exp}$ ): 3.6053, 2.8483 Wyckoff Site Atom x/a y/b z/cOcc. beq Li1 48h 0.3044 0.0253 0.6956 0.437 5 Li2 5 24g 0.25 0.009 0.75 0.158 Br1 1 1 1 0.700 0.2867 4a Br2 0.75 0.800 1 4d 0.75 0.75 P1 4b 1 0.5 1 1 0.0208

**Table A.4:** Crystallographic information of *Li*<sub>5.5</sub>*PS*<sub>4.5</sub>*Br*<sub>1.5</sub> (BM)

0.6204

1

0.75

1

0.300

0.200

0.0319

0.2867

1

0.1204

1

0.75

 $Li_6PS_5Cl$  (HT 350°c) structure from X-ray diffraction data (space group F-43m)  $\lambda_1 = 1.5046 \text{ Å}$ 

a = 9.8539;  $\alpha = \beta = \gamma = (90^{\circ})$ ; Volume = 956.827

0.1204

1

0.75

Fit residuals ( $R_{wp}$ ,  $R_{exp}$ ): 8.6452, 4.4761

1101001	(1000000000000000000000000000000000000					
Atom	Wyckoff Site	x/a	y/b	z/c	Occ.	beq
Li1	48h	0.3044	0.0253	0.6956	0.437	5
Li2	24g	0.25	0.009	0.75	0.158	5
Cl1	4a	1	1	1	0.678	0.845
Cl2	4d	0.75	0.75	0.75	0.321	0.2669
P1	4b	1	0.5	1	1	0.0208
S1	4d	0.1237	0.1237	0.6234	0.678	0.0319
S2	16e	1	1	1	1	0.845
S3	4a	0.75	0.75	0.75	0.321	0.2669

**Table A.5:** Crystallographic information of *Li*<sub>6</sub>*PS*<sub>5</sub>*Cl* (HT 350°c)

 $Li_6PS_5Br$  (HT 350°c) structure from X-ray diffraction data (space group F-43m)  $\lambda_1 = 1.5046 \text{ Å}$ 

a = 9.9914;  $\alpha = \beta = \gamma = (90^{\circ})$ ; Volume = 997.429

Fit residuals ( $R_{wp}$ ,  $R_{exp}$ ): 4.9770, 3.1073

	( wp/ cx	P /	<u> </u>			
Atom	Wyckoff Site	x/a	y/b	z/c	Occ.	beq
Li1	48h	0.3044	0.0253	0.6956	0.437	5
Li2	24g	0.25	0.009	0.75	0.158	5
Br1	4a	1	1	1	0.777	1.335
Br2	4d	0.75	0.75	0.75	0.222	1.207
P1	4b	1	0.5	1	1	0.0208
S1	4d	0.1198	0.1198	0.6198	1	0.0319
S2	16e	1	1	1	0.222	1.335
S3	4a	0.75	0.75	0.75	0.777	1.207

**Table A.6:** Crystallographic information of  $Li_6PS_5Br$  (HT 350°c)

 $Li_{5.5}PS_{4.5}Cl_{1.5}$  (HT 350°c) structure from X-ray diffraction data (space group F-43m)  $\lambda_1 = 1.5046$  Å

a = 9.865;  $\alpha = \beta = \gamma = (90^{\circ})$ ; Volume = 960.044

Fit residuals ( $R_{wp}$ ,  $R_{exp}$ ): 6.7002, 4.2630

Atom	Wyckoff Site	x/a	y/b	z/c	Occ.	beq
Li1	48h	0.3044	0.0253	0.6956	0.437	0.064
Li2	24g	0.25	0.009	0.75	0.158	0.027
Cl1	4a	1	1	1	0.64	0.0423
Cl2	4d	0.75	0.75	0.75	0.56	0.0281
P1	4b	1	0.5	1	1	0.0208
S1	4d	0.1198	0.1198	0.6198	1	0.0319
S2	16e	1	1	1	0.56	0.0423
S3	4a	0.75	0.75	0.75	0.64	0.0281

**Table A.7:** Crystallographic information of  $Li_{5.5}PS_{4.5}Cl_{1.5}$  (HT 350°c)

 $Li_{5.5}PS_{4.5}Br_{1.5}$  (HT 350°c) structure from X-ray diffraction data (space group F-43m)  $\lambda_1 = 1.5046 \text{ Å}$ 

a = 9.9835;  $\alpha = \beta = \gamma = (90^{\circ})$ ; Volume = 995.072

Fit residuals ( $R_{wp}$ ,  $R_{exp}$ ): 4.0740, 2.6999

Atom	Wyckoff Site	x/a	y/b	z/c	Occ.	beq
Li1	48h	0.3044	0.0253	0.6956	0.437	5
Li2	24g	0.25	0.009	0.75	0.158	5
Br1	4a	1	1	1	0.875	2.465
Br2	4d	0.75	0.75	0.75	0.669	2.343
P1	4b	1	0.5	1	1	0.0208
S1	4d	0.1198	0.1198	0.6198	1	0.0319
S2	16e	1	1	1	0.0326	2.465
S3	4a	0.75	0.75	0.75	0.3102	2.343

**Table A.8:** Crystallographic information of  $Li_{5.5}PS_{4.5}Br_{1.5}$  (HT 350°c)

 $Li_{5.5}PS_{4.5}Cl_{1.5}$  (HT 450°c) structure from X-ray diffraction data (space group F-43m)  $\lambda_1 = 1.5046 \text{ Å}$ 

a = 9.8108;  $\alpha = \beta = \gamma = (90^{\circ})$ ; Volume = 944.319 Fit residuals ( $R_{wv}$ ,  $R_{exv}$ ): 7.8165, 3.8987

1101001	110 1001010110 (11 wp) 11 (2xp) 11 (0.000)						
Atom	Wyckoff Site	x/a	y/b	z/c	Occ.	beq	
Li1	48h	0.3044	0.0253	0.6956	0.437	5	
Li2	24g	0.25	0.009	0.75	0.158	5	
Cl1	4a	0	0	1	0.669	1.99	
Cl2	4d	0.25	0.25	0.75	0.830	3.118	
P1	4b	1	0.5	1	1	0.0208	
S1	4d	0.25	0.25	0.75	0.169	0.0319	
S2	16e	0.119	0.119	0.619	0.3308	1.99	
S3	4a	0	0	1	1	3.11	

**Table A.9:** Crystallographic information of  $Li_{5.5}PS_{4.5}Cl_{1.5}$  (HT 450°c)

 $Li_{5.5}PS_{4.5}Br_{1.5}$  (HT 450°c) structure from X-ray diffraction data (space group F-43m)  $\lambda_1 = 1.5046 \text{ Å}$ 

a = 9.987;  $\alpha = \beta = \gamma = (90^{\circ})$ ; Volume = 996.333

Fit residuals ( $R_{wp}$ ,  $R_{exp}$ ): 5.1060, 3.1021

Atom	Wyckoff Site	x/a	y/b	z/c	Occ.	beq
Li1	48h	0.3044	0.0253	0.6956	0.437	5
Li2	24g	0.25	0.009	0.75	0.158	5
Br1	4a	1	1	1	0.891	1.011
Br2	4d	0.75	0.75	0.75	0.5245	0.777
P1	4b	1	0.5	1	1	0.0208
S1	4d	0.1205	0.1205	0.6205	1	0.0319
S2	16e	1	1	1	0.1083	1.011
S3	4a	0.75	0.75	0.75	0.4754	0.777

**Table A.10:** Crystallographic information of  $Li_{5.5}PS_{4.5}Br_{1.5}$  (HT 450°c)

 $Li_6PS_5Cl$  (HT 550°c) structure from X-ray diffraction data (space group F-43m)

 $\lambda_1 = 1.5046 \text{ Å}$ 

a = 9.8621;  $\alpha = \beta = \gamma = (90^{\circ})$ ; Volume = 959.218

Fit residuals ( $R_{wp}$ ,  $R_{exp}$ ): 10.1478, 4.3829

1101001	21 010113 (11 wp) 11 ex	p): = = ::	0, 1100_			
Atom	Wyckoff Site	x/a	y/b	z/c	Occ.	beq
Li1	48h	0.3044	0.0253	0.6956	0.437	5
Li2	24g	0.25	0.009	0.75	0.158	5
Cl1	4a	1	1	1	0.5838	0.6466
Cl2	4d	0.75	0.75	0.75	0.4161	0.7203
P1	4b	1	0.5	1	1	0.0208
S1	4d	0.1210	0.1210	0.6210	0.654	0.0319
S2	16e	1	1	1	0.2501	0.640
S3	4a	0.75	0.75	0.75	0.345	0.7203

**Table A.11:** Crystallographic information of *Li*<sub>6</sub>*PS*<sub>5</sub>*Cl* (HT 550°c)

A.2. SEM Images 75

$Li_6PS_5$	$Li_6PS_5Br$ (HT 550°c) structure from X-ray diffraction data (space group F-43m)							
$\lambda_1 = 1.5$	5046 Å							
a = 9.99	$a = 9.9906$ ; $\alpha = \beta = \gamma = (90^{\circ})$ ; Volume = 997.187							
Fit resi	duals ( $R_{wp}$ , $R_{ex}$	p): 4.8495	5, 2.8052					
Atom	Wyckoff Site		y/b	z/c	Occ.	beq		
Li1	48h	0.3044	0.0253	0.6956	0.437	5		
Li2	24g	0.25	0.009	0.75	0.158	5		
Br1	4a	1	1	1	0.795	2.159		
Br2	4d	0.75	0.75	0.75	0.2046	1.925		
P1	4b	1	0.5	1	1	0.0208		
S1	4d	0.1192	0.1192	0.6192	1	0.0319		
S2	16e	1	1	1	0.204	2.159		
S3	4a	0.75	0.75	0.75	0.795	1.925		

**Table A.12:** Crystallographic information of *Li*<sub>6</sub>*PS*<sub>5</sub>*Br* (HT 550°C)

## A.2. SEM Images

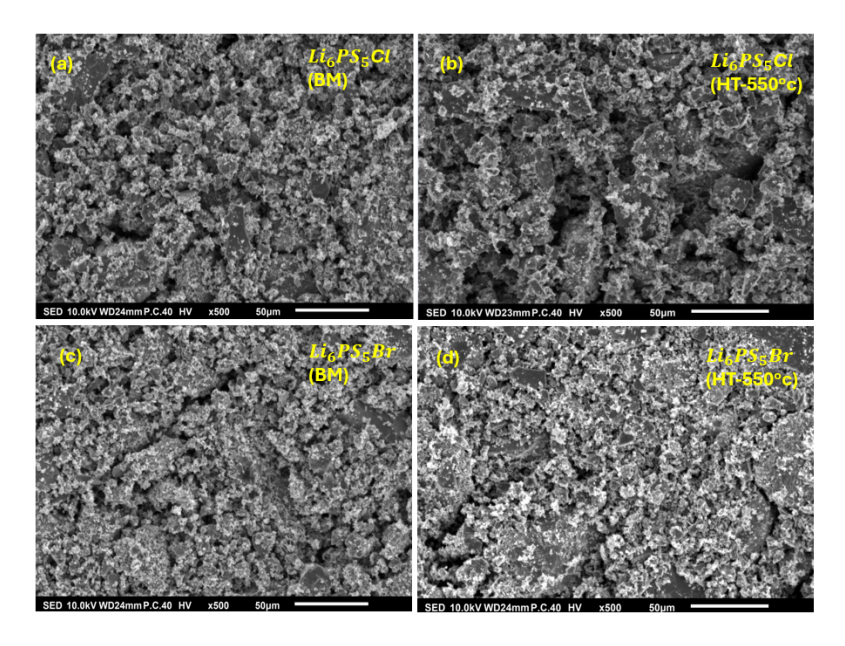


**Figure A.7:** SEM images of (a)  $Li_6PS_5$ Cl(BM), (b)  $Li_6PS_5$ Cl(HT 550°C), (c)  $Li_6PS_5$ Br(BM), and (d)  $Li_6PS_5$ Br(HT 550°C) solid electrolyte was prepared by high energy ball milling and high temperature annealing in 50 $\mu$  m

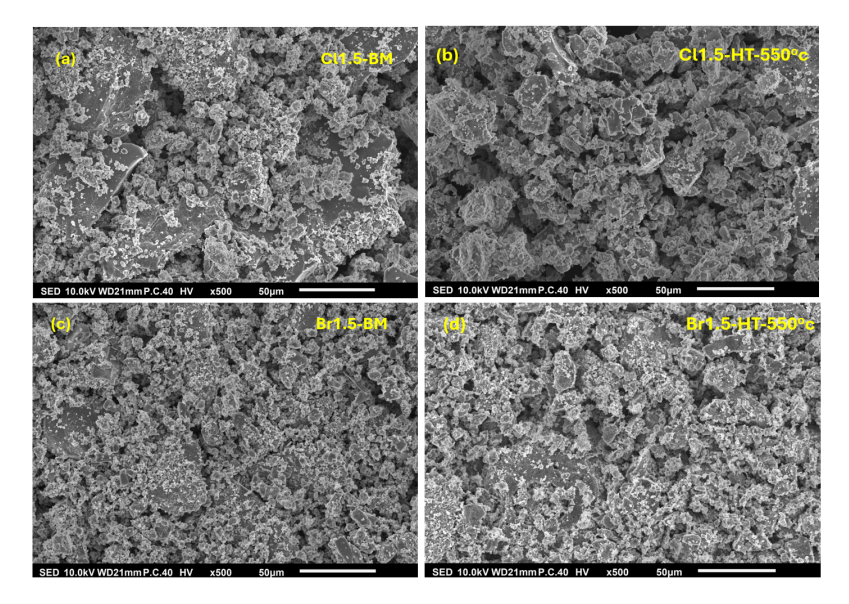


Figure A.8: SEM images of (a) $Li_{5.5}PS_{4.5}Cl_{1.5}$  (BM), (b) $Li_{5.5}PS_{4.5}Cl_{1.5}$  (HT 450°C), (c) $Li_{5.5}PS_{4.5}Br_{1.5}$  (BM), and (d) $Li_{5.5}PS_{4.5}Br_{1.5}$  (HT 450°C) solid electrolyte was prepared by high energy ball milling and high temperature annealing in  $50\mu$  m

## A.3. Ionic conductivity and Individual EIS fitted plots

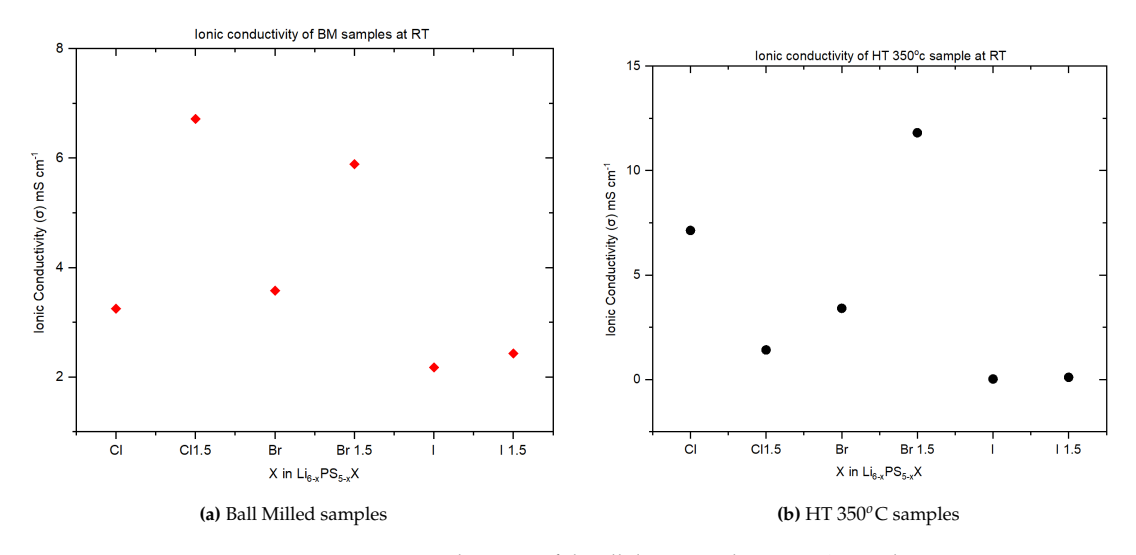
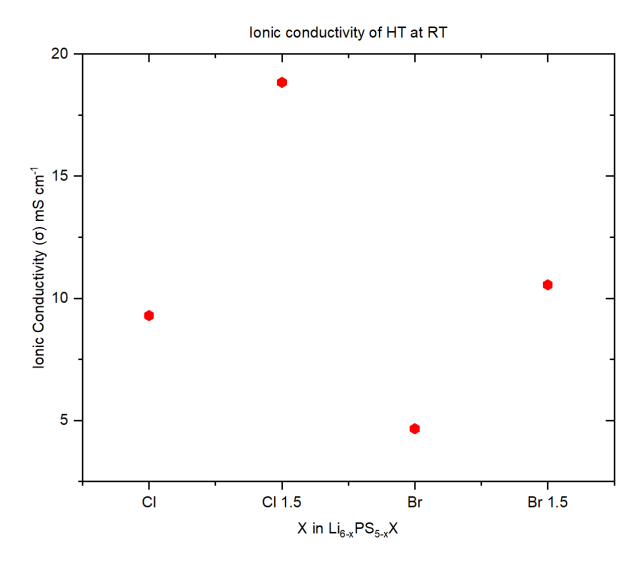


Figure A.9: Ionic conductivity of the all the BM and HT  $350^{\circ}$ C samples



**Figure A.10:** Ionic conductivity of the all the HT samples at  $450^{\circ}$ C and  $550^{\circ}$ C including the  $Li_6PS_5$ I and  $Li_{5.5}PS_{4.5}I_{1.5}$  measured at room temperature (298 K)

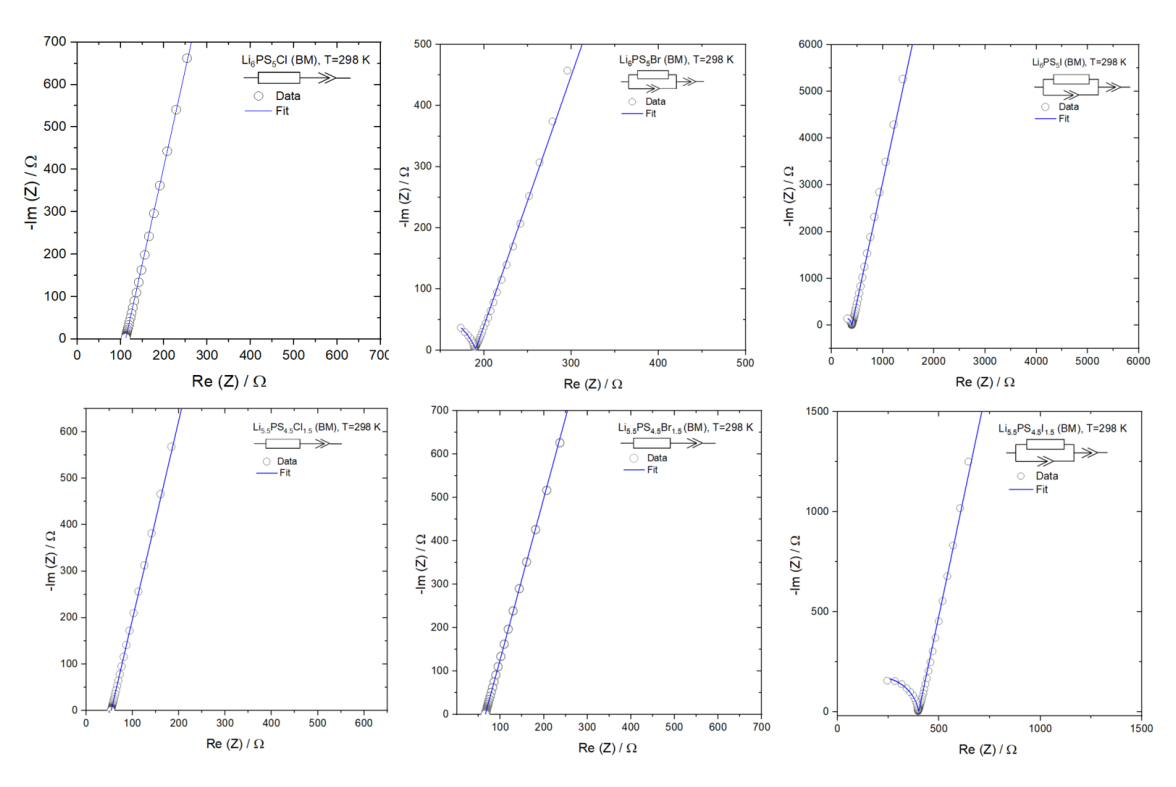
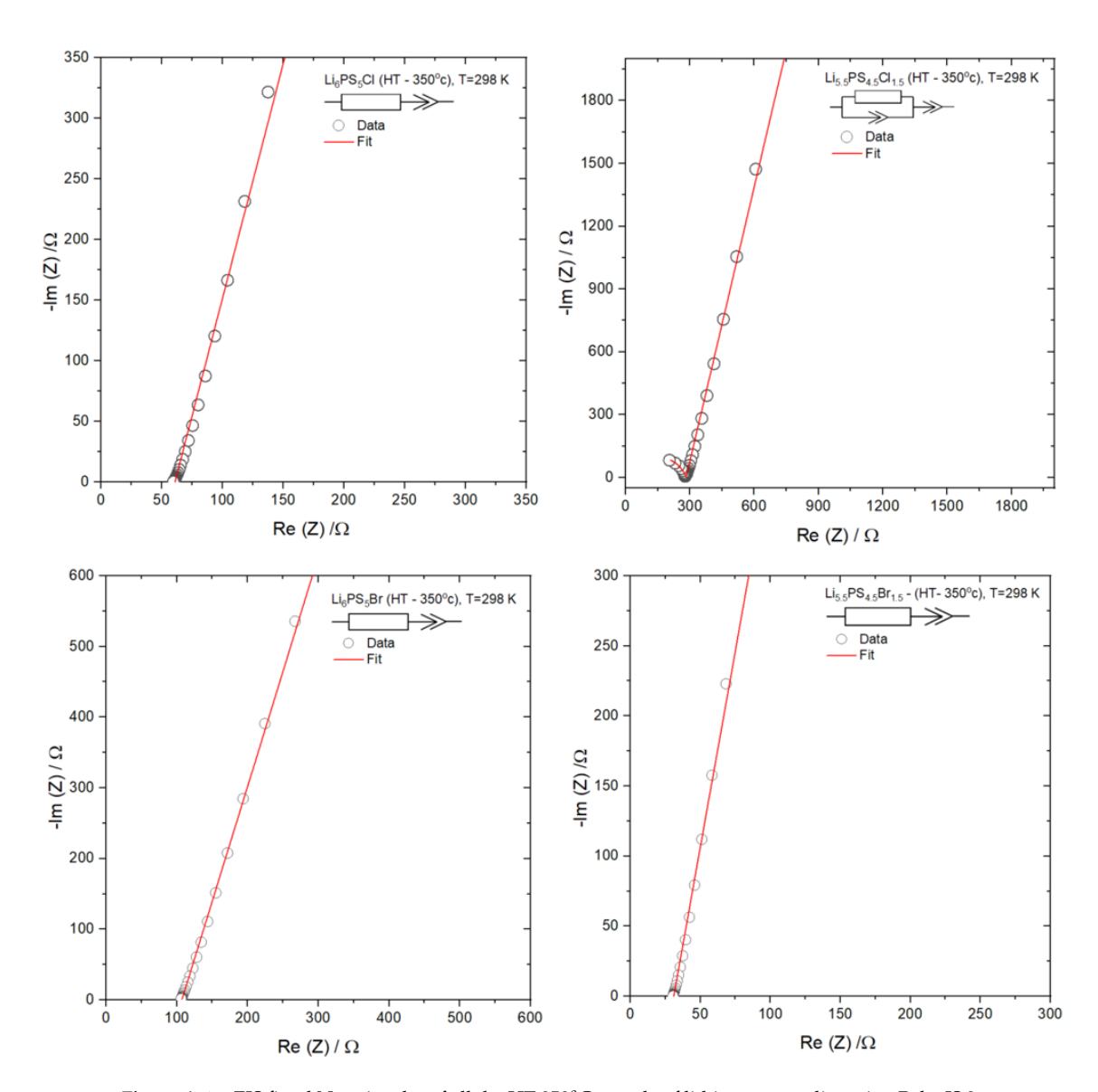
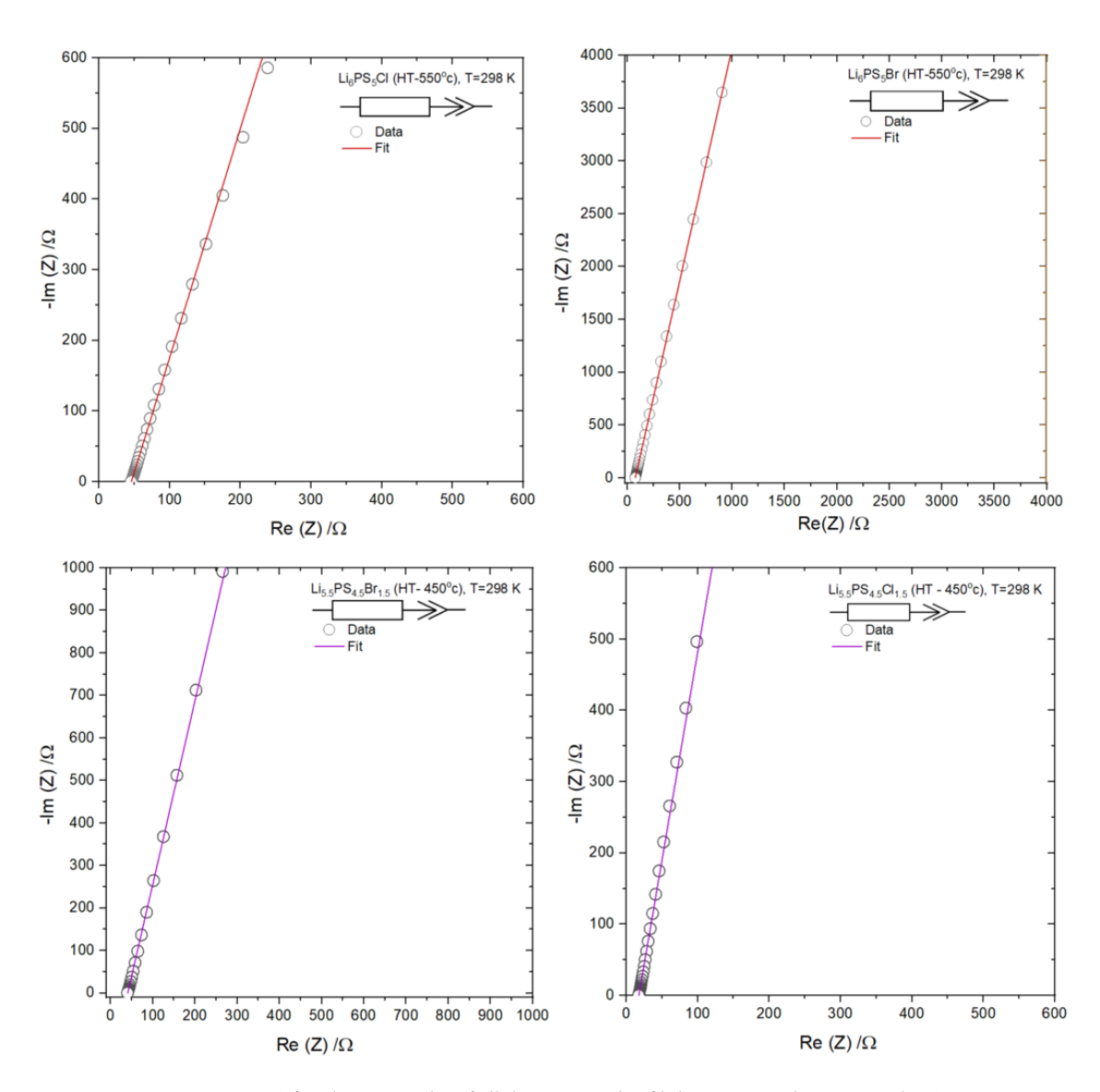


Figure A.11: EIS fitted Nyquist plot of all the BM sample of lithium argyrodite using RelaxIS 3



 $\textbf{Figure A.12:} \ EIS \ fitted \ Nyquist \ plot \ of \ all \ the \ HT \ 350^{o}C \ sample \ of \ lithium \ argyrodite \ using \ RelaxIS \ 3$ 



 $\textbf{Figure A.13:} \ EIS \ fitted \ Nyquist \ plot \ of \ all \ the \ HT \ sample \ of \ lithium \ argyrodite \ using \ RelaxIS \ 3$ 

## A.4. Temperature dependent EIS and the Activation Energy

### A.4.1. Arrhenius plot of all BM samples

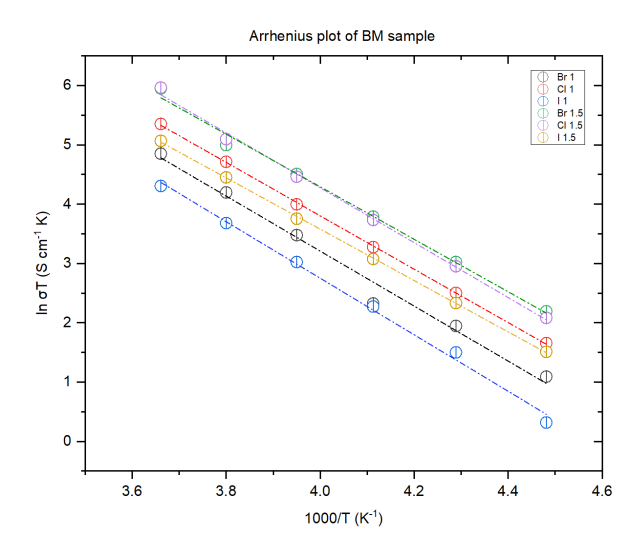


**Figure A.14:** Arrhenius plot of the all the ball milled samples including the  $Li_6PS_5I$  and  $Li_{5.5}PS_{4.5}I_{1.5}$  measured from temperature ranging from  $0^oc$  to  $-50^oc$ 

### A.4.2. Pre-exponential factor

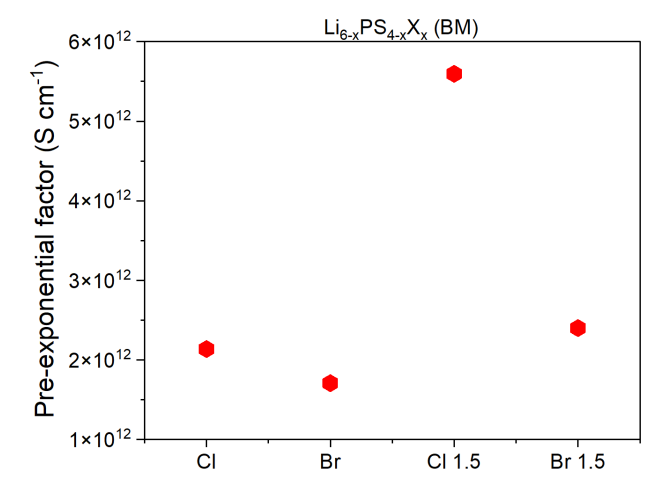


Figure A.15: Pre-exponential factor of all the ball milled samples

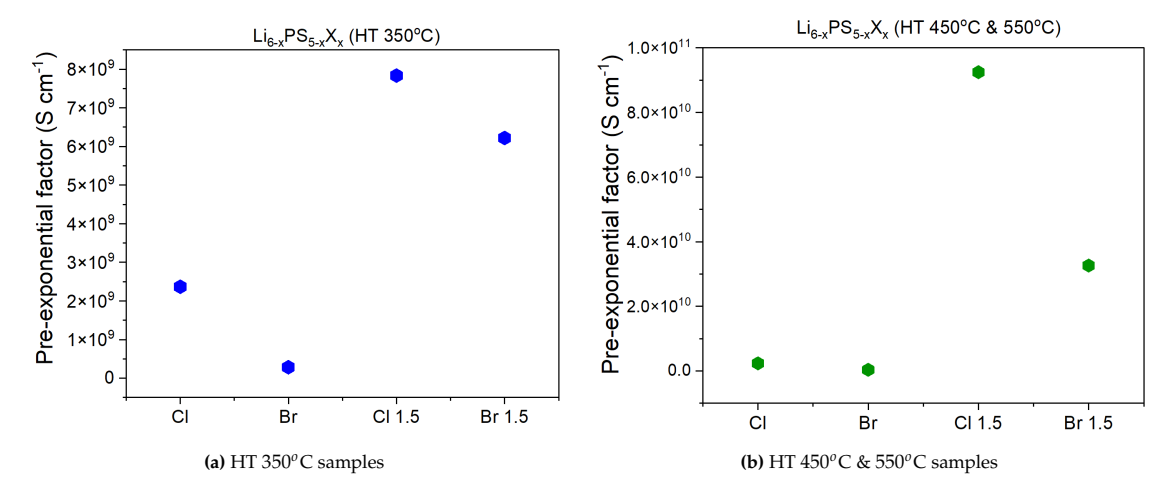
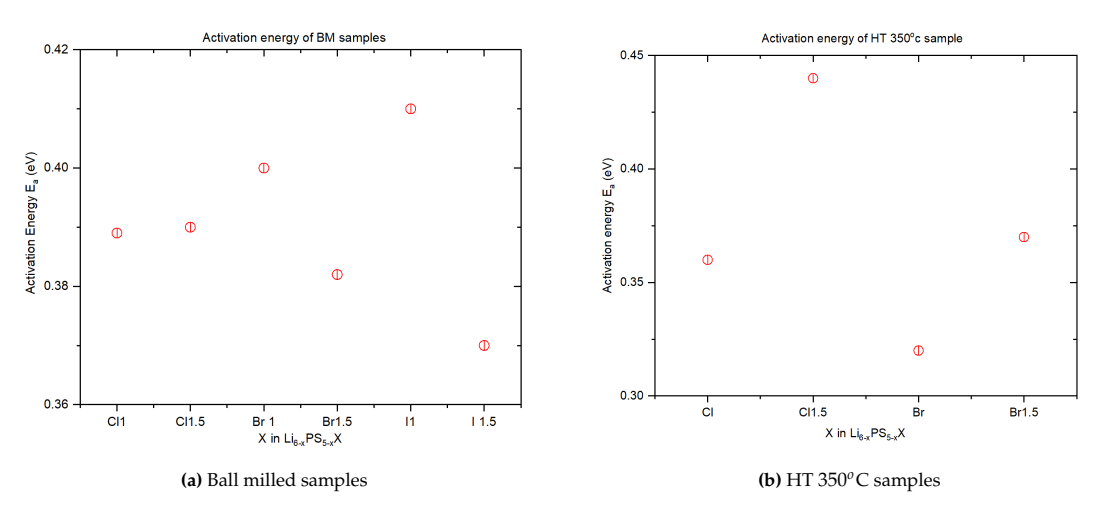


Figure A.16: Pre-exponential factor of the heat treated samples

#### A.4.3. Activation energy results



**Figure A.17:** Activation energy of BM and HT 350°C

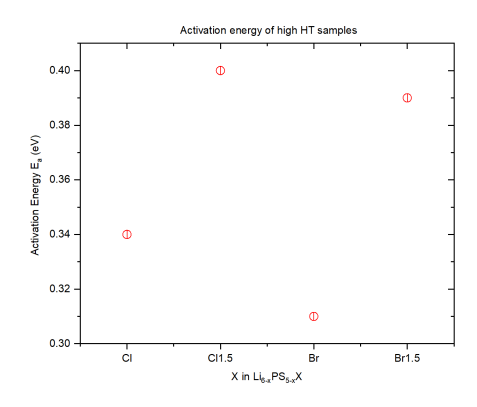
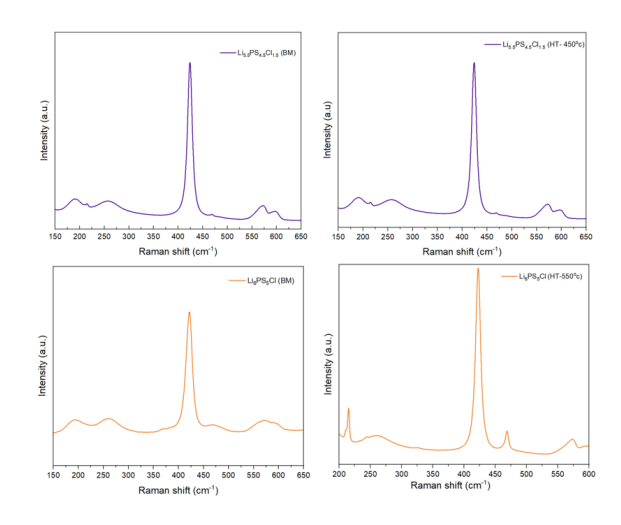


Figure A.18: Activation energy of all the HT samples

## A.5. Raman Spectroscopy

## A.5.1. Raman spectra of $Li_6PS_5Cl$ and $Li_6PS_5Br$



**Figure A.19:** Raman spectra of BM and HT samples of  $Li_6PS_5Cl$  and  $Li_6PS_5Br$  showing the peaks of  $PS_4^{-3}$ 

#### **A.5.2.** Raman spectra of $Li_{5.5}PS_{4.5}Cl_{1.5}$ and $Li_{5.5}PS_{4.5}Br_{1.5}$

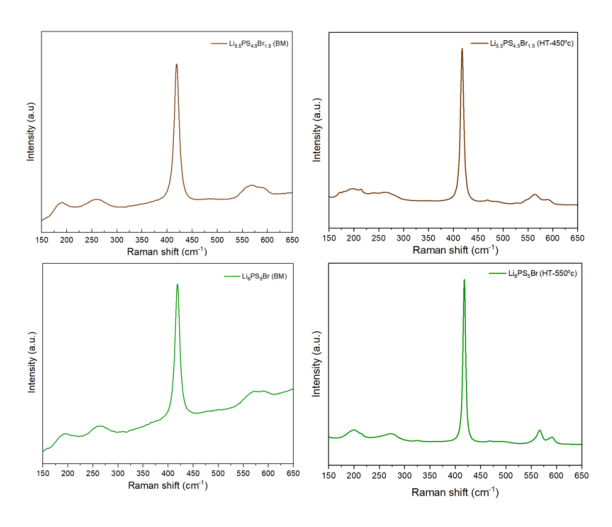


Figure A.20: Raman spectra of BM and HT samples of  $Li_{5.5}PS_{4.5}Cl_{1.5}$  and  $Li_{5.5}PS_{4.5}Br_{1.5}$  showing the peaks of  $PS_4^{-3}$ 

## A.5.3. Electrochemical stability window of the Bromine rich and $LN_2$ Quenched and slow cooled

#### XRD patterns of the bromine enriched lithium argyrodite

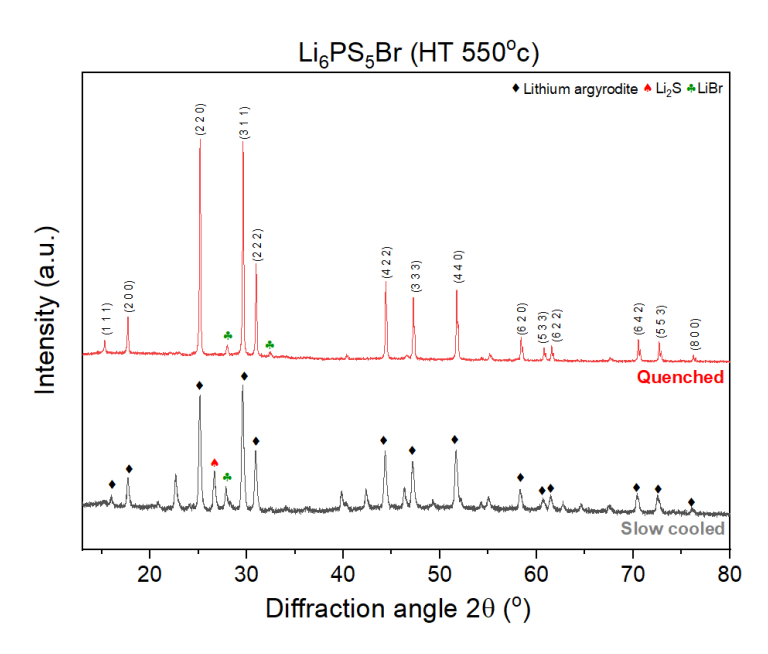


Figure A.21: XRD pattern of both slow cooled and quenched samples showing the peaks of lithium argyrodite structure of  $Li_6PS_5Br$  HT  $550^{\rm o}C$ 

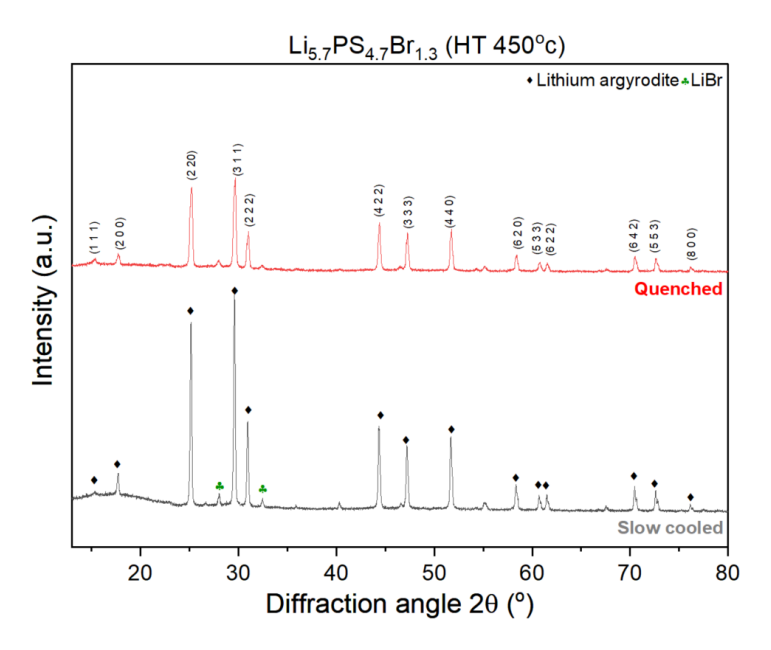


Figure A.22: XRD pattern of both slow cooled and quenched samples showing the peaks of lithium argyrodite structure of  $Li_{5.7}PS_{4.7}Br_{1.3}$  HT  $450^{o}$ C

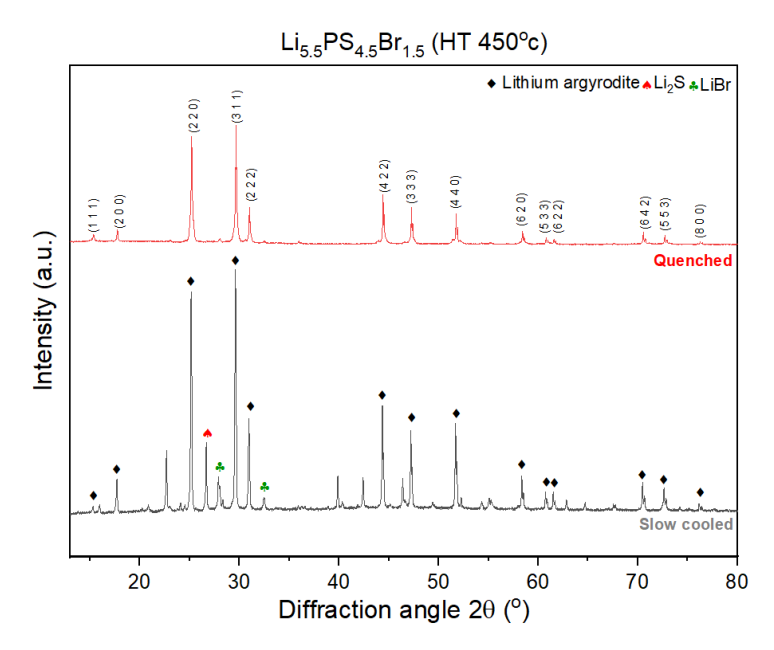


Figure A.23: XRD pattern of both slow cooled and quenched samples showing the peaks of lithium argyrodite structure of  $Li_{5.5}PS_{4.5}Br_{1.5}$  HT  $450^{o}$ C

#### Electrochemical stability window of the liquid nitrogen quenched composition

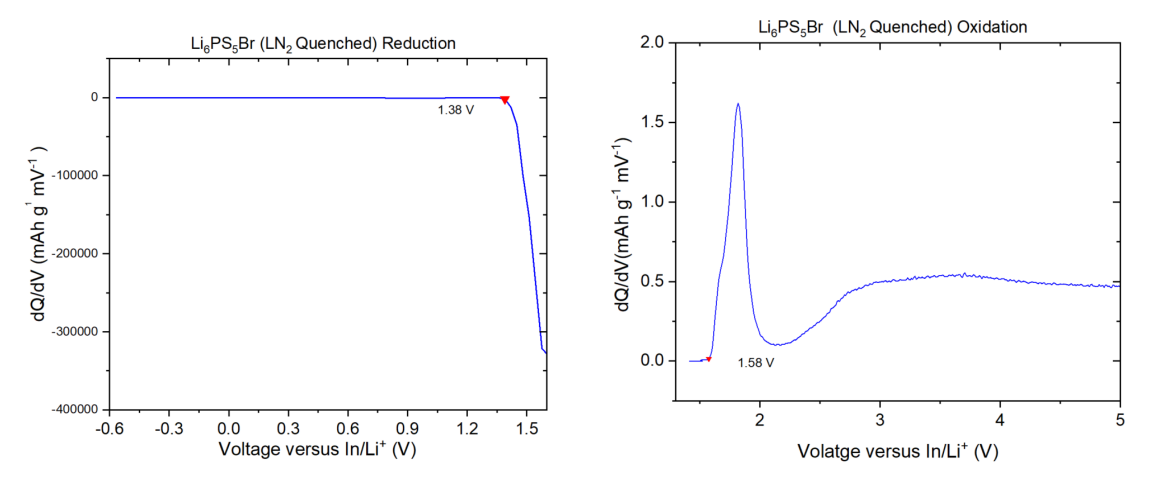


Figure A.24: Electrochemical stability window representing the oxidation and the reduction of  $Li_6PS_5Br$  HT  $550^{o}$  c  $LN_2$  Quenched samples

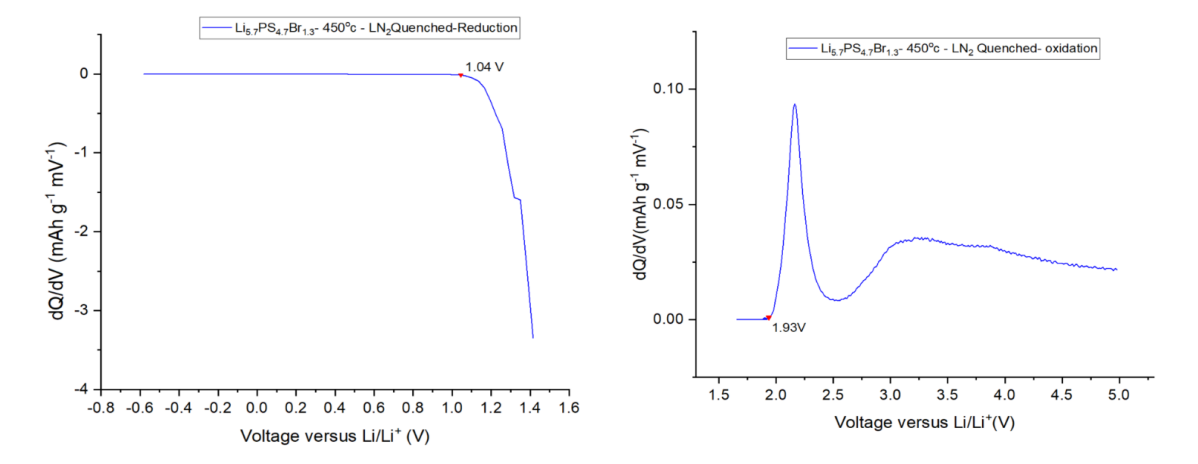
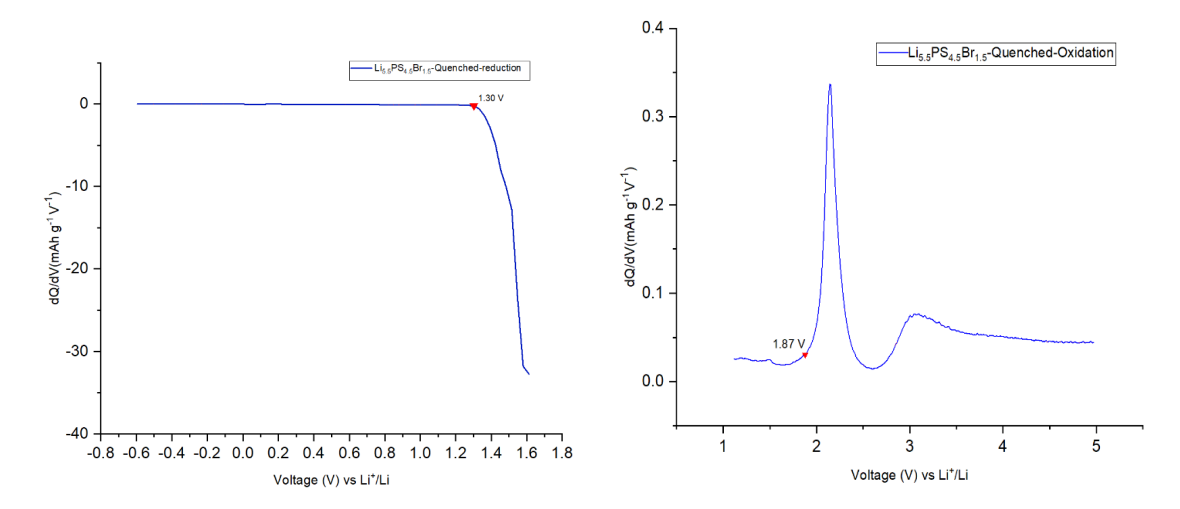


Figure A.25: Electrochemical stability window representing the oxidation and the reduction of  $Li_{5.7}PS_{4.7}Br_{1.3}$  HT  $450^{o}$ c  $LN_{2}$  Slow cooled samples



**Figure A.26:** Electrochemical stability window representing the oxidation and the reduction of  $Li_{5.5}PS_{4.5}Br_{1.5}$  HT  $450^{\circ}c$   $LN_2$  Slow cooled samples

Composition	Reduction	Oxidation
Br Q	1.96	2.18
Br 1.3 Q	1.64	2.53
Br 1.5 Q	1.9	2.47

Table A.13: Actual electrochemical stability window of the LPSB quenched samples

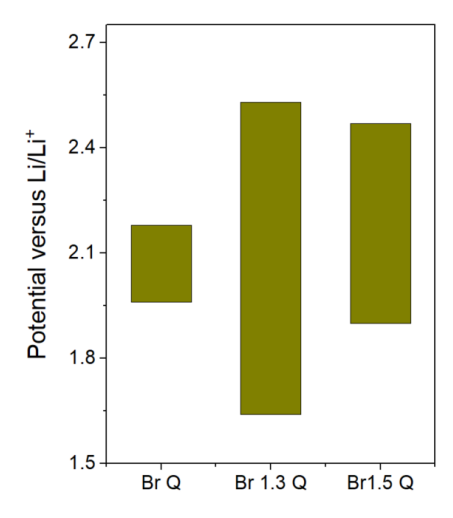


Figure A.27: Electrochemical stability window of  $LN_2$  cooled bromine enriched lithium argyrodite

# B

# Appendix: Sodium-ion solid electrolyte

#### **B.1. Sodium solid electrolyte**

This part of the thesis describes the investigation of the synthesis and characterization of the sodium solid electrolyte with halide substitution using high-energy ball milling. Various combinations and proportions of precursors were explored to find the optimum sodium solid electrolyte with high ionic conductivity. The sections below (B.1.1, B.1.2, and B.1.3) further discuss the synthesis and characterization, including XRD and ionic conductivity of various compositions.

#### **B.1.1.** Synthesis and XRD patterns of $Na_{2+x}In_xHf_{1-x}Cl_6$

By using NaCl,  $InCl_3$ , and  $HfCl_4$  as precursor to synthesis the  $Na_{2+x}In_xHf_{1-x}Cl_6$  with (x=0, 0.25, 0.5, 0.75, and 1) The mixture was placed inside a 45 ml  $ZrO_2$  jar with a milling media ratio of 1:30 and 10 mm (weight = 3 g) balls. The milling was set at 550 rpm with 15 minutes running and 10 minutes pause cycles, repeated for 60 cycles to synthesize 1 g of solid electrolyte. The figure B.1 (a) shows the XRD patterns of the composition  $Na_{2+x}In_xHf_{1-x}Cl_6$  with (X = 0, 0.25, 0.5. 0.75, 1) and their ionic conductivity is shown in the figure B.1(b), respectively.

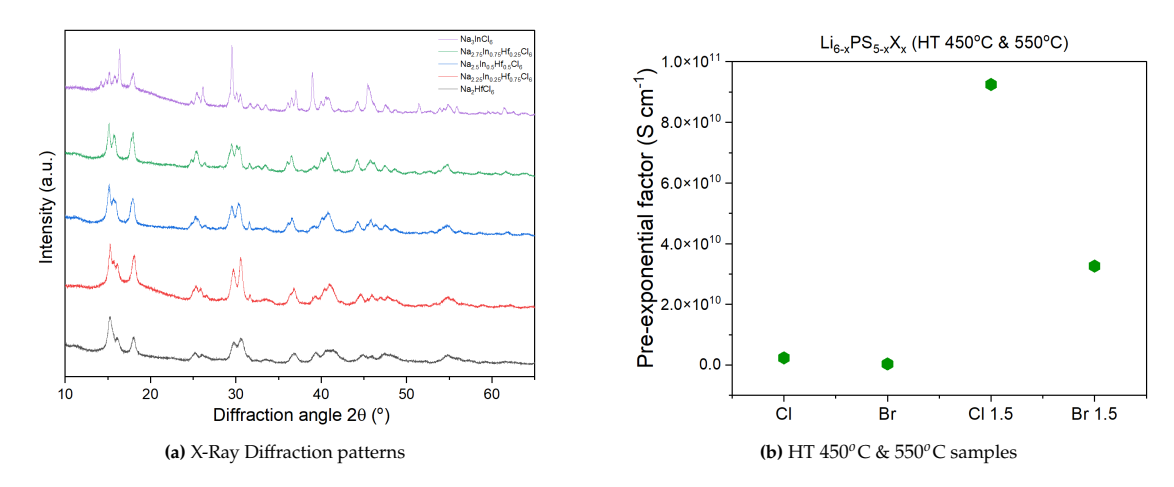
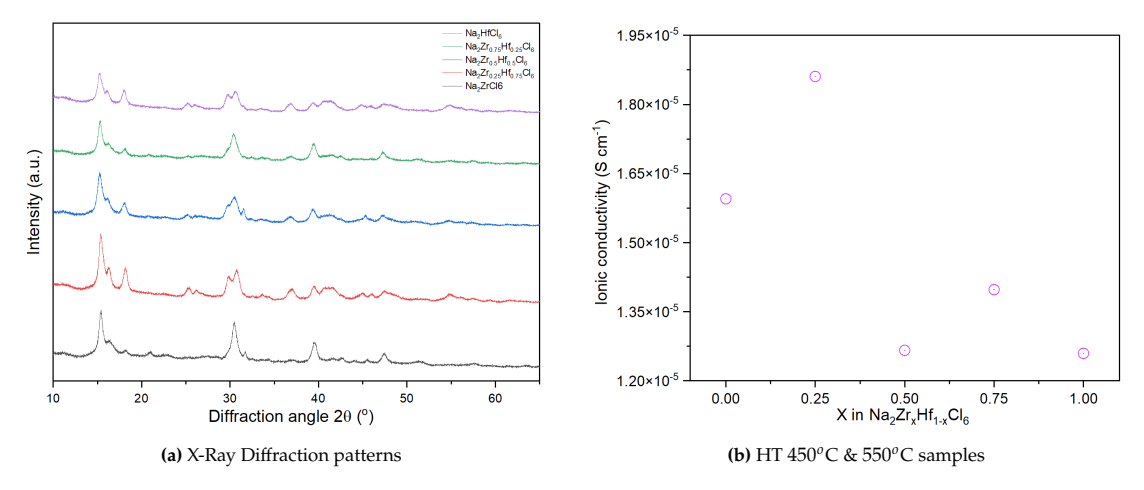


Figure B.1: X-Ray Diffraction patterns and ionic conductivity of  $Na_{2+x}In_xHf_{1-x}Cl_6$  (X = 0, 0.25, 0.5. 0.75, 1)

#### **B.1.2.** XRD patterns of $Na_2Zr_xHf_{1-x}Cl_6$

The below figure B.2 (a) and (b) shows the XRD patterns and ionic conductivity of the series of  $Na_2Zr_xHf_{1-x}Cl_6$  with (X = 0, 0.25, 0.5. 0.75, 1).



**Figure B.2:** X-Ray Diffraction patterns and ionic conductivity of  $Na_2Zr_xHf_{1-x}Cl_6$  (X = 0, 0.25, 0.5. 0.75, 1)

#### B.1.3. XRD pattern and ionic conductivity

The XRD patterns and ionic conductivity of the series of  $Na_xZr_{0.25}Hf_{0.75}Cl_{4+x}$  composition is shown in the below figure B.3 , respectively.

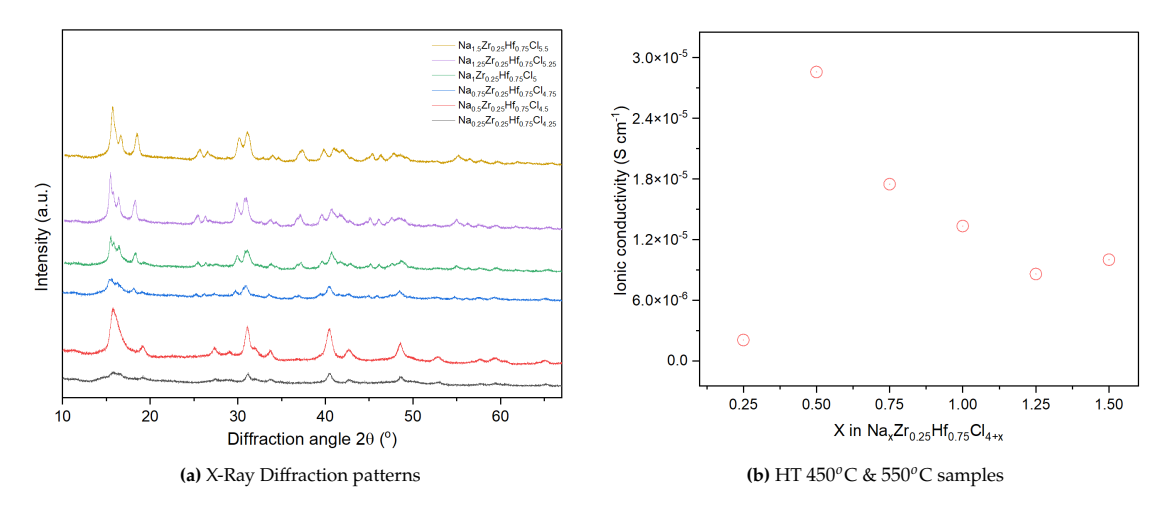


**Figure B.3:** X-Ray Diffraction patterns and ionic conductivity of  $Na_2Zr_xHf_{1-x}Cl_6$